TÉCNICO LISBOA

Numerical and Experimental Study of Wing Tip Endplates of a Formula Student Car

Tiago Pereira Rocha

Thesis to obtain the Master of Science Degree in

Aerospace Engineering

Supervisor: Prof. Luís Rego da Cunha Eça

Examination Committee

Chairperson: Prof. Fernando José Parracho Lau

Supervisor: Prof. Luís Rego da Cunha Eça

Member of the Committee: Prof. João Manuel Melo de Sousa

October 2020

Dedicated to my grandfather Fernando

Acknowledgments

This project would not have been possible without the help and support from a group of people.

First, I would like to express my gratitude towards my supervisor, professor Luís Eça, not only for the trust in proposing this project to me, but also for the guidance and feedback throughout.

My gratitude also goes to the Formula Student Técnico team, in particular to Inês Viveiros, Luís Morais and Jaime Pacheco, for the availability and assistance whenever needed.

I would also like to thank professor Luís Sousa for the time and effort put into printing (and re-printing) all the parts needed to make the wind tunnel model, without wich this work would certainly have been poorer.

To André Oliveira and professor André Marta: thank you for the cooperation with the wind tunnel experiments at the Aerospace Laboratory. From a random encounter, this proved to be a productive and rewarding partnership.

I also want to thank Pedro Costa, for the help setting up the DAQ of the balance at the Fluids Laboratory; and Sandra Ferreira Gomes, for proof-reading the dissertation and the support that dates back to our time together in the Formula Student team.

To my girlfriend, Carolina, thank you for being a constant source of enthusiasm, positivity and encouragement, even when mine waned.

Finally, a note to my family, my parents Fernando and Maria José, and my two sisters, Matilde and Sofia. For your love, support, and never-ending encouragement during this entire journey, especially when times were tough and things did not go according to plan, I am deeply thankful.

Resumo

Os apêndices aerodinâmicos dos carros Formula Student têm-se tornado cada vez mais complexos à medida que melhorias significativas se vão revelando cada vez mais difíceis de alcançar. Dado que as velocidades atingidas pelos carros em pista são relativamente baixas, e devido aos constrangimentos impostos pelas regras das competições, a sustentação que os carros produzem acarreta consigo elevados valores de resistência. Isto é particularmente relevante na classe elétrica, onde a autonomia da bateria é um dos maiores desafios.

Este trabalho apresenta um estudo sobre um conceito alternativo para as *endplates* da asa traseira de um Formula Student com o objetivo de reduzir a resistência global da mesma. Perfis alares são usados para a secção das *endplates*, modificando as características do escoamento em torno da asa: o ângulo de ataque induzido é reduzido, o que por sua vez resulta numa diminuição da resistência induzida sem perda de coeficiente de sustentação, aumentando a eficiência da asa.

Foi feita uma análise de convergência de malha para se avaliar o erro numérico envolvido nas simulações de CFD. Estas foram feitas primeiro para um modelo de asa simples, para analisar o efeito dos perfis das *endplates* no escoamento, bem como para identificar de que forma as dimensões das mesmas influenciam o desempenho da asa. Com base nos resultados, o conceito foi aplicado ao conjunto completo da asa.

Um modelo à escala 1:2.5 foi construído com recurso à impressão 3D, que foi testado no túnel de baixo números de Reynolds do Laboratório de Mecânica de Fluidos e no Túnel Aero-Acústico do Laboratório de Aeroespacial do Instituto Superior Técnico. A utilização das duas instalações experimentais permitiu avaliar a influência do número de Reynolds no desempenho da solução proposta. Os resultados obtidos confirmaram o potencial do conceito proposto.

Palavras-chave: Formula Student, asas finitas, *endplates*, CFD, túnel de vento, validação

Abstract

The aerodynamic appendages of Formula Student cars, crucial for their overall on-track performance, are getting more intricate as the gains are getting more and more marginal. Given the low speeds the cars achieve and the geometric restrictions imposed by the rules, the downforce generated on the cars will imply very high drag forces, which is especially critical for the electric class, where the energy output is limited by the accumulator.

It is this project's aim to propose a different design for the endplate of the rear wing of such a car. By making use of airfoils, effectively converting the endplate from a flat plate into a vertical wing, the characteristics of the rear wing assembly are changed – reducing the induced angle of attack, decreasing the drag coefficient without loss of lift coefficient, thereby increasing its efficiency.

First, a mesh convergence analysis was performed to assess the numerical accuracy of the simulations. Then, simulations were done with a single element wing in order to assess the hypothesis, as well as to understand how geometric factors contributed to the performance of the wing. The concept was afterwards applied to the full wing.

Finally, a 40%-scale model of the simulated wing was constructed with 3D printing to test it in the wind tunnel: first at the low Reynolds tunnel of the Fluids Laboratory; and at a later time at the CAST tunnel. The results were compared with the CFD simulations, confirming the potential of the concept theorized at the project's inception.

Keywords: Formula Student, finite wings, endplates, CFD, wind tunnel, validation

Contents

List of Tables

List of Figures

Nomenclature

Greek symbols

α	Angle of attack.
$\mathcal{AR}$	Wing aspect-ratio.
β	Angle of yaw/side-slip.
Γ	Circulation.
μ	Molecular viscosity coefficient.
ν	Kinematic viscosity.
Ω	Vorticity.
ω	Specific dissipation rate.
ρ	Density.
τ	Wall shear stress.

Roman symbols

b	Wingspan.
c	Chord.
L	Reference length.
p	Pressure.
S	Planform area.
y^+	Non-dimensional distance to the wall.
C_D	Drag coefficient.
C_f	Skin friction coefficient.
C_L	Lift coefficient.
C_p	Pressure coefficient.

Ma Mach number.

Re Reynolds Number.

u, v, w Velocity Cartesian components.

V Velocity magnitude.

Subscripts

∞ Free-stream condition.

i, j, k Computational indexes.

x, y, z Cartesian components.

Glossary

CAST	Centre for Aerospace Science and Technology
CFD	Computational Fluid Dynamics.
DAQ	Data Acquisition System.
DOF	Degree of freedom.
FSG	Formula Student Germany.
FS	Formula Student.
IST	Insituto Superior Técnico
RANS	Reynolds-averaged Navier Stokes.
SST	Shear stress transport.
TKE	Turbulent Kinetic Energy
WSS	Wall shear stress.
WT	Wind tunnel.

Chapter 1

Introduction

1.1 Overview of Vehicle Aerodynamics

Ever since the beginning of the automobile industry, the aerodynamics of vehicles has been an important aspect of their development. From an aerodynamics point of view, cars are blunt objects that move close to the ground. Their geometry is usually complex, which means that the airflow around them has a three-dimensional character, and that the boundary layers over the surfaces are usually fully turbulent due to strong pressure gradients. Separation of the airflow and wide wakes generated by it are frequently observed, two phenomena that are unsteady in nature. For passenger vehicles, this means that the drag coefficient, C_D (Equation 1.1), is of particular relevance. The amount of drag that a vehicle generates while in movement will greatly impact several aspects of its performance, for instance fuel consumption, stability, top speed and its acceleration [1].

For racecars, however, the drag coefficient is of secondary importance. In those, the generation of downforce – negative lift[1] – is of greatest importance, and therefore the lift coefficient, C_L (Equation 1.2), takes precedence in their design. The reason for this being that downforce increases the tyres' cornering ability (see section 1.2), which in turn leads to greater average speeds over a lap and consequently to a reduction of the laptime [2].

$$C_D = \frac{D}{\frac{1}{2}\rho A V^2} \tag{1.1}$$

$$C_L = \frac{L}{\frac{1}{2}\rho A V^2} \tag{1.2}$$

where C_D and C_L are, respectively, the lift and drag coefficients, ρ is the density of the fluid (in this case, air), V is the is the velocity of the (uniform) incoming flow, and A is the reference area.[2]

Historically, the development of race cars centered around the development of engines, tyres and

[1] Lift is by definition the force perpendicular to the incoming flow. It can be positive – in airplanes, where upward force is needed for sustained flight and simply called lift – or negative – also called downforce, since in automobiles what is desired is a downward force, pushing car against the ground for higher tyre grip

[2] The reference area depends on the main component of the drag force. As such, it can either be the frontal area (form drag) or the planform area (skin friction drag).

suspension systems. However, at the end of the 1960s, the first real aerodynamic developments in motorsport took place, when the Lotus Formula 1 team added a pair of wings to their cars (Figure 1.1). From that moment on, the aerodynamic downforce has been a hallmark of racecar performance (Figure 1.2).

Figure 1.1: Lotus 49B Formula 1 racecar. While it debuted in 1967, the wings were only introduced midway through 1968. Given a series of accidents due to inappropriate mounting structures and adjustable angles of attack, they were promptly banned [3].

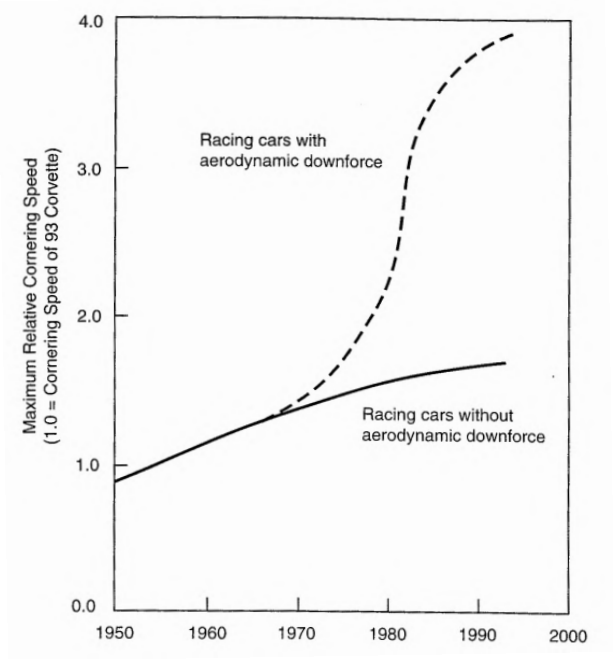

Figure 1.2: Maximum relative cornering speed over the years, with and without aerodynamic downforce [2].

To understand how the aerodynamic downforce positively affects the performance of racecars, one must look at what connects the cars to the road: the tyres.

1.2 Impact of Aerodynamic Loads on Tyre Behaviour and Racecar Performance

The forces needed to drive a car are created by the contact patch between tyre and road. For the tyre to generate these forces, it must deform, which will lead to slip – the difference between the velocity of the tyre and the velocity of the road. These forces depend on the vertical load that is being applied on the tyres, and will have a maximum for a given maximum adhesion coefficient μ (Equation 1.3). When this maximum adhesion coefficient is surpassed, the car will enter a slide.

$$\mu = \frac{F_\xi}{F_Z} \tag{1.3}$$

where F_ξ is a force component parallel to the ground and F_Z is the normal force component. If the ξ direction is coincident with the longitudinal axis of the vehicle, then $\xi = x$ and μ is called braking coefficient, when $\xi = y$, it is called cornering coefficient, as shown in Figure 1.3. It is worth noting that, in the braking case, wheel slip is defined as a percentual value, whereas in the lateral case slip is defined by a slip angle β. In both cases, the adhesion changes linearly with slip until a certain value of slip. As this value increases, the limit of grip of the tyre is achieved, and a slide will occur.

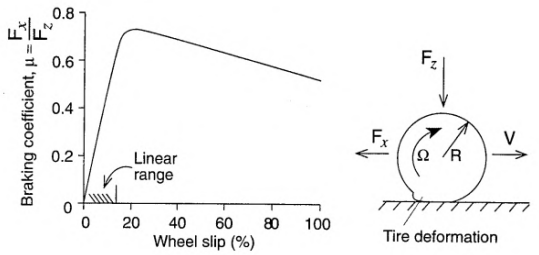

(a) Braking coefficient.

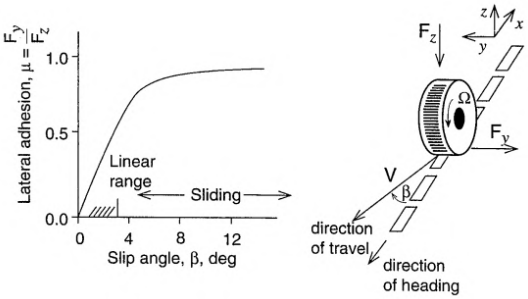

(b) Lateral coefficient.

Figure 1.3: Coefficients of adhesion as a function of slip for the braking and lateral situations [2].

The definition of the adhesion coefficient μ shows that, for a larger applied vertical load, the same horizontal force can be generated at a lower slip angle β. In practical terms, by increasing the normal load on the tyres, the lateral force that the tyres generate will increase too, meaning that the car will be able to turn at a higher speed without sliding.[3] One way to achieve higher loads is by increasing the car's mass. Since increasing the mass adds weight that will affect acceleration and the force needed to turn the car at the same rate, a new source of vertical load is necessary, which is where aerodynamic downforce comes in. Aerodynamic downforce increases the vertical load without adding weight to the car[4], thus enlarging the tyre's performance envelope (Figure 1.4).

A more specific analysis of the influence of downforce on laptimes is seen in Figure 1.5. In the figure, a much stronger dependence on the lift coefficient is observed, in comparison to the coefficient of drag,

[3]This also has other implications besides faster laptimes, namely regarding tyre management during a race, since less slip means less friction, and therefore less damage to the tyres.

[4]Technically not true, since the devices have mass themselves, but the vertical load generated is much greater than their weight, $F_{Z_{aerodynamicdevices}} \gg W_{aerodynamicdevices}$.

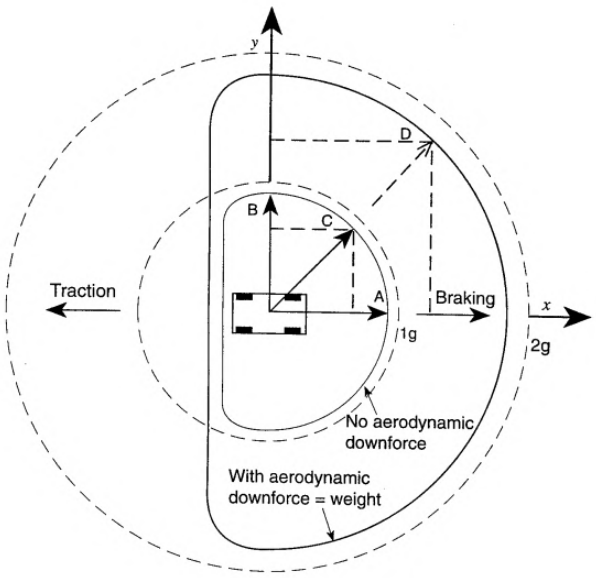

Figure 1.4: Schematic of the tyre's performance envelope. The downforce enlarges the range of operation of the tyre [2].

justifying the greater importance of C_L over C_D in racecars.

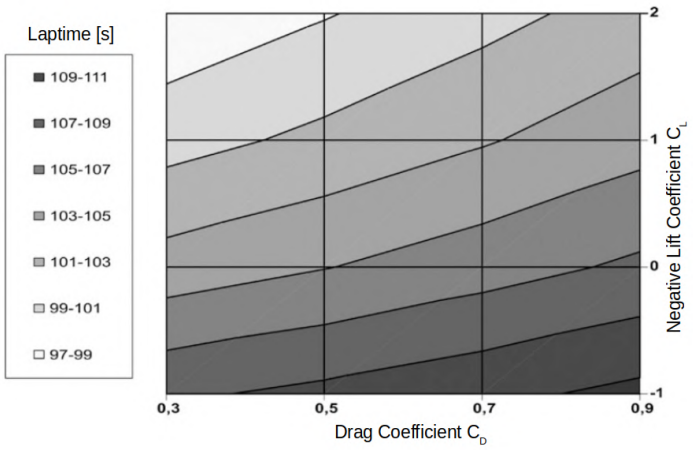

Figure 1.5: Relationship between laptimes and the coefficients of lift and drag of a generic racecar at the Hockenheimring [4].

1.3 Downforce Generation on a Racecar

Downforce can be created on a racecar in different manners:

1. By changing the car's shape in order to influence the airflow around it;
2. Via adding inverted wings to the car, in order to produce negative instead of positive lift;
3. Through other devices, like bargeboards and fins, that may or may not generate downforce themselves, but influence the other components in a way that makes them more effective.

In Figure 1.6, the contribution, in percentage, of each part to the C_D and C_L of a Formula 1 car is presented. The values are shown for the front wing, rear wing, undertray/floor, front wheels, rear wheels, barge boards and others. The values of C_D and C_L of each part are added in Table 1.1 [5].

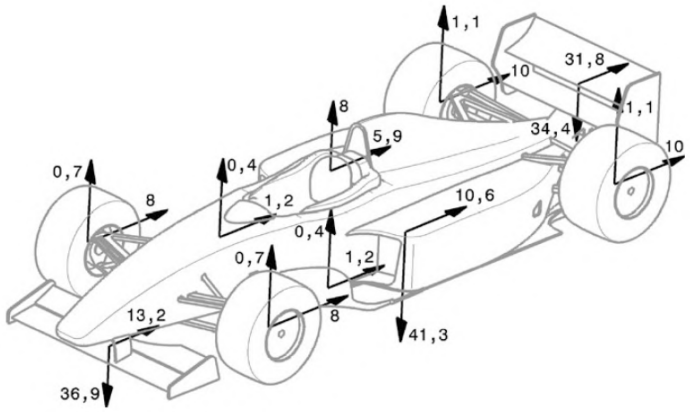

Figure 1.6: Contribution, in percentage, to the overall drag and downforce by each part of a Formula 1 car [5].

Component	Drag Coefficient		Lift Coefficient		C_L/C_D
	C_D	Proportion [%]	C_L	Proportion [%]	
Front Wing	0.123	13.2	0.9699	36.9	7.859
Rear Wing	0.297	31.8	0.899	34.4	3.029
Undertray	0.099	10.6	1.080	41.3	10.911
Front Wheels	0.150	16.0	-0.038	-1.4	-0.251
Rear Wheels	0.187	20.1	-0.061	-2.3	-0.326
Barge Boards	0.023	2.4	-0.020	-0.8	-0.889
Rest	0.055	5.9	-0.210	-8.0	-3.793
Total	0.934	100	2.617	100	2.802

Table 1.1: Values of C_D and C_L of different components of a Formula 1 car [5].

The front wing, rear wing and undertray are responsible for all the downforce of the car, fairly evenly. The difference between the 3 becomes noticeable when looking at the C_D values. The rear wing alone is responsible for 31.8% of all the resistance of the car, whereas the other two have a combined 23.8% of the drag. This may be attributed to the different interactions between the different parts of the racecar. In particular, the rear wing is usually the rearmost part of a racecar and stands in the wake of all those other parts.

1.4 Formula Student

1.4.1 Competition Summary

Formula Student is a worldwide competition for university students, in which they are challenged to conceive, design, fabricate, develop and compete with a small, formula type racecar (Figure 1.7).

Figure 1.7: Projecto FST Novabase's (now FST Lisboa), FST06e competing at Formula Student Hungary in 2015.

In a competition, the events are divided into two major categories: Static and Dynamic Events. Each of these two is further subdivided into different events:

- Static Events – concerned with the operational and/or engineering aspect of the project. They are divided into 3:
  - *Business Plan Presentation*: the team is challenged to think of its prototype as if it were intended for the market, with a focus on sales, profitability and marketability;
  - *Cost and Manufacturing*: design and manufacturing decisions are justified from a financial point of view;
  - *Engineering design*: engineering principles and decisions are presented and discussed with a series of judges, typically industry experts.
- Dynamic Events – events in which the cars' on-track performance is assessed. There are 5:
  - *Acceleration*: a 75-meter straight-line sprint from a stand still position in which longitudinal acceleration is paramount;
  - *Skidpad*: the cars are driven in a figure-of-eight track that tests the cars' lateral acceleration;
  - *Autocross*: a qualifying-lap like event in which peak performance is evaluated;
  - *Endurance*: a 22-kilometer event whose purpose is to assess the cars' reliability;
  - *Efficiency*: the fuel/energy necessary to complete the endurance event is measured to evaluate the compromise between all-out performance and fuel/energy economy.

For each event the teams are awarded points, according to a specific structure (Table 1.2). The static events account for 325 points, while the dynamic events value a maximum 675 points. This means that the performance of the cars is the main priority of the teams. As a result of the competition being evaluated on a basis of points and not on laptimes alone, the design process of the cars is done to achieve the maximum global number of points possible per competition, which will lead to certain design compromises.

Static Events	Points
Business Plan Presentation	75
Cost and Manufacturing	100
Engineering Design	150
Dynamic Events	
Skid Pad	75
Acceleration	75
Autocross	100
Endurance	325
Efficiency	100
Total	1000

Table 1.2: Maximum points awarded at a Formula Student Competition.

1.4.2 Aerodynamics in Formula Student

As seen in section 1.2, the normal load applied on a tyre increases its grip. In order to better evaluate the effect of downforce on the cornering velocity, its impact on the maximum theoretical cornering velocity before the tyre slips can be deducted. Considering a constant friction coefficient and that, in the mentioned state, the friction force is equal to the centripetal force, it leads to Equation 1.4.

$$\mu F_Z = \mu \left(mg + \frac{1}{2}\rho C_L A V^2 \right) = \frac{mV^2}{r} \Rightarrow V = \sqrt{\frac{mg}{\frac{m}{\mu r} - \frac{1}{2}\rho C_L A}} \tag{1.4}$$

where m is the car's mass, g is the gravitational acceleration and r is the corner radius[5]. This equation is plotted against different values of r for a constant $C_L = 1.7$ in Figure 1.8 [6].

Even though the Autocross and Endurance tracks are made in a way to prevent excessive speeds, featuring small radii corners, slaloms, short straights and hairpins, the speeds that are reached are high enough to provide significant aerodynamic forces, enhancing the prototypes' performance [7].

In FS, however, the wings are only allowed in design boxes imposed by the rules, effectively constraining the size of the wings (Figure 1.9). Consequently, in order to generate significant C_L values, the wings will inevitably have very short wingspans for their total chords, yielding very low $\mathcal{AR}$ values and resulting in a large C_D penalty.

[5]The corner raidus r is assumed to be constant

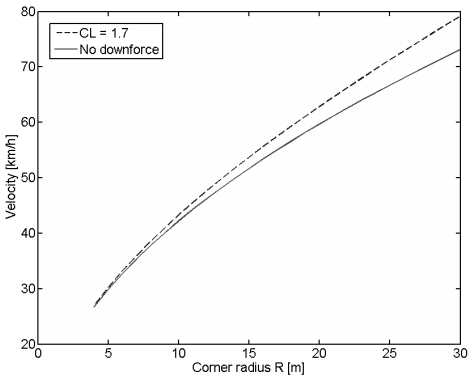

(a) Maximum velocity as a function of corner radius.

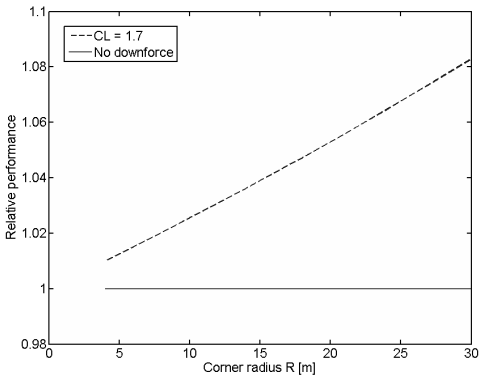

(b) Relative car performance.

Figure 1.8: Maximum velocity and relative performance for a car without downforce and one with a C_L of 1.7 [6].

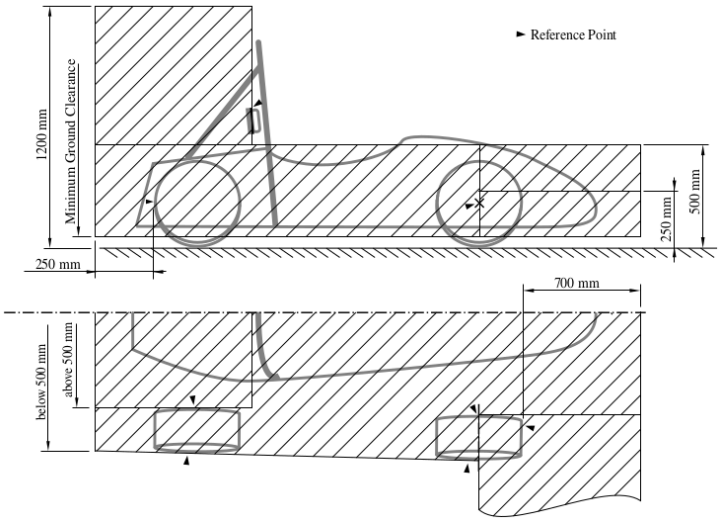

Figure 1.9: Design limitations on aerodynamic devices imposed by FS rules [8].

Nowadays, an aerodynamic kit is a must-have for top performance in Formula Student competitions, typically comprising front and rear multi-element wings, undertrays and diffusers, and multiple side mounted wings on sidepods (Figure 1.10).

1.5 Motivation

In a two-dimensional, inviscid flow over an airfoil, the lift it produces is tied to the circulation around it. Circulation is defined as the line integral of the velocity field along a closed curve. The lift – per unit of span – will then be, according to the Kutta-Joukowski theorem: $L' = \rho_\infty V_\infty \Gamma$. For any particular airfoil at a given angle of attack only one value of Γ is possible, which leads to the flow leaving the airfoil smoothly at its trailing edge in what is known as the Kutta condition.

$$\Gamma \equiv \oint_C \boldsymbol{V} \cdot \boldsymbol{ds} \tag{1.5}$$

Figure 1.10: Ecurie Aix, from the RWTH Aachen, participating at FSG 2019 with its eace08 car. See the complex aerodynamic package. ©FSG – Elena Schulz.

where $\boldsymbol{V}$ is the velocity field and C is an arbitrary curve.

The circulation is generated when an airfoil is started from rest. At this point, significant velocity gradients at the trailing edge form a region of strong vorticity that moves downstream, the starting vortex, that has a counterclockwise circulation. The starting vortex is convected with the increase of the Reynolds number and it leaves an opposite circulation around the airfoil satisfying the Kutta condition.

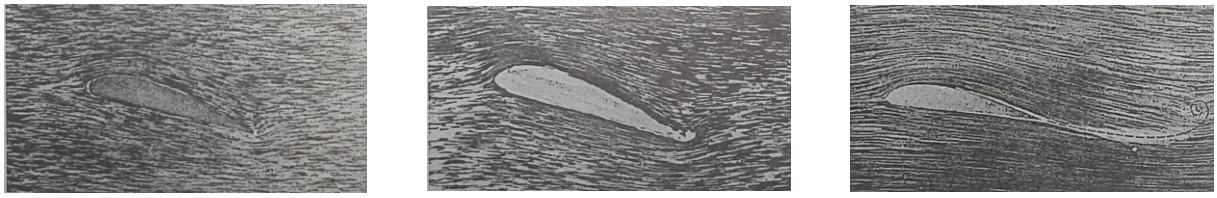

(a) Airflow immediately after start. (b) Vorticity buildup. (c) Starting vortex shedding.

Figure 1.11: Circulation generation on an airfoil [9].

In finite wings, the vortex system generated is much more complex. Since the pressure differential cannot be sustained on the wing tips where the wing ends, two trailing vortexes are shed from the high-pressure to the low-pressure surface. This originates a spanwise airflow on both surfaces, going from the root to the wingtip on the pressure side and in the opposite direction on the suction side. Moreover, these vortices have another effect on the airflow over the wing: a downward velocity component in the near vicinity of the wing, v_i, called downwash. Subsequently the wing will have an effective angle of attack $\alpha_{eff} = \alpha - \alpha_i$, where α is the geometric angle of attack and α_i is the induced angle of attack. The induced angle of attack gives rise to another drag component, the induced drag D_i, and to a reduction in the lift produced by the wing [9, 10].

The characteristics of a finite wing can be derived from Prandtl's lifting line theory. It replaces the wing by a bound vortex along the spanwise direction with a force $L' = \rho_\infty V_\infty \Gamma$ and two free vortices trailing downstream from the wing tips to infinity (due to the Helmholtz's theorem, which states that a vortex filament cannot end in a fluid).

Despite its approximations, the lifting line theory yields useful relations that help understand the difference between a three dimensional wing and an airfoil. One important parameter of finite wings is

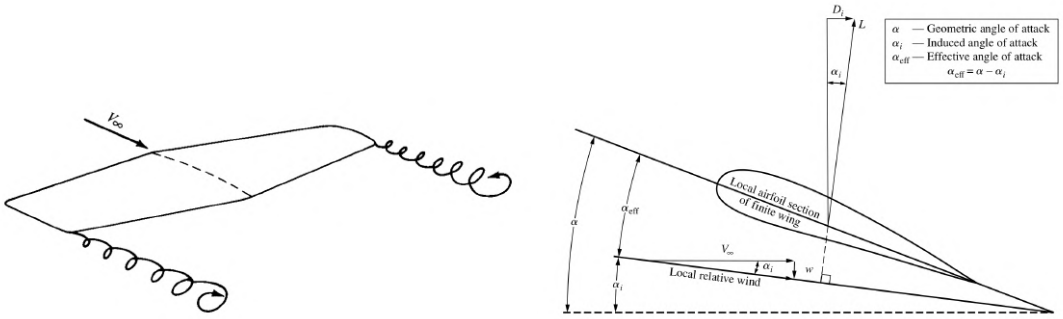

(a) Wing-tip vortices. (b) Induced angle of attack, α_i.

Figure 1.12: Three-dimensional flow over a finite wing [10].

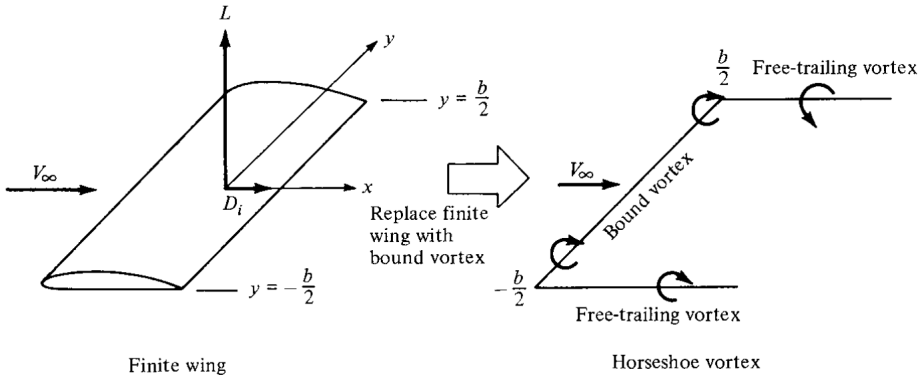

Figure 1.13: Prandtl's lifting line theory. The wing is replaced by a bound vortex and two trailing vortices [10].

the aspect ratio, $\mathcal{AR} = b/\bar{c} = b^2/S$, where b is the wingspan, $\bar{c}$ is the average chord and S the planform area. For a 3D wing with a given airfoil, its C_L can be related to that of its airfoil by Equation 1.6.

$$C_{L_{3D}} = a_{3D}(\alpha + \beta) \quad \text{with} \quad a_{3D} = \frac{a_{2D}}{1 + \frac{a_{2D}}{\pi \mathcal{AR}}} \tag{1.6}$$

where α is the angle of attack, β is the zero lift angle and $a_{2D} = \left(\frac{dC_L}{d\alpha}\right)_{2D} \approx 2\pi$. This equation implies that, for an airfoil, because $\mathcal{AR} = \infty$, then $a_{3D} = a_{2D}$. As $\mathcal{AR}$ decreases, so will the value of a_{3D} and consequently the $C_{L_{3D}}$. This trend is shown in Figure 1.14.

The induced drag can also be expressed as a function of the $\mathcal{AR}$ (Equation 1.7).

$$C_{D_i} = \frac{C_L^2}{\pi e \mathcal{AR}} \quad \text{with} \quad e = 1/(1 + \delta) \tag{1.7}$$

where e is the Oswald efficiency factor. This indicates a similar relation to $C_{L_{3D}}$, since that for $\mathcal{AR} = \infty$, $C_{D_i} = 0$, and it increases with decreasing $\mathcal{AR}$.

In the aeronautic industry, one of the ways to make commercial flights more cost-effective is by reducing the airplanes' fuel consumption through reduction of their aerodynamic resistance, seeing that the induced drag of an aircraft can account for 30-40% of its total drag in long-range cruise condition [12]. The tips of the wings are considered *dead zones* in terms of aerodynamic efficiency, since they produce much more drag than lift because of the reduced pressure differential between the upper and

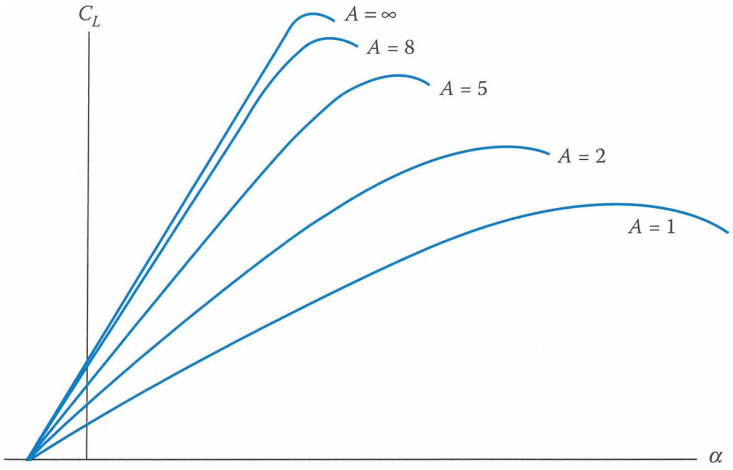

Figure 1.14: C_L as a function of α for different $\mathcal{AR}$ values [11].

lower surfaces at the tip of the wing. With this in mind, several wingtip designs (Figure 1.15) have been developed over the years, which aim to reduce the drag generated by airplanes, thus improving its performance specifications, with some achieving reductions of about 20% of the wing induced drag and increasing the lift-over-drag ratio of the wing of circa 9% near the design lift coefficient [13].

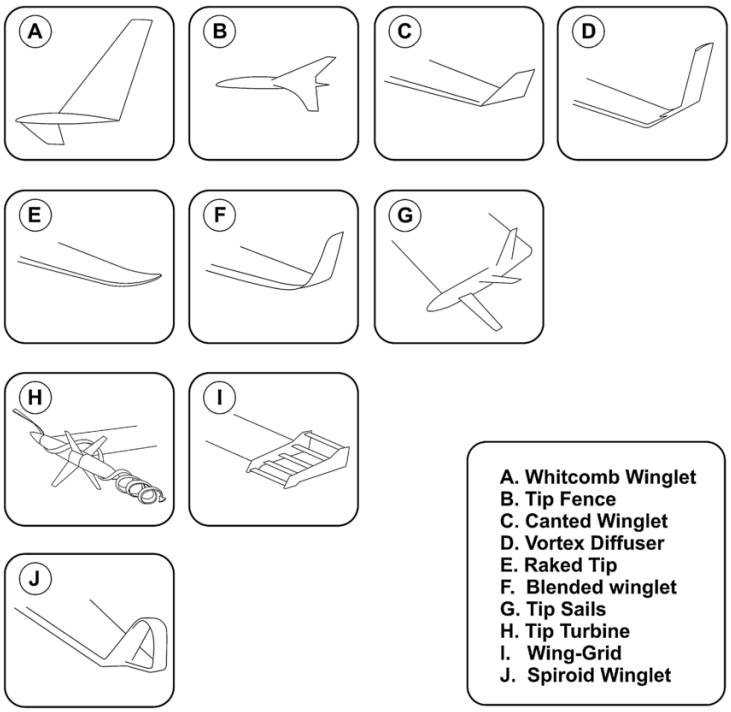

Figure 1.15: Different wingtip designs [14].

Yet, one fact that is often overlooked is that, to be fully effective, the vertical surface at the tip must produce significant side forces, for which purpose a flat plate is ineffective since it is not a lifting device. The side forces are necessary so that the lift-induced inflow above the wing tip can be reduced or, conversely, the outflow below the tip.

The same principle can be applied to racecar wings, or in this specific case for formula student racecars. As was mentioned above, the wings used in Formula Student have low aspect-ratios due to

regulatory constraints. As such, in order to generate downforce at the speeds registered in the events, a large drag penalty will inevitably be incurred. Table 1.3 presents the values of C_L and C_D of FST Lisboa's latest prototype, the FST09e, obtained in a 3D CFD simulation [15]. These values highlight the problem of the low aspect-ratio wings in FS cars, which is especially noticeable for the rear wing. In spite of producing 34.5% of the total downforce of the car (2nd best of the lifting devices, behind the front wing with 39.8% and ahead of the undertray with 23.8%), it accounts for 38.1% of its total drag, outweighing the drag contributions of the other lifting devices combined, front wing and undertray (13.7+10.9=24.6%), for a lowest C_L/C_D ratio out of the 3 parts at 2.072.

Component	Drag Coefficient		Lift Coefficient		C_L/C_D
	C_D	Proportion [%]	C_L	Proportion [%]	
Front Wing	-0,175	13,7	-1,165	39,8	6,669
Rear Wing	-0,487	38,1	-1,010	34,5	2,072
Undertray	-0,140	10,9	-0,697	23,8	4,994
Front Wheels	-0,066	5,1	0,051	-1,7	-0,780
Rear Wheels	-0,074	5,8	0,037	-1,2	-0,495
Sidepod	0,013	-1,0	0,105	-3,6	8,154
Rest	-0,350	27,4	-0,247	8,4	0,706
Total	-1,278	100	-2,926	100	2,289

Table 1.3: C_D and C_L distribution over different parts on a FS car [15].

The drag produced by the wings has other implications besides the low aerodynamic efficiency itself. The power needed to overcome the aerodynamic drag is given by Equation 1.8 [16], where a direct dependence on the C_D value is observed. In an electric FS car, the battery is designed to complete the Endurance event at a specific performance threshold [17]. This means, accordingly, that it will have a fixed weight during all the dynamic events, even those where the energy required is less than that of the endurance, penalizing the performance in the other events.

$$P_{drag} = DV \Leftrightarrow P_{drag} = C_D \frac{1}{2} \rho A V^3 \tag{1.8}$$

where P_{drag} is the power required to overcome the drag force.

One way to reduce the drag of the rear wing is by using active elements on it [18]. Nonetheless, there are drawbacks to the cited design, namely the complexity of the assembly, which may lead to reliabilitity problems, and the added weight, as well as the polar moment of inertia of the entire wing. Therefore, the need arises to find a simpler, much more efficient wing design: one that has a higher C_L/C_D, possessing the desirable design C_L for cornering performance, while simultaneously having a low C_D so as to not compromise the top speed.

1.6 Objectives

In Formula Student, it is common for the rear wings to feature gurney flaps on their endplates (Figure 1.16) to boost the wing's downforce. It is equivalent to adding curvature to the endplate, changing the velocity distribution of the wing and increasing the amount of downforce it generates. However, since it is a flat plat perpendicular to the airflow, it generates flow separation and thus the increase in downforce is done at the expense of a drag penalty.

Figure 1.16: Gurney flap on an endplate of a FS car.

The objective of this project is then to find an alternative solution to the conventional endplate design of a FS car's rear wing that creates the same effect of the gurney flap, but without the added drag. This will be done by using an endplate with curvature, namely an airfoil, turning the endplates into lifting surfaces, whose vortices are exploited with the aim of reducing the wing's downwash v_i and induced angle of attack α_i, thereby increasing the wing's load and therefore downforce; reducing its overall drag by reduction of the induced drag D_i and as a result increasing the wing's and the car's aerodynamic efficiency.

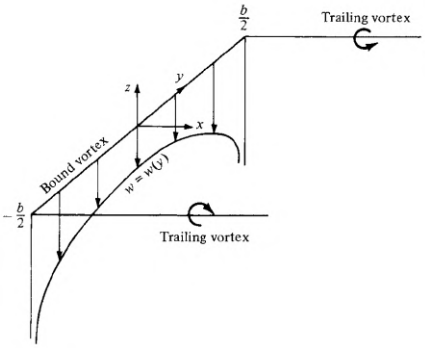

Figure 1.17: Downwash distribution according to the lifting line theory [10].

The concept was first investigated with CFD simulations in Star-CCM+, whereby different airfoils and endplate dimensions were tested. Afterwards experimental tests were done to confirm the trends seen in the simulations. The wind tunnel experiments also allowed the assessment of the Reynolds number

effect on the efficiency of the proposed design.

1.7 Thesis Outline

This thesis is divided into six chapters.

Chapter 1 is an introduction to the project. An overview of vehicle aerodynamics is given, with emphasis on the impact of aerodynamics in motorsport. A brief description of the Formula Student competition is provided, as well as some context into the topic of the thesis.

The Chapter 2 is devoted to the mathematical formulation of the problem, namely the equations used to perform the CFD simulations.

Chapter 3 is concerned with the topic of numerical error. A theoretical background is provided and the steps taken to assess the error are described. The setup used in the simulations in Star-CCM+ is also presented.

Chapter 4 is dedicated to the numerical simulations done in this project. The geometries tested, as well as their respective findings, are presented and discussed.

In Chapter 5 the experimental tests are described, including the wind tunnels used, model construction, test methodology and the results obtained. Furthermore, a comparison with the CFD simulations is established to validate the simulations' results.

Finally, Chapter 6 presents the conclusions of the entire project. Suggestions for future work are also laid out.

Chapter 2

Mathematical Formulation of the Problem

In this chapter the mathematical formulation of the problem is described. The equations used to perform the CFD simulations of interest are introduced, namely the RANS equations, the SST K-omega Turbulence Model and the GammaReTheta Transition Model. Some theoretical background is also provided to justify their use.

2.1 Airflow Characterisation

The choice of the mathematical equations depends on the considered Reynolds number. The Reynolds number (Equation 2.1) is a non-dimensional parameter that represents the ratio between inertial and diffusion forces of the fluid [9].

$$Re = \frac{\rho V L}{\mu} = \frac{V L}{\nu} \tag{2.1}$$

where V is the free-stream velocity (m/s), L is the reference length of the flow (m), μ is the dynamic viscosity ($kg/(m \cdot K)$), and ν is the kinematic viscosity, defined by $\nu = \mu/\rho$ ($m^{-2}K^{-1}$).

The Re of this case is calculated considering $V = 15m/s$, corresponding to the average velocity over a lap at a FS track, L is the total chord of the rear wing of FST09e, $L = 0.4 + 0.2 + 0.2 = 0.8m$, and ρ and μ are the density and dynamic viscosity of the air, respectively $1.225kg/m^3$ and $1.81 \times 10^{-5}kg/(m \cdot s)$ at $15^\circ C$. These values yield a $Re \approx 8 \times 10^5$.

The transition from laminar to turbulent flow over an airfoil depends on the pressure gradient it experiences, that is, its angle of attack, and also on the Reynolds number of the flow. For a NACA0012 airfoil at $\alpha = 0^\circ$ transition was observed for $Re = 1 \times 10^5$ [19]. Therefore, transition may be present on the wing and play a role on the development of the boundary-layers on the wings' surfaces.

2.2 RANS Equations

To analyze an incompressible, viscous flow with constant properties, two equations are needed: the continuity and the momentum equations (Equations (2.3) and (2.4), respectively [9]).

$$\rho \frac{\partial U_i}{\partial x_i} = 0 \tag{2.2}$$

$$\frac{DU_i}{Dt} \equiv \frac{\partial U_i}{\partial t} + U_j \frac{\partial U_i}{\partial x_j} = -\frac{1}{\rho}\frac{\partial p}{\partial x_i} + \nu \frac{\partial^2 U_i}{\partial x_j^2} + f_i \tag{2.3}$$

where ν is the kinematic viscosity, and f_i is the mass force in the component i per mass unit.

These equations describe an unsteady flow due to the time dependance observed of their variables. On the other hand, by decomposing the time-dependent variables of the momentum equations into a time averaged and fluctuation components ($u = \bar{u} + u'$, [20]), the RANS equations are reached (Equation 2.5) for the statistically steady flow of an incompressible fluid.

$$\rho \frac{\partial \bar{u}_i}{\partial x_i} = 0 \tag{2.4}$$

$$\rho \bar{u}_j \frac{\partial \bar{u}_i}{\partial x_j} = \rho \bar{f}_i + \frac{\partial}{\partial x_j}\left[-\bar{p}\delta_{ij} + \mu\left(\frac{\partial \bar{u}_i}{\partial x_j} + \frac{\partial \bar{u}_j}{\partial x_i}\right) - \rho\overline{u_i' u_j'}\right] \tag{2.5}$$

where the left-hand side is the change in mean momentum in the fluid element, that is counteracted on the right hand side by, respectively, the mean body force, the isotropic stress thanks to the mean pressure field, the viscous stresses, and apparent stress $(-\rho\overline{u_i' u_j'})$) due to the fluctuating velocity field, usually referred to as the Reynolds stress.

2.3 Turbulence Models

The aforementioned Reynolds stress term requires additional modeling to close the system of equations. For this purpose many turbulence models have been created. In the field of external aerodynamics three models have been widely used:

- Spalart-Allmaras;
- K-epsilon models;
- K-omega models.

The Spalart-Allmaras model is a one equation model. It gives good results for applications where the boundary-layer is generally attached and massive separations areas do not exist, for example: the flow over a wing, fuselage or other aerospace external-flow applications.

The K-epsilon (k-ε) and K-omega (k-ω) family models are both two equation models, i.e., both models incorporate two additional transport equations to account for the turbulent properties of the flow.

The original *k*-ε model [21] was constructed for high Reynolds numbers, and therefore relied on the use of wall functions to correctly predict the airflow behaviour in the boundary-layer. Over time modifications have been made to the *k*-ε model in order to better assess the effects of viscosity near the wall. Despite these improvements, the *k*-ε model has its deficiencies. In aerodynamic calculations, like those of whole-aircraft and automobile simulations, the complex geometries will origin flow events of varying length scales (vortices, wakes and others). Though the majority of the flow field is inviscid, its structure will inevitably be influenced by what happens in the boundary-layer where the viscous forces are significant. The *k*-ε model also predicts too much turbulent shear stress, especially in adverse pressure gradients, often resulting in suppression of separation on curved walls.

In contrast to the *k*-ε model, the *k*-ω behaves better for boundary-layers under adverse pressure gradients. It does not require wall distance computation and can also be applied throughout the entire boundary-layer, including the viscous sub-layer, without the need for modifications. The main disadvantge of the *k*-ω model is that the boundary-layer calculations are sensitive to the free-stream values of turbulence properties, which is mainly problematic for internal flow applications, where care is needed when choosing the boundary conditions.

Due to the reasons above, as well as the flow characterisation of section 2.1 and considerations exposed in Chapter 1, one of the *k*-ω models was used throughout the project, namely the SST *k*-ω model.

2.3.1 SST K-omega Model

The *k*-ω turbulence model was first proposed by Wilcox [22]. It uses two transport equations for the variables k – the turbulent kinetic energy – and ω – the specific dissipation rate (Equations (2.6) and (2.7)).

$$\frac{\partial(\rho u_j k)}{\partial x_j} = \rho P - \beta^* \rho \omega k + \frac{\partial}{\partial x_j}\left[\left(\mu + \sigma_k \frac{\rho k}{\omega}\right)\frac{\partial k}{\partial x_j}\right] \tag{2.6}$$

$$\frac{\partial(\rho u_j \omega)}{\partial x_j} = \frac{\alpha\omega}{k} P - \beta \rho \omega^2 + \frac{\partial}{\partial x_j}\left[\left(\mu + \sigma_\omega \frac{\rho k}{\omega}\right)\frac{\partial \omega}{\partial x_j}\right] + \frac{\rho \sigma_d}{\omega}\frac{\partial k}{\partial x_j}\frac{\partial \omega}{\partial x_j}. \tag{2.7}$$

where $P = \tau_{ij}\frac{\partial u_i}{\partial x_j}$; and the fraction $\rho k/\omega$ represents the eddy viscosity, μ_T. The closure coefficients are:

$$\alpha = 5/9, \quad \beta = 3/40, \quad \beta* = 9/100, \quad \sigma_k = 1/2, \quad \sigma_w = 1/2 \tag{2.8}$$

Due to the *k*-ω model's sensitivity to the free-stream values of the turbulence properties, there have been attempts to improve the original model and address this problem, namely the SST *k*-ω [23].

The SST *k*-ω model's purpose is to retain the robustness of the original *k*-ω model near the wall while harnessing the free-stream independence of the *k*-ε model. This is achieved in the following way:

1. Transform the original *k*-ε model into a *k*-ω style formulation;

2. The *k*-ω model is multiplied by a function F_1, while the transformed *k*-ε model is multiplied by $(1 - F_1)$;

3. The two equations are added together to form the new Baseline *k*-ω model.

$$\frac{\partial(\rho k)}{\partial t} + \frac{\partial(\rho u_j k)}{\partial x_j} = P - \beta^* \rho \omega k + \frac{\partial}{\partial x_j}\left[(\mu + \sigma_k \mu_t)\frac{\partial k}{\partial x_j}\right] \tag{2.9}$$

$$\frac{\partial(\rho \omega)}{\partial t} + \frac{\partial(\rho u_j \omega)}{\partial x_j} = \frac{\gamma}{\nu_t} P - \beta \rho \omega^2 + \frac{\partial}{\partial x_j}\left[(\mu + \sigma_\omega \mu_t)\frac{\partial \omega}{\partial x_j}\right] + 2(1 - F_1)\frac{\rho \sigma_{\omega 2}}{\omega}\frac{\partial k}{\partial x_j}\frac{\partial \omega}{\partial x_j} \tag{2.10}$$

The function F_1 is built in a way as to be equal to 1 in the inner region of the boundary layer and to gradually transition to 0 in the outer region of the boundary-layer. This blending function F_1 accomplishes the stated goal by effectively activating the original *k*-ω model in the boundary-layer and switching to the *k*-ε model in the free-stream, thus eliminating the original *k*-ω model's main issue.

The final SST *k*-ω model formulation is achieved by introducing a modification to the eddy viscosity. There is now a limiter in place for the eddy viscosity to improve the model's performance in flows with adverse pressure gradients and wake regions:

$$\mu_t = \frac{\rho a_1 k}{\max(a_1 \omega, \Omega F_2)} \tag{2.11}$$

where Ω is the absolute value of the vorticity and F_2 is a blending function [23].

The new coefficients C are calculated from two sets of constants, C_1 and C_2, by use of the F_1 function, $C = F_1 C_1 + (1 - F_1)C_2$. The set of constants C_1 pertains to the SST *k*-ω model (Equation 2.12), while the C_2 constants are taken from the standard *k*-ε model (Equation 2.13).

$$\begin{gathered} \sigma_{k1} = 0.85, \quad \sigma_{w1} = 0.5, \quad \beta_1 = 0.0750, \quad a_1 = 0.31 \\ \beta^* = 0.09, \quad k = 0.41, \quad \gamma_1 = \beta_1/\beta^* - \sigma_{w1} k^2/\sqrt{\beta^*} \end{gathered} \tag{2.12}$$

$$\begin{gathered} \sigma_{k2} = 1.0, \quad \sigma_{w2} = 0.856, \quad \beta_2 = 0.0828 \\ \beta^* = 0.09, \quad k = 0.41, \quad \gamma_2 = \beta_2/\beta^* - \sigma_{w2} k^2/\sqrt{\beta^*} \end{gathered} \tag{2.13}$$

2.3.2 Boundary-layer

The flow over a wing constitutes a wall bounded flow in which areas of laminar, transition and turbulent flow are likely to exist, depending on its geometry and Reynolds number. In this project, given the calculated Re in section 2.1, all these phenomena are expected. Accordingly, it is necessary to correctly calculate the shear stress at the wall so that the viscous effects are properly captured. To achieve this, the flow and turbulence parameters across the boundary-layer have to be accurately predicted.

The boundary-layer is the region of the flow in which the viscosity effects must be taken into account [24]. Due to the viscosity of real fluids, the relative velocity of the fluid to the wall is zero, $V_{fluid} = V_{wall}$, which constitutes the no-slip condition. The boundary-layer is thinner for higher Reynolds numbers due

to the reduced effects of the viscosity, and thicker for lower Reynolds numbers, where the diffusion forces are larger than the inertial forces.

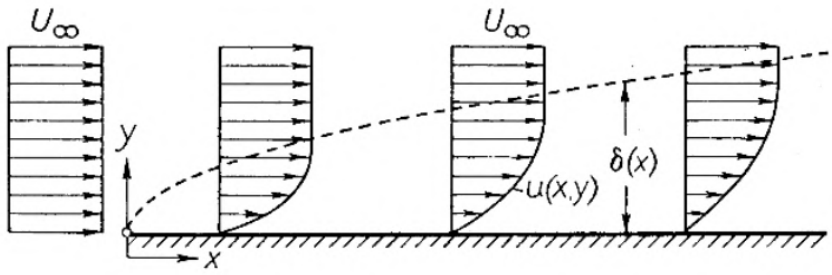

Figure 2.1: Schematic of a boundary-layer on a flat plate with no angle of attack [24].

The boundary-layer itself is initially laminar and remains so until a certain critical Reynolds number, Re_{crit}, which onsets the transition from laminar to turbulent (Figure 2.2a). In these two regimes, the boundary-layer will have different velocity profiles. More specifically, the turbulent boundary-layer is thicker than the laminar boundary-layer due to the diffusion introduced by the turbulence (Figure 2.2b).

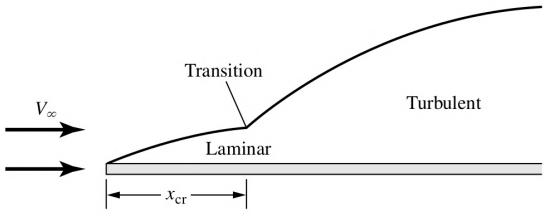

(a) Boundary-layer transition from x_{crit}, corresponding to the Re_{crit}.

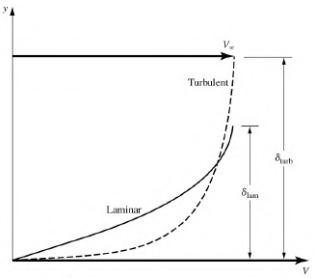

(b) Overlapped laminar and turbulent boundary-layer profiles.

Figure 2.2: Illustration of the transition from laminar to turbulent boundary-layer with the respective velocity profiles [10].

In turbulent boundary-layers, where the turbulence gives rise to the closure problem described in section 2.2, the turbulence models are used to solve the flow equations. To achieve this, the boundary-layer is divided into two regions [25]: an inner region, which comprehends 10 to 20% of the total thickness of the boundary-layer; and an outer region, in which direct viscous effects are negligible. The inner region is further subdivided into different three layers [26], as illustrated in Figure 2.3:

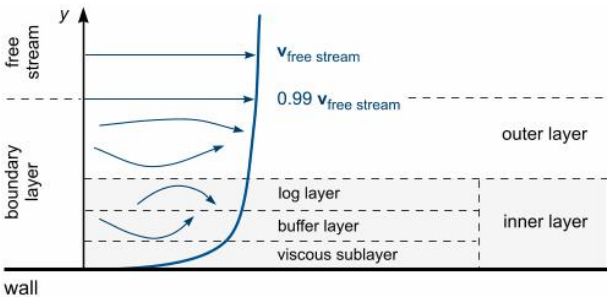

Figure 2.3: Subdivision of the turbulent boundary-layer [26].

- *Viscous Sublayer*: fluid layer in contact with the wall;
- *Buffer Layer*: transitional layer between the viscous sublayer and the log layer;
- *Log Layer*: layer farthest from the wall.

Where these different layers are located in relation to the wall is based on a non-dimensional distance to the wall, y^+ (Equation 2.14).

$$y^+ = \frac{y\rho u_\tau}{\mu} \tag{2.14}$$

where y is the distance to the wall and u_τ is the friction velocity at the nearest wall. It can be expressed as $u_\tau \equiv \sqrt{\frac{\tau_w}{\rho}}$, where τ_w is the shear-stress on the wall.

Viscous Sub-layer This viscous sub-layer is very thin ($y^+ < 5$) and the viscous effects are dominant in this region adjacent to the wall, where the flow is almost laminar. It can be assumed that the shear stress is approximately constant and equal to the wall shear stress τ_w throughout the layer. This assumption will eventually lead to the conclusion that there is a linear relationship between the velocity and distance to the wall, $u^+ = y^+$, where u^+ is the dimensionless velocity, $u^+ = U_\infty/u_\tau$. For this reason the viscous sub-layer is sometimes also referred to as the linear sub-layer.

Buffer layer The buffer layer is the region immediately after the viscous sub-layer and acts as a transition zone to the log-law layer, as the viscous and turbulent stresses have roughly the same magnitude. It is, then, situated in the region where $5 < y^+ < 30$ and it can be verified that the maximum turbulent production occurs at around $y^+ = 12$ (variations may be observed depending on the Reynolds number) [27]. Since it is difficult to accurately modelate the flow characteristics in this layer, the smallest cell in a CFD mesh is either put inside the viscous sub-layer, where low Reynolds numbers models are applied, or in the outer sub-layer, in which case high Reynolds numbers models are used (viscous versus turbulent approach, respectively).

Log-law Layer The log-law layer is situated in the region where $30 < y^+ < Y$ (the upper limit is dependent on the Reynolds number) and is where both turbulent and viscous effects are of significance. In this region the following relationship applies:

$$u^+ = \frac{1}{\kappa} ln(y^+) + B = \frac{1}{\kappa} ln(Ey^+) \tag{2.15}$$

where the κ is the von Karman constant and B is the additive constant. Both these constants are universally valid for all turbulent flows over smooth walls and may take the values $\kappa = 0.41$ and $B = 5.0$. The name of this layer comes from the logarithm present in Equation 2.15.

The velocity profile in the three layers is displayed graphically in Figure 2.4.

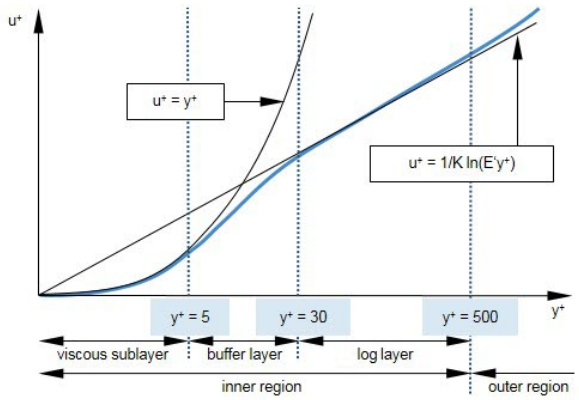

Figure 2.4: Non-dimensional velocity u^+ as a function of y^+ across the different sublayers [26].

2.4 Transition

2.4.1 Transition Effects on Flow over an Airfoil

Transition is the process whereby a flow changes from a laminar to turbulent one due to several natural perturbations (mechanical vibrations, surface irregularities, sound waves, amongst others) that affect the boundary-layer. Laminar-turbulent transition can sometimes be forced, for example to delay airflow separation, since turbulent boundary-layers have less momentum thickness [9].

At low Reynolds numbers, the flow over airfoils typically features laminar separation bubbles (Figure 2.5). These happen because the flow around the airfoil at low Reynolds numbers does not have enough energy to transition from laminar to turbulent with an attached boundary-layer. The laminar bubble is then located between the point at which separation of the laminar flow occurs and the point where the fully transitioned flow reattaches to the surface. These laminar bubbles result in an increase in pressure drag [28] and can also lead to an increase in the lift generated, due to an apparent increase in the camber of the airfoil [29], thus becoming an important trait of the airflow.

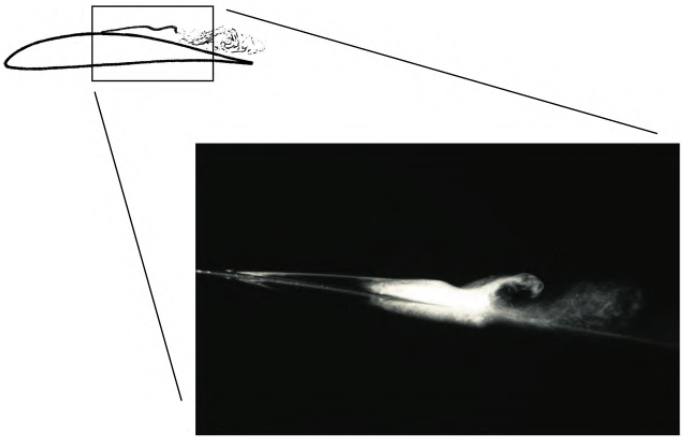

Figure 2.5: Smoke flow visualization of a laminar separation bubble [28].

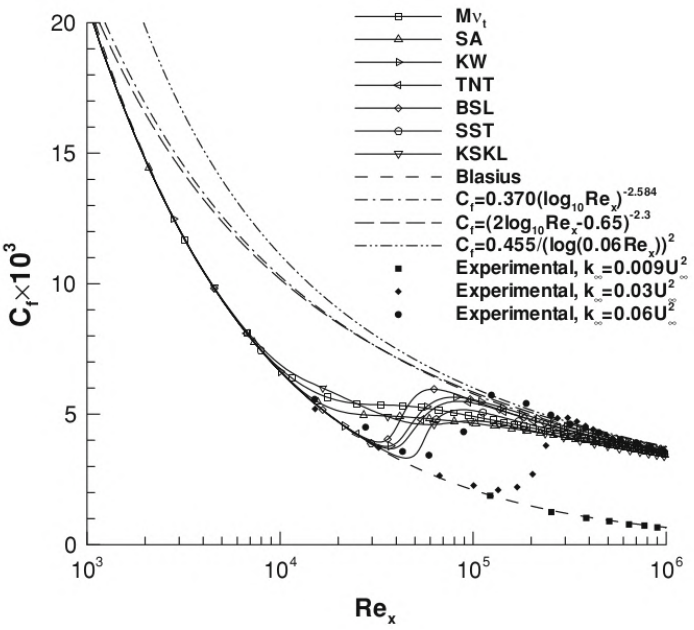

Figure 2.6: Transition in zero pressure gradient predicted by a variety of low-Reynolds number turbulence models. In all the models the flow is fully turbulent way before it does in reality [30].

2.4.2 Transition Model – Gamma ReTheta Transition

Most eddy viscosity turbulence models can predict transition, but they do it at lower Reynolds numbers than what can be seen in experimental data, as can be seen in Figure 2.6 [30]. In addition, they do not have the appropriate sensitivity to strong adverse pressure gradients and cannot predict transition well when there are separated shear layers [31]. Hence, they are not suited to properly determine the existence of laminar separation bubbles.

In order to identify where transition actually materializes, a transition model is needed. In STAR-CCM+, there are two approaches to calculate transition: a turbulent suppression model, or the Gamma Transition and Gamma ReTheta Transition models.

The Turbulent Suppression Model does not compute additional equations – it merely mirrors transition by suppressing turbulence in a predefined region. It is the fastest and least computationally expensive one, but requires that the transition location is already known. The Gamma Transition model is a simplification of the Gamma ReTheta Transition model, and as such is quicker and requires less computational power. It solves only for turbulence intermittency, providing a local method for the onset of transition [32].

The Gamma ReTheta Transition model is a two-equation, correlation-based transition model that is coupled with the SST *k*-ω model. It solves for both intermittency, γ, and transition momentum thickness Reynolds number, $\overline{Re_{\theta t}}$ (Equations (2.16) and (2.17) [33]). Intermittency measures the amount of time during which the flow is turbulent. When $\gamma = 1$, the flow is turbulent 100% of the time, whilst an intermittency $\gamma = 0$ means a fully laminar flow.

$$\frac{\partial(\rho\gamma)}{\partial t} + \frac{\partial(\rho U_j \gamma)}{\partial x_j} = P_\gamma - E_\gamma + \frac{\partial}{\partial x_j}\left[\left(\mu + \frac{\mu_t}{\sigma_f}\right)\frac{\partial \gamma}{\partial x_j}\right] \tag{2.16}$$

$$\frac{\partial(\rho\overline{Re_{\theta t}})}{\partial t} + \frac{\partial(\rho U_j \overline{Re_{\theta t}})}{\partial x_j} = P_{\theta t} + \frac{\partial}{\partial x_j}\left[\sigma_{\theta t}(\mu + \mu_t)\frac{\partial \overline{Re_{\theta t}}}{\partial x_j}\right] \tag{2.17}$$

where $P_{\gamma 1} = F_{length} c_{a1} = \rho S[\gamma F_{onset}]^{0.5}(1 - c_{e1}\gamma)$ and $P_{\theta t} = c_{\theta t}\frac{\rho}{t}(Re_{\theta t} - \overline{Re_{\theta t}})(1.0 - F_{\theta_t})$.

To use the γ-Re_θ model, special attention must be given to the mesh creation process, the turbulent specification on inflow boundary-conditions and convergence. The mesh usually requires y^+ values between 0.1 and 1. The turbulent specification must take into account the decay laws of the SST *k*-ω model. The convergence using this model will require more iterations since two more equations are being solved.

Chapter 3

Preliminary Tests

Before performing the CFD simulations of the concept proposed in this project, an assessment of the numerical error involved in the simulations was necessary. As such, the chapter begins with a description of the numerical accuracy. Then, a mesh convergence analysis was done, whose steps are stated, from the geometric model used to its results. At the end of the chapter, a comparison between the SST *k*-ωmodel and the GammaReTheta Transition model is shown to understand which is more suitable for the ensuing simulations.

3.1 Numerical Accuracy

The error of a variable $e(\phi)$ corresponds to the difference between an approximated solution ϕ_i and the exact solution ϕ_{exact}:

$$e(\phi) = \phi_i - \phi_{exact} \tag{3.1}$$

The numerical error has three main components: the round-off, iterative and discretization errors [34].

The round-off error is a consequence of the finite precision of computations using floating-point or integer values. To correctly calculate the round-off error, the exact solution of the problem is needed, which is generally not possible [34].

The iterative error can have different causes: the non-linear equations in the models used for the aerodynamic simulations; the use of segregated numerical methods; corrections used to obtain second order (or higher) approximations; and the fact that the system of linear equations used by the discretization methods are solved several times with iterative methods. The iterative error can only be reduced down to the round-off error and is commonly monitored recurring to the residuals of the equations and/or the differences in the variables' values in successive iterations [34].

The discretization error is a consequence of the transformation of the differential equations used by the mathematical models into a system of linear equations. It can also be affected by a geometric component, especially for small radii – such as an airfoil's leading edge. The discretization error is

commonly the main component of the numerical error and can, in most cases, be reduced by increasing the number of degrees of freedom. The discretization error is determined by mesh convergence studies, in which the other two errors are assumed to be negligible [34].

3.2 Mesh Convergence Analysis

3.2.1 Background

In the present work the discretization error is the largest component of the solution error. Thus, a mesh convergence study was done to evaluate it. Such a study estimates the exact numerical value and determines the uncertainty of the computed solutions [35]. This method requires that the solution of a quantity of interest be computed for three or more meshes. The first mesh can either be the coarsest or the most refined, which is then progressively refined/coarsened, according to a specific refinement/coarsening factor. Normally $r = 2$ or $r = 1/2$, in what is called grid doubling or halving, respectively, but can have different values [36].

$$r = \left(\frac{N_1}{N_2}\right)^{1/d} \tag{3.2}$$

where N_k is the number of elements on mesh k and d is the number of dimensions of the problem.

The estimation of the exact solution of the problem is most often done via extrapolation. A frequent method used is the Richardson extrapolation, which gives an estimate of the exact solution by calculating a solution to the problem as if the mesh was infinitely refined. This extrapolation method requires assumptions to yield reliable estimations [36]:

- The discrete solutions are in the asymptotic range (the sequence of systematically refined meshes whose discretization error reduces at the formal order of accuracy of the discretization scheme);
- The refinement is systematic, i.e., it has to be uniform and consistent. Uniform refinement mandates that the mesh must be refined by the same factor over the entire control volume[1]. Consistent refinement has to do with the grid quality[2] which should be the same or higher with increasing refinement;
- The solutions are smooth – the dependent variables or their derivatives do not have discontinuities;
- The other error components are small – at least two orders of magnitude smaller than the discretization error in the solution of the finest mesh.

Then, to calculate the discretization error ϕ, it is assumed that it has the following behaviour [34]:

$$e(\phi_i) = \phi_i - \phi_{exact} = \alpha h_i^p \quad \Rightarrow \quad \phi_i = \phi_0 + \alpha(hi/h_1)^p \tag{3.3}$$

[1]The use of locally-refined meshes, meshes refined in only one coordinate direction, and refinement whose refinement factor varies locally over the domain are all examples of improper approaches to mesh refinement [36].

[2]Examples of mesh quality criteria: skewness angle, cell aspect ratio, warpage, volume change, etc.

where ϕ_i is the solution for the i mesh; ϕ_{exact} is the exact solution; ϕ_0 is the estimate of the exact solution; α is a constant: h_i is the mesh size and p is the convergence order.

3.2.2 Geometry Model

The geometry chosen for these studies was the geometry of the rear wing of FST Lisboa's FST09e car, which is also the basis for this project. It has a main plane, two flaps and an endplate (Figure 3.1). The airfoil used in the main element and in the flaps is the Selig S1223. The wing has a total chord of $c_t = c_{main} + 2 \times c_{flap} = 0.4 + 2 \times 0.2 = 0.8m$; and a span of $b = 0.9m$, for a total wing area $S = 0.72m^2$ and an aspect-ratio $\mathit{AR} = 1.125$.

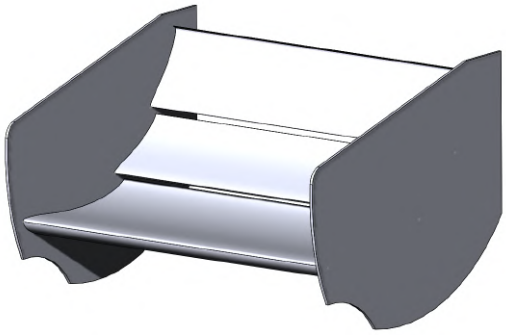

Figure 3.1: Geometry used for the mesh convergence analysis.

The simulation was done with just half a wing due do its symmetry, halving the number of cells needed for any given simulation and consequently its computational penalty. The domain was made large enough to ensure that the exterior boundaries would not affect the airflow near the wing (Figure 3.2), whereby the flow inlet is $\approx 5L$ forward of the wing, and the outlet is $\approx 10L$ aft of it (with $L = c_t$). The wing's height from the ground is the same as when mounted on the car, $h \approx 0.78m \approx L$ (from the leading edge of the main element).

Figure 3.2: Domain used in the CFD simulations.

3.2.3 Volume Mesh Generation

The model is simple enough that it did not require any clean-up or special preparation before importing it in Star-CCM+. To create the control volume, first a bounding box with the aforementioned dimensions was created and then a boolean subtract operation was performed. The boolean subtract operation ensures that the volume has no gaps or holes, eliminating the need for a surface wrapper operation before the mesh generation, a process that is usually time-consuming.

Star-CCM+ has three main meshers: Tetrahedral, Polyhedral and Trimmed, represented in Figure 3.3. Choosing one mesh type model depends on factors such as the time available for meshing, desired solution accuracy and convergence rate, how much memory is available, amongst others. Considering those factors, the trimmed mesher was used.

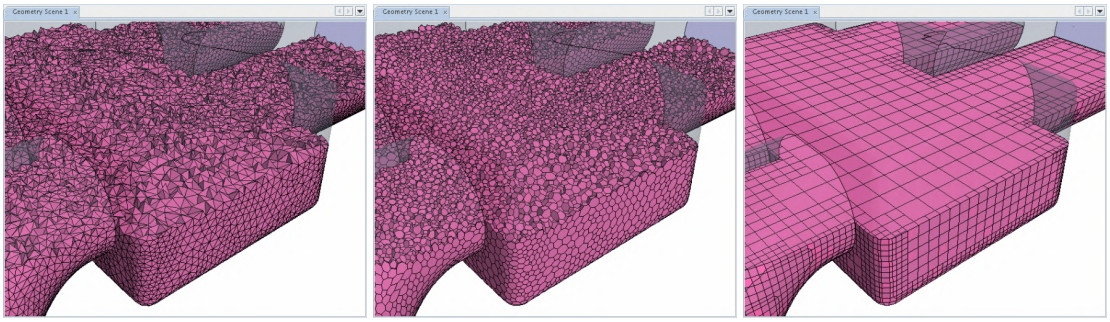

(a) Tetrahedral mesher. (b) Polyhedral mesher. (c) Trimmed mesher.

Figure 3.3: Three types of core mesh on the same geometry [26].

No local refinement was employed; instead, the parameter that regulates the cell growth away from the surfaces was changed to slow, meaning that the mesher uses several layers of cells of the same size to produce a gradual transition from the surfaces to the core. Prism layers were added to all the wing's surfaces, so that the flow near them could be better resolved, as explained in section 2.3. These mesh features can be seen in Figure 3.4. The surface remesher option was also enabled to safeguard the quality of the surface mesh upon which the volume mesh is generated.

The starting point of the mesh convergence study was the coarsest mesh. To refine the mesh on the surfaces, the target surface size on the wing surface was the most important parameter and had to be changed in each refinement step. This is the case because the trimmed mesher in Star-CCM+ multiplies the size of the cells by two and uses the target surface size as its initial value [26]. To comply with the systematic refinement requirement, the same total height was kept in the region where the prism layers were generated in all five meshes; the number of layers was increased so that the refinement occurred in all the three dimensions (on the surface and direction perpendicular to it). The total height value was nonetheless chosen in a way that guaranteed that the y^+ on the wing surface was $y^+ = 1$ (Figure 3.5).

3.2.4 Numerical Setup – Models and Boundary Conditions

In Star-CCM+ the models used in a simulation are defined in a *Physics Continuum*. These comprise the equation of state, dimensionality of the problem, flow type and others. The complete list of settings

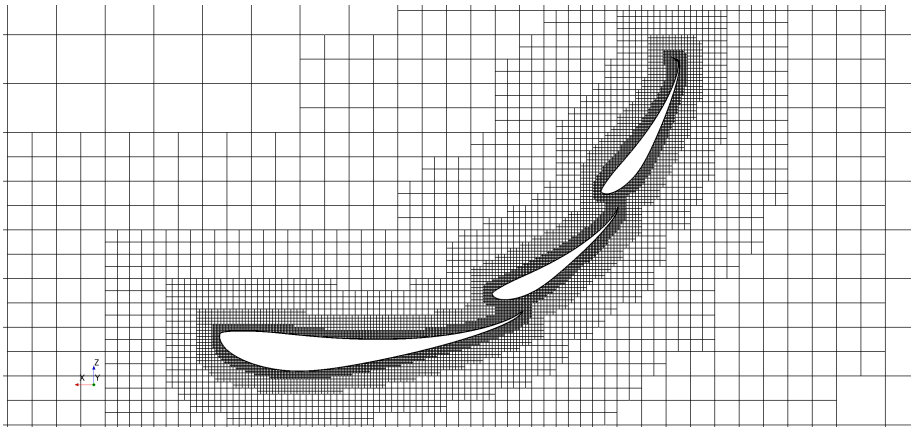

(a) Mesh on symmetry plane.

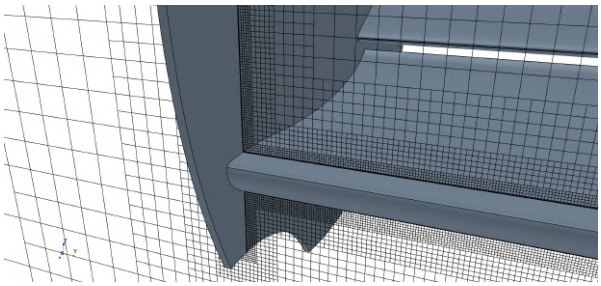

(b) Slow growth away from the surface with several layers of cells of the same size.

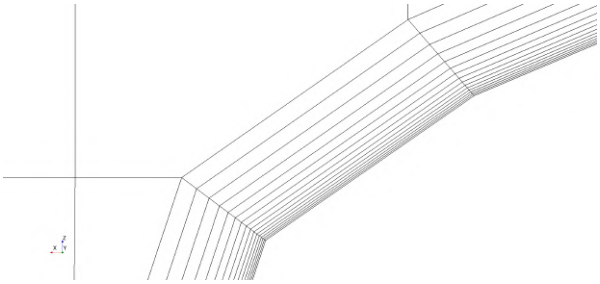

(c) Prism layers near the wall.

Figure 3.4: Mesh features of the wing model.

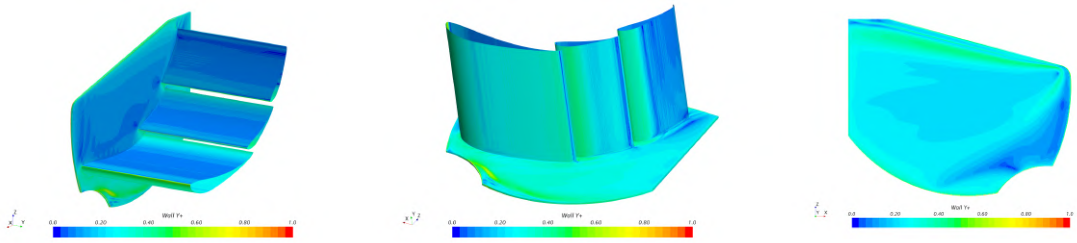

(a) (b) (c)

Figure 3.5: y^+ contour on the wing surfaces-

used in the mesh convergence analysis is given in Table 3.1.

In terms of boundary conditions, which can be seen in Figure 3.6, these are as follows:

- The inlet is defined as a velocity-inlet. The velocity magnitude is $V_{inlet} = 15m/s$;
- The outlet is a pressure outlet, with the pressure being set to $0Pa$ (Gauge);
- The ground is a no-slip wall that moves at the same velocity as the airflow, $V_{ground} = V_{inlet}$;
- The top and side boundaries, because they are far away from the wing, are defined as symmetry planes;
- The symmetry boundary is a symmetry plane;
- The wing's surfaces are defined as stationary ($V_{wing} = 0m/s$) no-slip walls.

- All y^+ Wall Treatment
- Constant Density
- Gas
- Gradients
- Steady
- Three Dimensional
- Segregated Flow
- Turbulent
- Wall Distance
- K-Omega Turbulence
- RANS
- Solution Interpolation
- SST (Menter) K-Omega

Table 3.1: List of settings used in Star-CCM+.

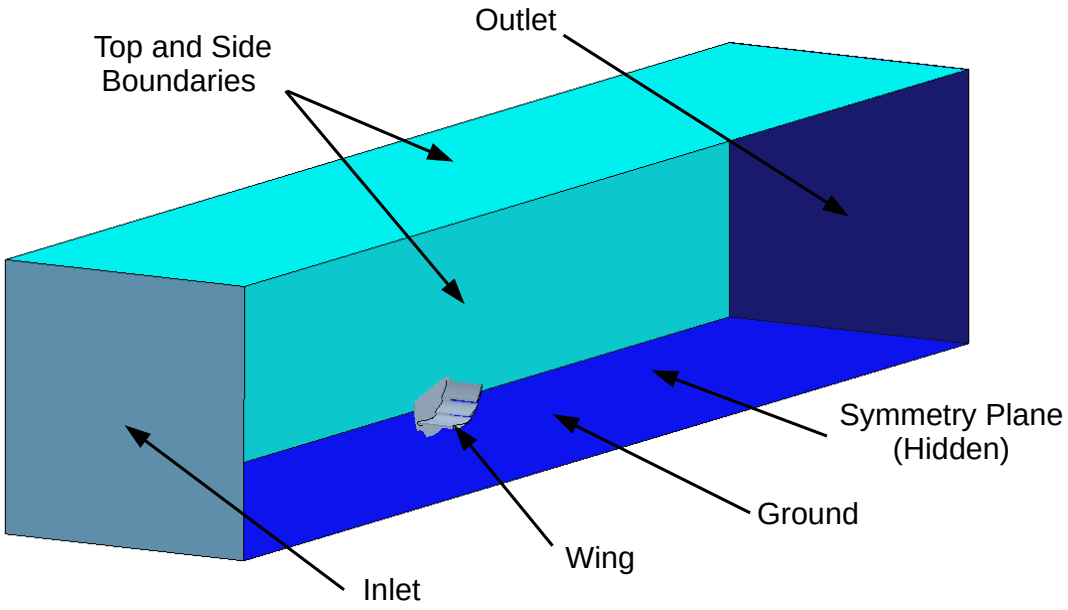

Figure 3.6: Boundary conditions.

3.2.5 Results

The convergence analysis was done with five different meshes, with the total element count ranging from about 1.5 to 9 million elements. The quantities of interest to perform the analysis were the lift and drag coefficients of the wing. The residuals of one of the simulations are in Figure 3.7 and the data from the mesh convergence analysis is displayed in Table 3.2.

Using the aforementioned Richardson extrapolation, the exact solution was estimated as well as its error constant. These values are presented in Table 3.3 while the data is pictured against the Richardson extrapolation in the plots of Figure 3.8.

The data obtained with the mesh convergence analysis had some noise due to the definition of r, since it is difficult ensure the same r in each refinement step of an unstructured trimmed (hexahedral)

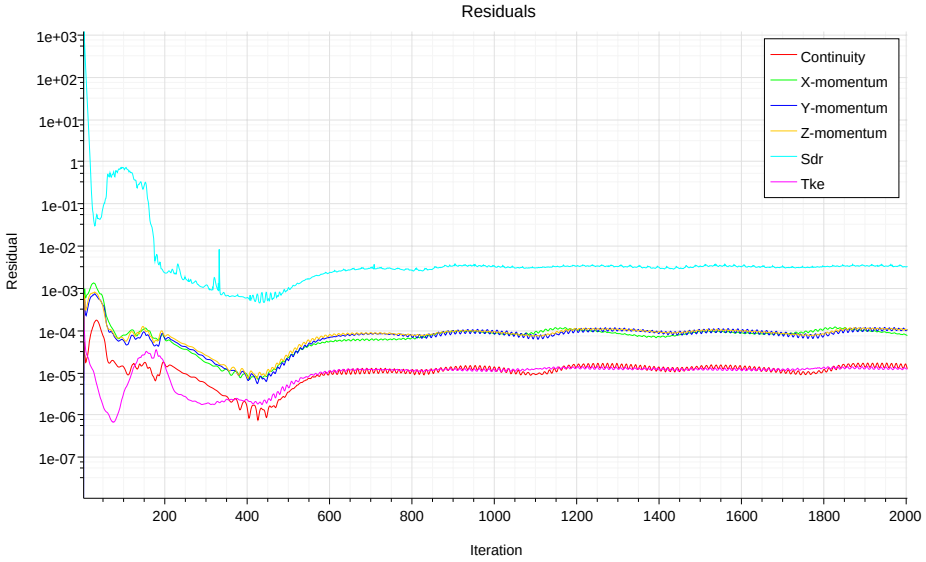

Figure 3.7: Residuals of the solution with the fine mesh.

Mesh	Mesh Parameters					Results	
	TSS [mm]	NPL	PLIH [mm]	NE ($\times 10^6$)	r	C_L	C_D
Coarse	4	7	0.0462	1.5	—	2.617	1.068
Medium-Coarse	3.5	8	0.0362	2.1	1.12	2.637	1.083
Medium	3	10	0.0230	3.2	1.27	2.626	1.073
Medium-Fine	2.3	13	0.0123	5.9	1.57	2.627	1.078
Fine	2	15	0.0083	8.7	1.78	2.600	1.064

Table 3.2: Data retrieved from the mesh convergence analysis. TSS is the target surface size; NPL is the number of prism layers; PLIH is the prism layer initial height; NE is the number of elements in the mesh; and r is the refinement factor, $r = \sqrt[3]{h_i/h_1}$.

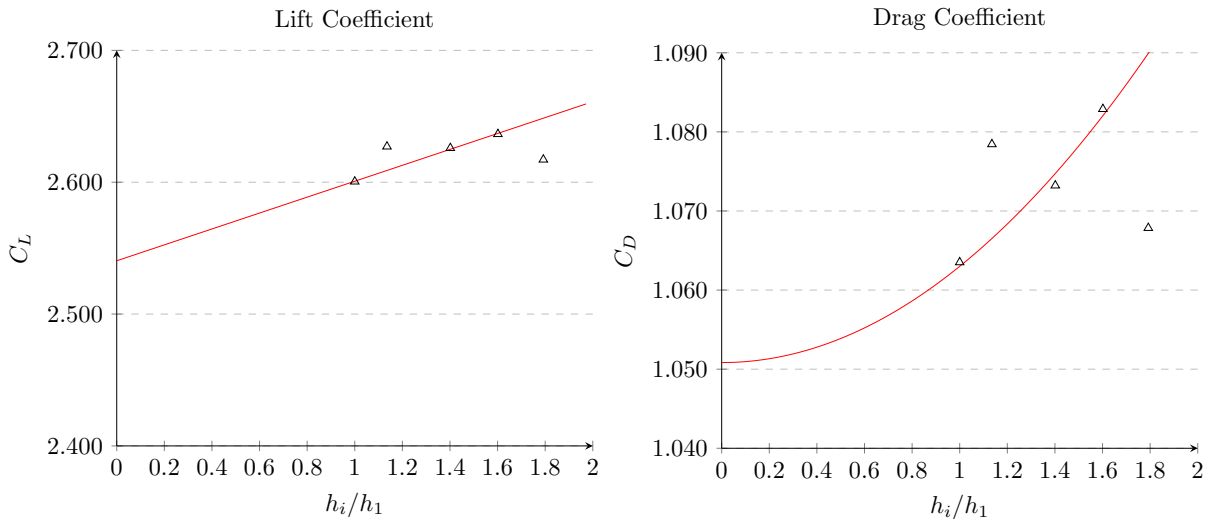

(a) Lift coefficient.

(b) Drag coefficient.

Figure 3.8: Plots of the mesh convergence analysis. The intersection of the curve with the y-axis is the estimation of the exact solution.

	C_L	C_D
Exact Solution Estimation	2.540	1.051
Estimated Error	6.034×10^{-2}	1.217×10^{-2}

Table 3.3: Guess of the exact solution and error constant of the mesh convergence analysis.

mesh. Nonetheless, the estimated numerical errors are close to or smaller than 1%. Based on these results, the mesh used for the next simulations was the fine mesh.

3.3 γ-Re_θ Transition Model

The simulations done for the mesh convergence analysis made use of the SST *k*-ω turbulence model, which generally predicts the onset of transition at around $Re = 5 \times 10^4$ [30], below the natural transition Reynolds number.

So in the case of the wing, the skin friction coefficient, $C_f = \frac{\tau_w}{1/2\rho V^2}$, and the pressure coefficient were plotted along the direction of the airflow in Figure 3.9. In the C_f plot there is a peak at $x \approx 1.35$, right after the leading-edge of the main element of the wing. This means that at that point the transition from laminar to turbulent flow had already occurred, which corresponds to $x_{crit} = 0.025c_t$. This can be further corroborated by looking at the turbulent kinetic energy, k, contour on the symmetry plain near the main element's leading edge (Figure 3.10). The production of k begins immediately after the leading edge, indicating that the flow transitions from laminar to turbulent very rapidly. This should not be the case, given that at that point there was a favorable pressure gradient in the suction side of the wing, as illustrated in Figure 3.9b.

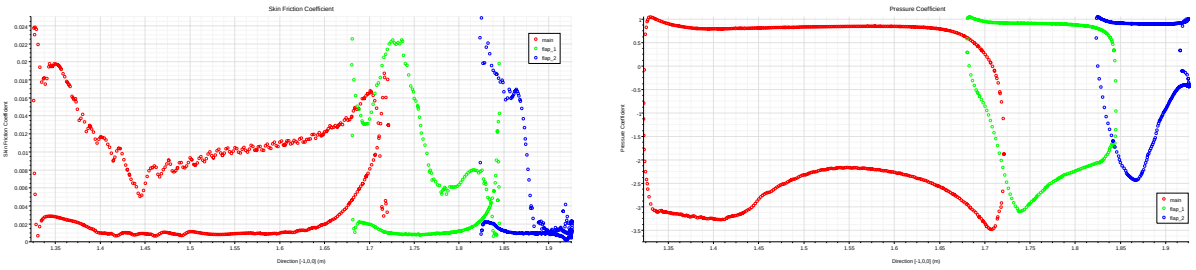

(a) Skin friction coefficient.

(b) Pressure coefficient.

Figure 3.9: Plots of the k-ω model at $y = 0.5b$.

For these reasons, a different set of simulations was done to investigate whether the transition really occurred at $x = 0.025c_t$ and if laminar separation occurred on the wings' surfaces. With this in mind, the γ-Re_θ transition model was used. The mesh chosen via the convergence mesh study was used here again.

The γ-Re_θ model revealed a different location for the transition, at $x_{crit} \approx 0.15c_t$. Besides, the transition occurs with a laminar separation bubble. This can be seen in the C_f plot of Figure 3.11a where $C_f = 0$ at the x_{crit}. Moreover, at that same coordinate there is a jump in the C_p (Figure 3.11b) that did not exist in the case of the *k*-ω model (Figure 3.9b). The C_p values are higher in magnitude too

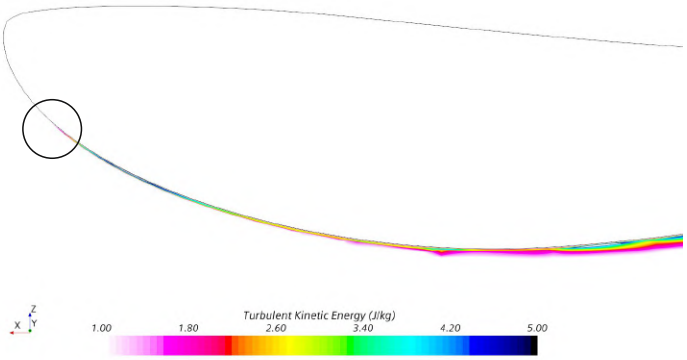

Figure 3.10: TKE contour on symmetry plain near the leading edge of the wing's main element for the *k*-ω model. Area where transition occurs highlighted by the circle.

when compared with the *k*-ω model.

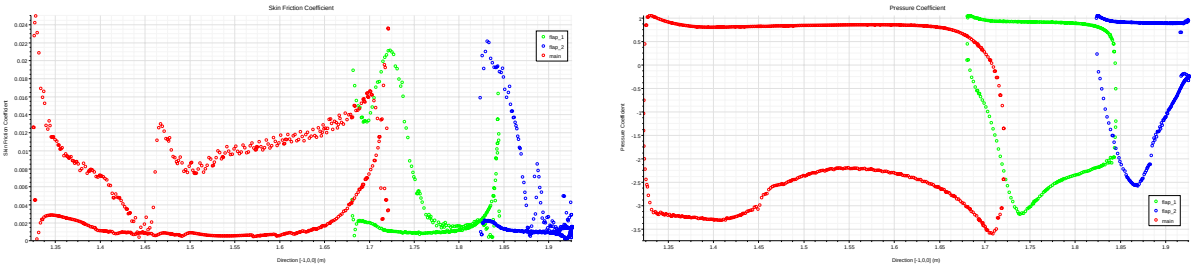

(a) Skin friction coefficient.

(b) Pressure coefficient.

Figure 3.11: Plots of the *k*-ωmodel at $y = 0.5b$.

Once more the TKE contour on the symmetry plane was drawn near the main element of the wing (Figure 3.12). The TKE production starts much more rearward than with the *k*-ω model (Figure 3.10), revealing that the transition only occurs at that point simultaneously with the separation bubble.

The differences in the flow with the two models are further evidenced when looking at the pressure coefficient and wall shear stress distributions of Figures 3.13 and 3.14:

- The C_p of the simulation with the γ-Re_θ transition model is lower in larger patches of the wing than with the SST *k*-ω model, especially near the symmetry plane at the leading-edge of the wing and at the trailing edge of the main element over the entire wing-span.
- The wall shear stress on the low-pressure side of the wing shows that the separation occurs over the entire span of the main-element with the γ-Re_θ model, represented by the dark-blue strip ($WSS = 0Pa$) after the leading-edge. The area underneath the flaps also has significant differences, especially on the first flap.

Finally, the lift and drag coefficients of the γ-Re_θ model are compared with those of the *k*-ω model in Table 3.4. The difference for both is within the error estimation of the previous section. However, given that the physics of the flow is different, the γ-Re_θ model had to be chosen for the remainder of the projects' simulations.

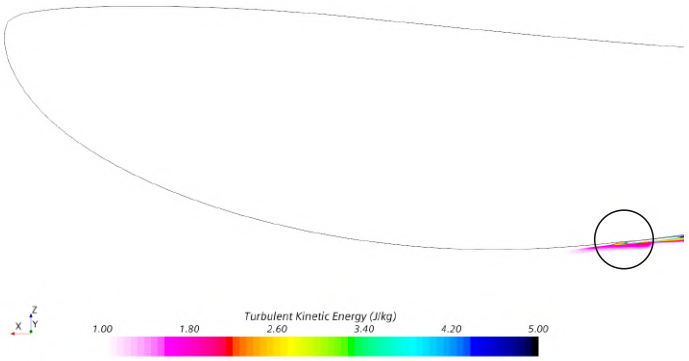

Figure 3.12: TVR contour on symmetry plain near the leading edge of the wing's main element of the γ-Re_θ model. Area where transition occurs highlighted by the circle.

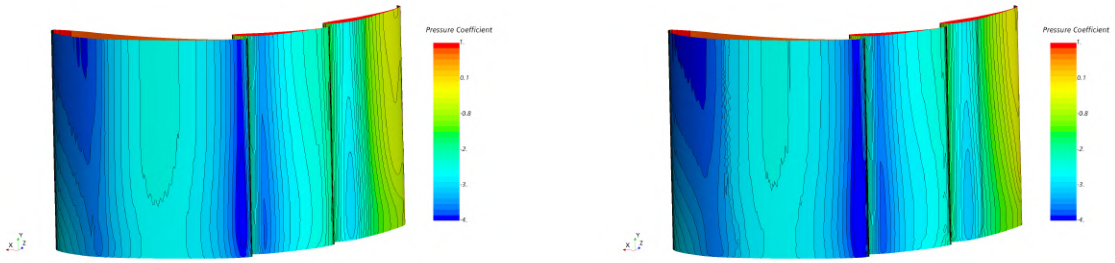

(a) SST *k*-ω model.

(b) γ-Re_θ transition model.

Figure 3.13: Pressure coefficient distribution on the underside of the wing.

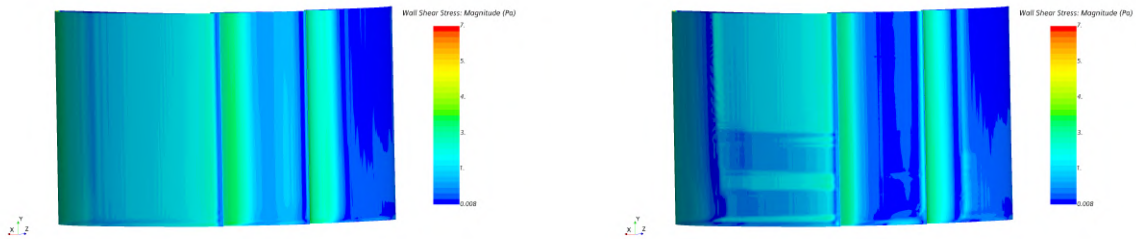

(a) SST *k*-ω model.

(b) γ-Re_θ transition model.

Figure 3.14: Wall shear stress contour on the underside of the wing. Air flows from left to right.

Model	C_L	Δ%	C_D	Δ%	C_L/C_D	Δ%
SST *k*-ω	2.600		1.064		2.445	
γ-Re_θ	2.660	+2.308	1.097	+3.101	2.425	-0.818

Table 3.4: Comparison between the SST *k*-ω and γ-Re_θ models.

Chapter 4

Assessing the Effect of Wing Tip Endplates with CFD

4.1 Geometry Model

Initially the simulations were done with a different geometry model. On the one hand, this simplifies the design process; on the other hand it facilitates understanding the effect the design changes to the endplates had on the overall performance of the wing. The model had just a main element and an endplate. The main element has the same chord as the one in the wing model of the mesh convergence analysis and features a Selig S1223 airfoil at an angle of attack $\alpha = 5^{\circ}$.

The endplate begins and ends, respectively, on the leading edge and the trailing edge of the wing's airfoil. It is also defined by two vertical coordinates, one above the trailing edge of the wing, one below the lowest airfoil point (Figure 4.1). These were also a variable of interest in trying to reach the best efficiency possible in terms of C_L/C_D.

Figure 4.1: Variable dimensions of the endplate analyses.

4.2 Flat Endplate Versus Airfoils

The first simulations were done with two geometries. A flat endplate (the usual design) and an endplate with curvature. To add the curvature to the endplates, the airfoils of the NACA 4-Digit Series were used due to their simplicity and overall good general applicability. Their nomenclature is as follows: the first digit is the camber of the airfoil, the second the position of maximum camber, and the last two its thickness. So for example, the 2412 airfoil has the following characteristics:

1. the first digit is the camber of the airfoil, 2% ($0.02c$);
2. the second digit 4 means that the maximum camber occurs at 40% ($0.4c$) of the chord from the leading edge;
3. the last two digits 12 represent the thickness of the airfoil in percentage ($t = 0.12c$).

The first simulations were done with a flat endplate and the 2412 aifoil with the following dimensions: $top = 0mm \vee bottom = 50mm$ and $top = bottom = 50mm$, the results of which are given in Table 4.1. In the case of $top = 0mm \vee bottom = 50mm$, the C_L is larger and the C_D smaller for the flat endplate, resulting in a higher C_L/C_D than that of the 2412 endplate . With $top = bottom = 50mm$, the C_L of the flat endplate was still larger, but the C_D was higher too. The consequence is that the 2412 endplate now has an efficiency only 1.65% smaller than that of the flat endplate. Despite the increase in C_L/C_D and lower C_D , the C_L of the 2412 endplate falls short of that of the flat endplate by 8.3%. A factor could have been the decrease in span of the main element due to the airfoil thickness, since the wing's overall span has to stay the same due to the rules constraint mentioned in subsection 1.4.2. Therefore, the same two variants of the endplate were simulated with a thinner airfoil, the 2402, whose results are also in Table 4.1. Concerning the $top = 0mm \vee bottom = 50mm$ combination, the thinner 2402 airfoil compares favorably against the flat endplate: higher C_L , identical C_D and a higher C_L/C_D . When increasing the top dimension, though, both the C_L and C_D are smaller than those of the flat endplate, with the C_L/C_D still larger owing to a bigger decrease in the C_D .

Endplate	Bottom [mm]	Top [mm]	Lift [N]	Drag [N]	C_L	C_D	C_L/C_D
Flat	50	00	24.911	3.507	1.056	0.149	7.102
		50	26.575	3.567	1.127	0.151	7.450
2412	50	00	24.470	3.570	1.037	0.151	6.854
		50	24.376	3.327	1.033	0.141	7.327
2402	50	00	25.224	3.518	1.069	0.149	7.170
		50	25.787	3.430	1.093	0.145	7.519

Table 4.1: Results of the first simulations.

Upon seeing the airflow of the 2402 and flat endplates, it was noted that the vortices generated by the 2402 endplate were at an identical distance from the chord line, as illustrated in Figure 4.2. Consequently their combined effect vanished, and thus only slight to no improvements in the performance of the wing were observed. To test this hypothesis, two sets of simulations were done, using both the flat and 2402 endplates:

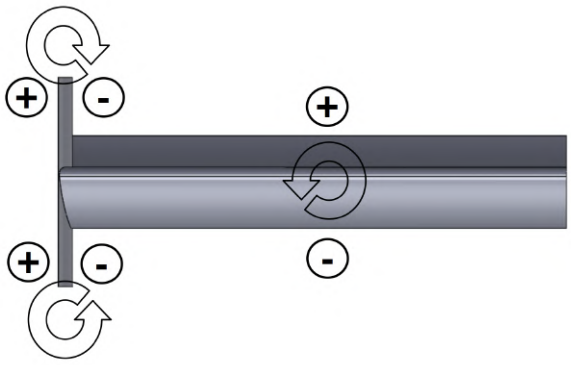

Figure 4.2: Orientation of the vortices generated by the main plane and endplate. Wing in front view.

- Fixing the top coordinate to $top = 50mm$, the bottom coordinate was incremented in 50mm steps until $bottom = 200mm$;
- The same procedure was done but in the opposite direction: $bottom = 50mm$ and $top = 100mm, top = 150mm, top = 200m$.

The forces' and coefficients' values are in Tables 4.2 and 4.4; further, the components of the drag are shown in Tables 4.3 and 4.5.

Endplate	Top [mm]	Lift [N]	Drag [N]	C_L	C_D	C_L /C_D
Flat	100	25.801	3.449	1.094	0.146	7.481
	150	26.221	3.460	1.112	0.147	7.578
	200	26.532	3.468	1.125	0.147	7.651
2402	100	26.138	3.404	1.108	0.144	7.679
	150	26.487	3.404	1.123	0.144	7.781
	200	26.610	3.361	1.128	0.142	7.917

Table 4.2: Results for fixed dimension $bottom = 50mm$.

Geometry	Part	Drag Component			C_D Components		
		$D_{pressure}$ [N]	$D_{viscous}$ [N]	D_{total} [N]	$C_{D_{pressure}}$	$C_{D_{viscous}}$	$C_{D_{total}}$
Flat	Endplate	0.362	0.111	0.474	0.015	0.005	0.020
	Main	2.885	0.110	2.994	0.122	0.005	0.127
	Total	3.247	0.221	3.468	0.138	0.009	0.147
2402	Endplate	0.167	0.093	0.260	0.007	0.004	0.011
	Main	3.002	0.099	3.101	0.127	0.004	0.131
	Total	3.169	0.192	3.361	0.134	0.008	0.142

Table 4.3: Drag components of the Flat and 2402 endplates with $top = 200mm$ and $bottom = 50mm$.

The changes in the dimensions brought significant differences between the two endplate designs, with the 2402 endplate generally displaying identical or better C_L , C_D and C_L/C_D values. Changing the top dimension resulted in slightly larger C_L and smaller C_D values of the 2402 endplate in comparison with the flat endplate, leading to slightly higher C_L/C_D values. This trend is more pronounced when

Endplate	Bottom [mm]	Lift [N]	Drag [N]	C_L	C_D	C_L/C_D
Flat	100	26.295	3.466	1.115	0.147	7.587
	150	27.177	3.512	1.152	0.149	7.738
	200	27.826	3.548	1.180	0.150	7.843
2402	100	27.072	3.420	1.148	0.145	7.916
	150	28.115	3.389	1.192	0.144	8.296
	200	28.981	3.348	1.229	0.142	8.656

Table 4.4: Results of the fixed dimension $top = 50mm$.

Geometry	Part	Drag Component			C_D Components		
		$D_{pressure}$ [N]	$D_{viscous}$ [N]	D_{total} [N]	$C_{D_{pressure}}$	$C_{D_{viscous}}$	$C_{D_{total}}$
Flat	Endplate	0.398	0.133	0.531	0.017	0.006	0.023
	Main	2.906	0.112	3.017	0.123	0.005	0.128
	Total	3.304	0.245	3.548	0.140	0.010	0.150
2402	Endplate	0.076	0.104	0.180	0.003	0.004	0.008
	Main	3.054	0.114	3.168	0.129	0.005	0.134
	Total	3.130	0.218	3.348	0.133	0.009	0.142

Table 4.5: Drag components of the Flat and 2402 endplates with $top = 50mm$ and $bottom = 200mm$.

increasing the bottom dimension. The C_D values are similar to those of increasing top dimension, but the increase in C_L is more noticeable, with the gains in term of C_L/C_D evident, reaching a maximum increase of 10.4% for the $top = 50mm \vee bottom = 200mm$.

The placement of the endplate relative to the main plane affects the strength of the tip vortices of the wing assembly, as can be seen in the vorticity countour of Figure 4.3. Moving the endplate upward leads to a stronger lower vortex and a weaker top vortex, while the opposite happens when the endplate is moved downward. Since the strengthening of one of the vortices comes with a decrease in the intensity of the other, the two configurations have similar C_D .

Looking at the different drag components, the introduction of the airfoil to the endplate reduces the wing's overall drag by reducing the endplate's pressure and viscous drag. This is again intensified in the case of the $top = 50mm \vee bottom = 200mm$. The viscous and pressure drag values of the main wing increase somewhat with the 2402 endplate, however, resulting in a larger main wing total drag. Still, this increase is not enough to offset the drag reduction of the endplate.

The difference in lift coefficient seems to come from the different pressure distribution of the low-pressure side of the wing Figure 4.4. The isobaric lines of the $top = 50mm$ configuration are closer to being parallel than those of the $bottom = 50mm$ design. Not only that, but the magnitude of the C_p values on the underside of the wing are higher in the first configuration, especially near the tip of the wing. This will inevitably result in a higher lift coefficient.

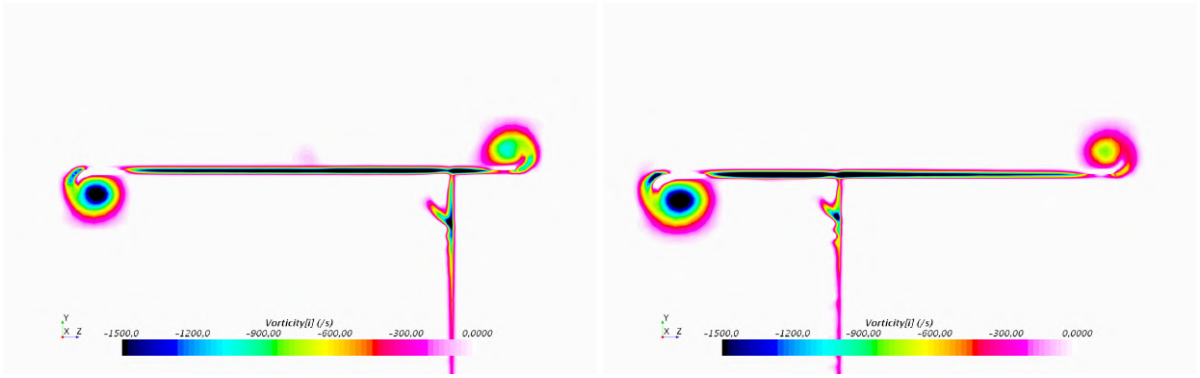

(a) Top=50, bottom=200.

(b) Top=200, bottom=50.

Figure 4.3: Vorticity countour at $x = 400mm$ of the 2402 endplate.

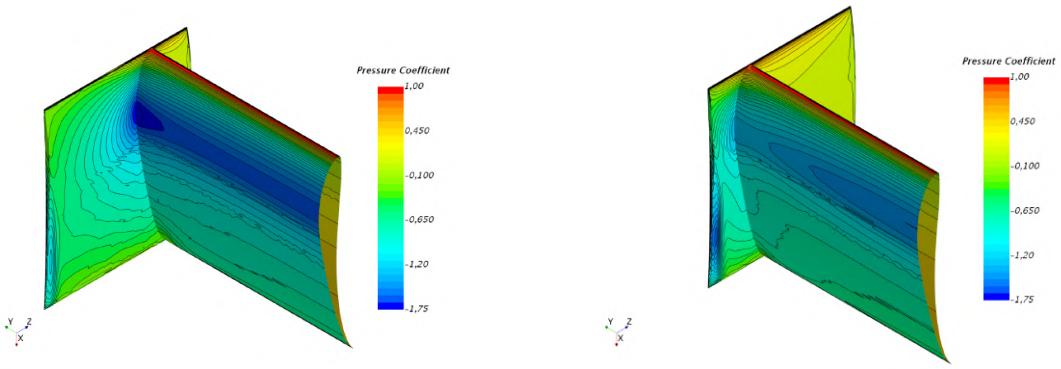

(a) Top=50, bottom=200.

(b) Top=200, bottom=50.

Figure 4.4: Pressure coefficient contour on the underside of the wing.

4.3 Four Endplate Designs – Comparison

After seeing these results, the same three bottom coordinates were tested for another two endplate designs: the gurney flap, the solution usually used by Formula Student teams; and the NACA2402 with negative camber (2402inv), to seek maximum efficiency according to the hypothesis tested beforehand. The four endplate designs are shown side-by-side in Figure 4.5. The results of those two geometries are in Table 4.6 which are then compared with the other two in the plots of Figure 4.6.

Endplate	Bottom [mm]	Lift [N]	Drag [N]	C_L	C_D	C_L/C_D
Gurney Flap	100	26.791	3.763	1.136	0.160	7.120
	150	27.776	3.824	1.177	0.162	7.264
	200	28.577	3.884	1.211	0.165	7.358
2402inv	100	25.432	3.080	1.078	0.131	8.257
	150	26.065	3.069	1.105	0.130	8.493
	200	26.532	3.091	1.125	0.131	8.584

Table 4.6: Values of the gurney flap and inverted NACA2402.

When analysing the lift coefficient plot in Figure 4.6a, the endplate with the 2402 airfoil has the highest C_L values followed by the endplate with the gurney flap, the flat endplate and then the inverted 2402 airfoil. The fact that the gurney flap increases the C_L so much and close to the 2402 airfoil corroborates

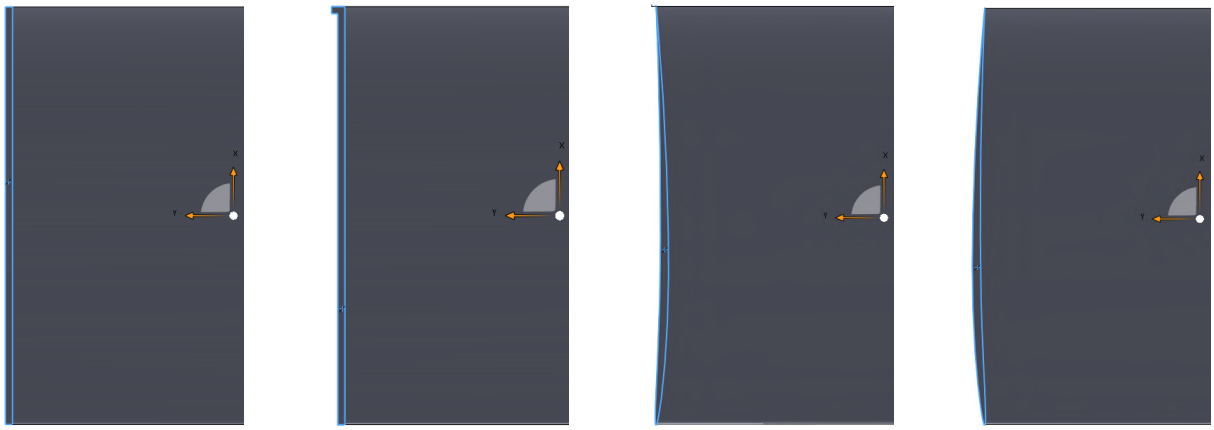

(a) Flat endplate. (b) Gurney flap. (c) NACA2402. (d) NACA2402inv.

Figure 4.5: Final endplate designs for comparison.

Geometry	Part	Drag Component			C_D Components		
		$D_{pressure}$ [N]	$D_{viscous}$ [N]	D_{total} [N]	$C_{D_{pressure}}$	$C_{D_{viscous}}$	$C_{D_{total}}$
Gurney Flap	Endplate	0.654	0.123	0.777	0.028	0.005	0.033
	Main	2.996	0.112	3.107	0.127	0.005	0.132
	Total	3.650	0.235	3.884	0.155	0.010	0.165
2402inv	Endplate	0.119	0.107	0.226	0.005	0.005	0.010
	Main	2.756	0.109	2.865	0.117	0.005	0.121
	Total	2.875	0.216	3.091	0.122	0.009	0.131

Table 4.7: Drag components of the Gurney Flap and 2402inv endplates with $top = 50mm$ and $bottom = 200mm$.

the theory that its effect is similar to that of the airfoil in terms of giving a camber to the endplate.

Regarding the C_D values, plotted in Figure 4.6b, the lowest value corresponds to the 2402inv, then the 2402 endplate, the flat endplate and finally the gurney flap by a big margin. The largest C_D value of the gurney flap is a consequence of how the lift increase is obtained, namely due to a separation on its rearward face. This is validated by the drag components in Table 4.7, where the drag of the endplate increases dramatically, especially its pressure component due to the separation. Interestingly the trends of the values are opposite: the C_D of the flat plate seems to stabilize with increasing bottom coordinate, while the 2402 is decreasing and the 2402inv increasing.

Finally, the efficiency of the four endplates is measured with the lift over drag values of Figure 4.6c. Here, despite the large lift coefficient, the gurney flap has the lowest efficient due to its high C_D coefficient and the flat endplate is consistently the third most efficient wing. Regarding the two airfoil designs, in the first two bottom coordinates the inverted comes ahead, but is then overtaken by the normal 2402 airfoil. The large efficiency values of the 2402inv endplate are by virtue of the marked reduction in its lift coefficient.

The pressure distribution in the low-pressure surface of the wing is presented in Figure 4.7. There are obvious differences across the 4 designs. The addition of the gurney flap on the trailing edge of the endplate decreases the C_p on the underside of the wing, an effect exacerbated when the NACA2402 was used, especially near the wing tip (due to the bi-directional flow acceleration on the endplate and

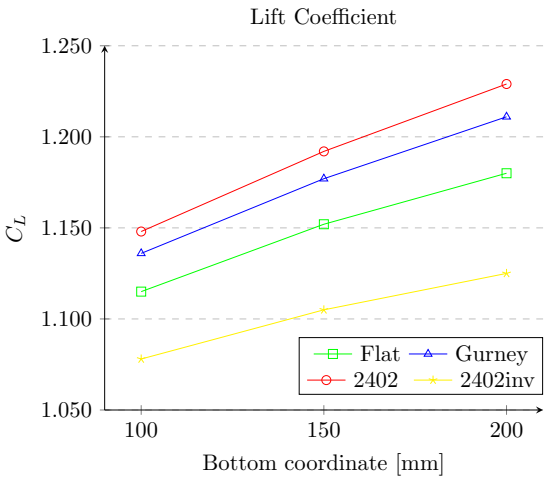

(a) Lift coefficient.

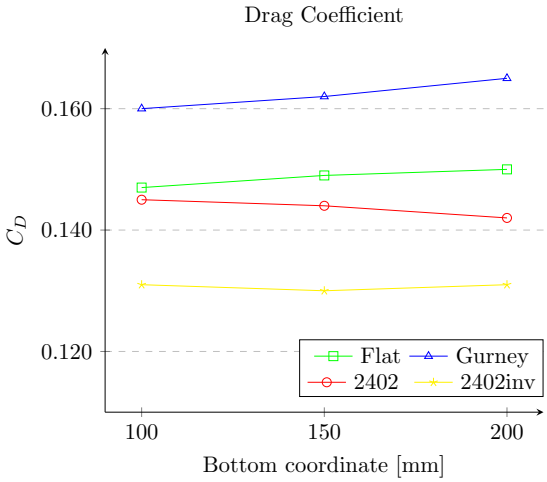

(b) Drag coefficient.

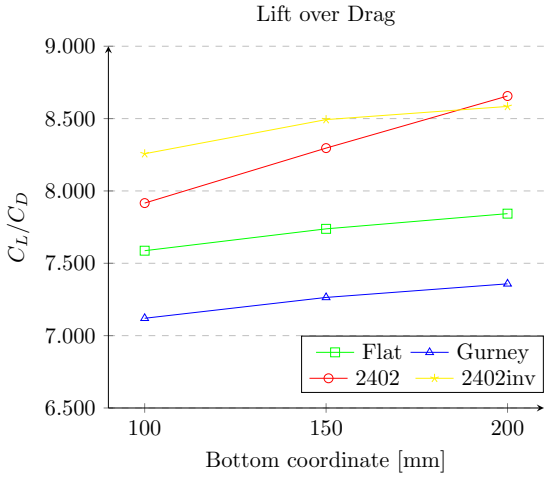

(c) Lift over drag.

Figure 4.6: C_L , C_D and C_L/C_D values of the four endplate designs.

main element). The isobaric lines of the latter also run parallel practically from the root to the tip, meaning that the entire span of the main element is equally loaded, something that is not seen in any of the other three wings, hence the largest lift coefficient of the 2402 endplate. The NACA2402inv actually has an increase in the C_p .

The pressure distribution on the high-pressure surface of the different designs is shown in Figure 4.8. In this case the contours remain practically unchanged regardless of the design, except for the inverted NACA2402 endplate (Figure 4.8d) where the pressure side of the main element matches the pressure side of the endplate, the result being that the isobaric lines are streched to the endplate in a similar fashion to what happened with the low pressure side of the NACA2402 endplate (Figure 4.7c).

The airflow around the four endplates can once again be analysed with the vorticity around them (Figure 4.9). Starting from the flat endplate, the addition of the gurney flap stregthens the lower vortex and weakens the top one, an effect that is reinforced with the NACA2402 endplate. Moreover, the increased vorticity due to the curvature of the NACA2402 airfoil originates a vortex near the tip of the wing on the underside of the wing. The inverted NACA2402 does the opposite, strengthening instead

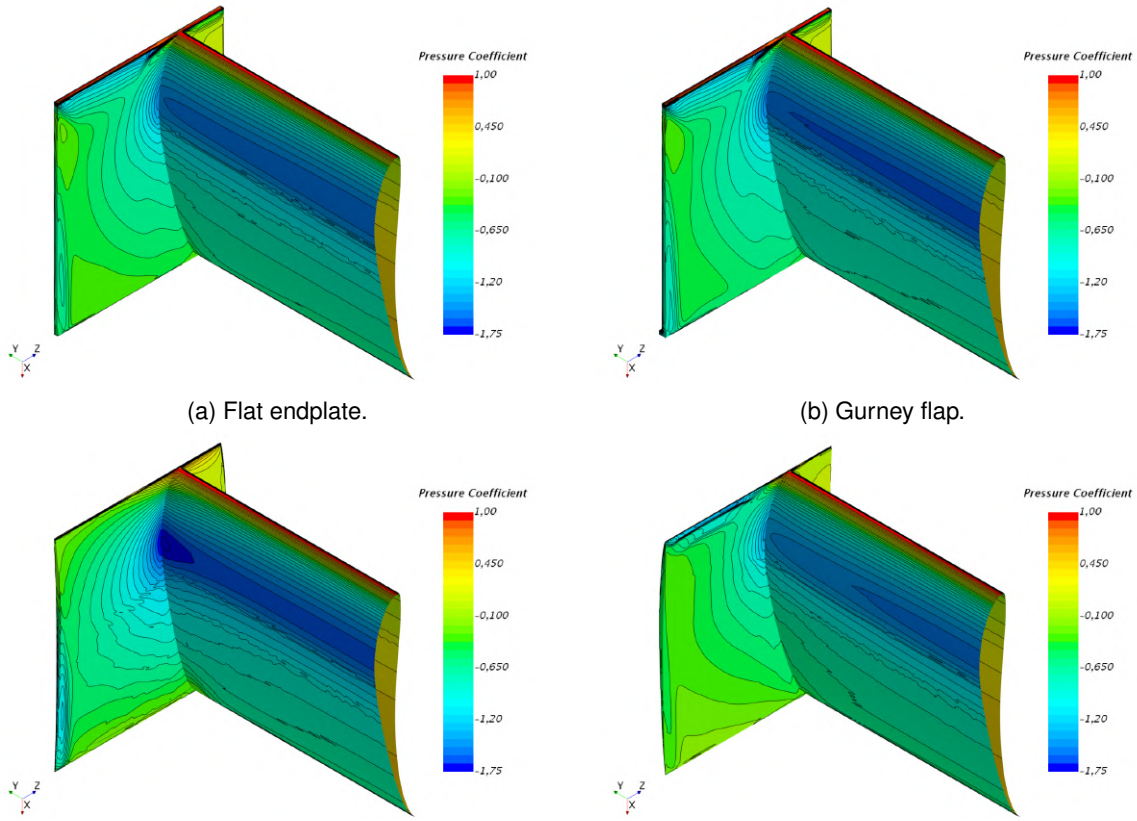

(a) Flat endplate.

(b) Gurney flap.

(c) NACA2402.

(d) Inverted NACA2402.

Figure 4.7: Pressure coefficient on the low-pressure surfaces of both the main plane and the endplate.

the top vortex and weakening the lower one.

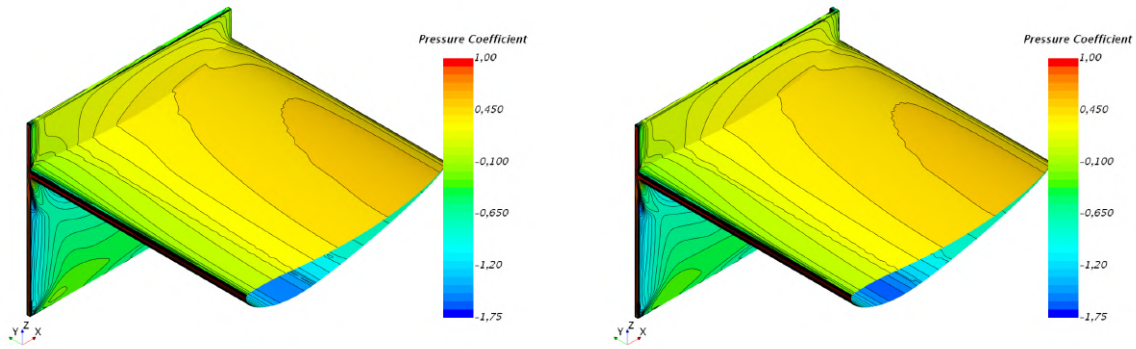

(a) Flat endplate.

(b) Gurney flap.

(c) NACA2402.

(d) Inverted NACA2402.

Figure 4.8: Pressure coefficient contour on the pressure side of the wing.

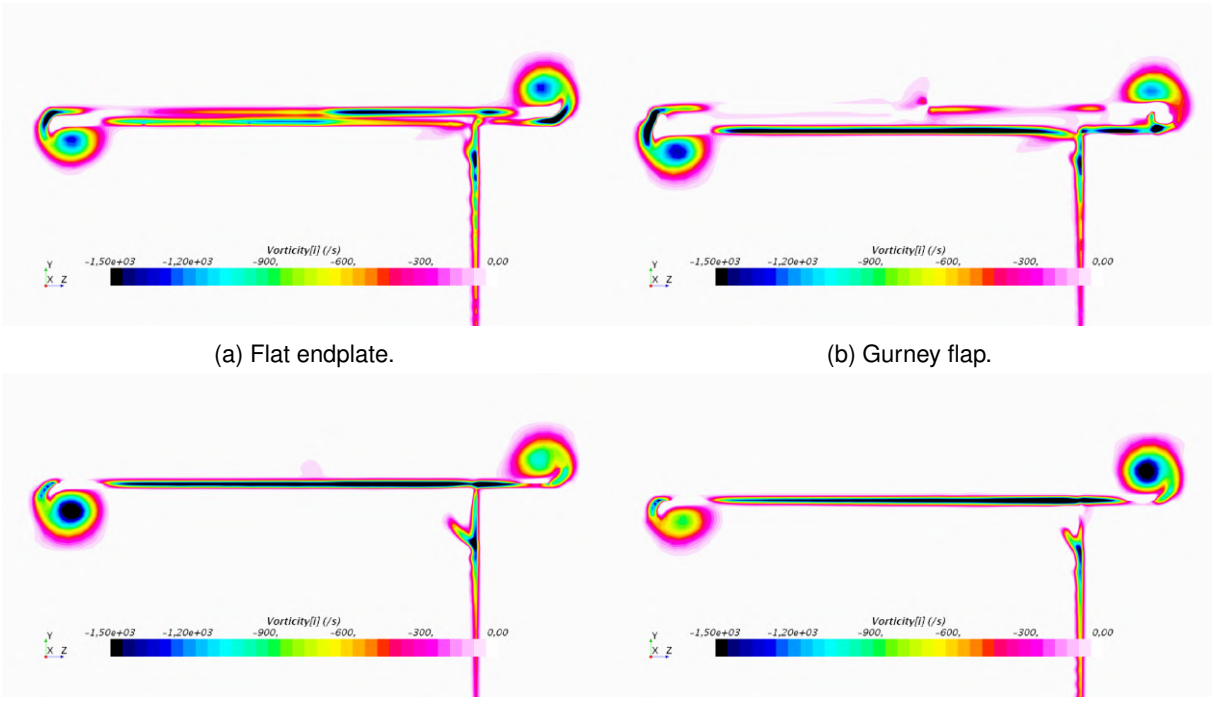

(a) Flat endplate.

(b) Gurney flap.

(c) NACA2402.

(d) Inverted NACA2402.

Figure 4.9: Vorticity in the i direction at the trailing edge plane, $x = 0.4m$. On the right, the vortex of the pressure side; on the left, the vortex of the suction side.

4.4 Full Wing

The same philosophy was transposed to the full wing. Three geometries were tested: a rectangular flat endplate, a rectangular 2402 endplate, and a 2402 endplate with a cut on the pressure side, mirroring the constant top distance of the best configuration found with a single wing element. The results are presented in Table 4.8.

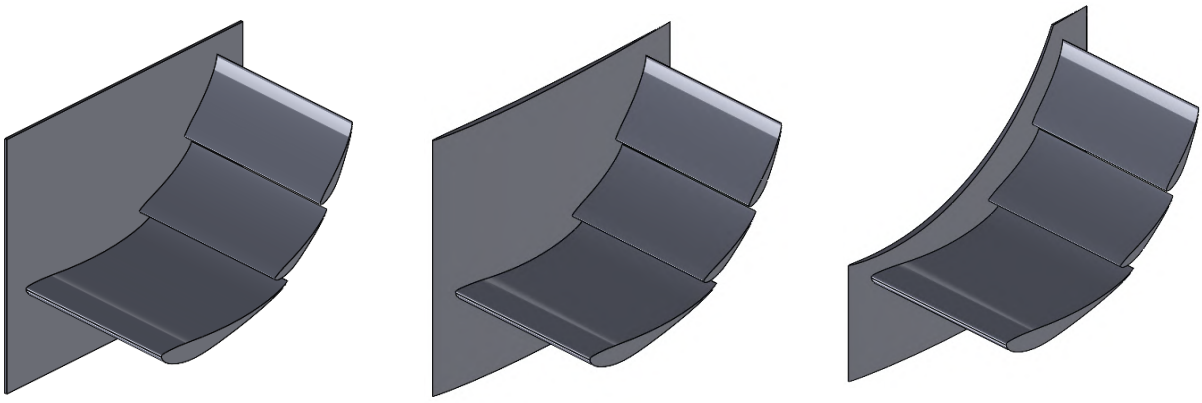

(a) Flat endplate.

(b) NACA2402 Endplate.

(c) NACA2402 with cut on the pressure side.

Figure 4.10: Endplate designs tested on full wing model.

Endplate	Lift [N]	Drag [N]	C_L	C_D	C_L/C_D
Flat	125.505	45.717	2.647	0.964	2.745
NACA2402	128.035	47.275	2.701	0.997	2.708
NACA2402cut	124.504	47.570	2.626	1.003	2.617

Table 4.8: Results of the full wing designs.

When the flaps are added, the difference of the curvature introduced in the endplate decreases. In this case, the endplate with the NACA2402 airfoil yields 2% gain in terms of C_L , but a 3.4% increase in C_D , decreasing the overall efficiency of the wing by 1.3%, in contrast with what was seen previously. The design with the cut on the pressure side has a lower C_L by 0.8% and larger C_D by 4%, giving a 4.6% decrease in the C_L/C_D ratio.

The tip vortexes are shown in Figure 4.11. It can be seen that the added curvature to the endplate strengthens both the lower side vortex and the vortex on the top of the wing. This justifies the increase in drag. On the endplate with the cut, the vortex of the pressure side has already burst, since it forms near the main element, rolls near the edge of the cut, and eventually bursts before reaching the trailing edge of the endplate (Figure 4.12).

The pressure distribution also changes, especially on the low-pressure surfaces (Figure 4.13). The effect of the curvature here is the same as in the single element wing. The added vorticity of the endplate influences the airflow of the main element and the flaps, reducing the pressure, thus increasing the C_L . The pressure on the high-pressure surfaces remains practically unaltered (Figure 4.14).

One of the reasons hypothesized for the reduced effect of the curvature of the endplate in the multi-element wing is that the airflow leaves the wing at an angle when compared to the free stream (Fig-

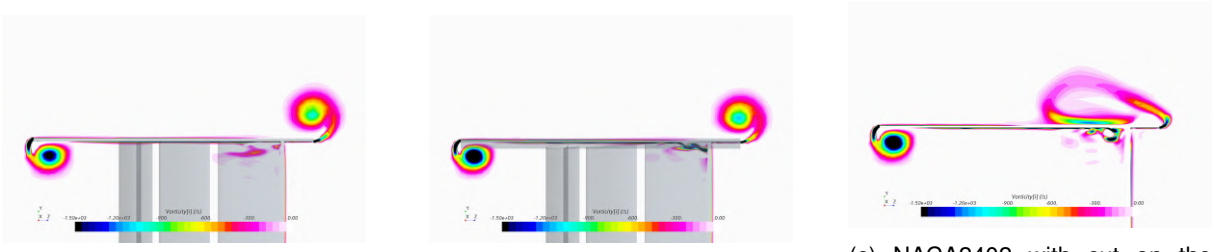

(a) Flat endplate.

(b) NACA2402 Endplate

(c) NACA2402 with cut on the pressure side.

Figure 4.11: Vorticity in i direction at the $x = 0.6m$ plane. On the right side, the pressure side vortex; on the left side, the low-pressure side vortex.

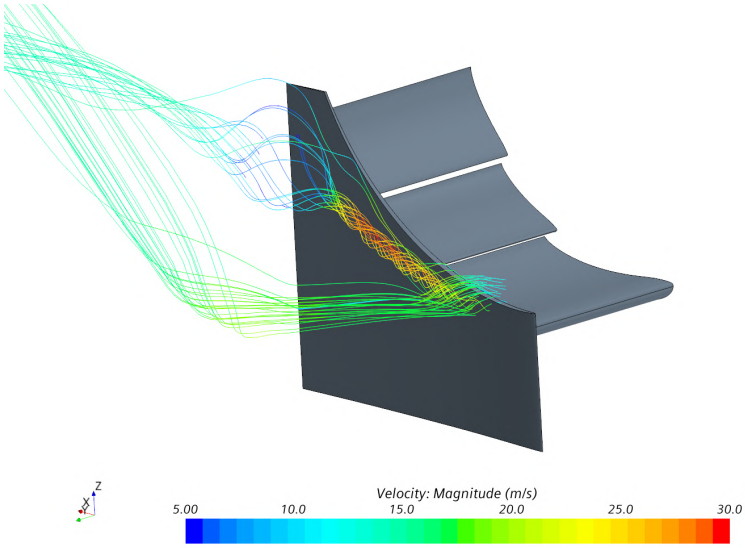

Figure 4.12: Vortex on the endplate with the cut. It bursts before reaching the trailing edge of the endplate.

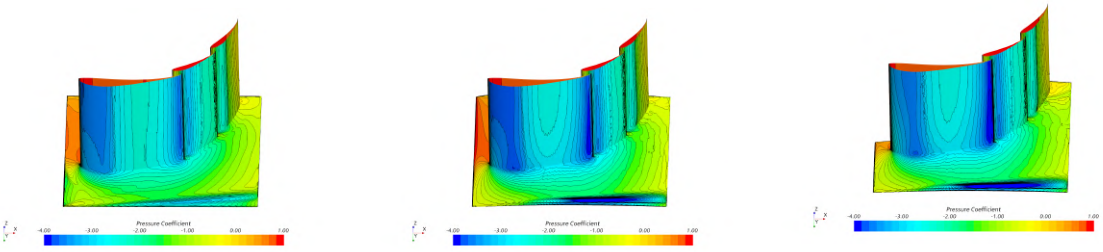

(a) Flat endplate.

(b) NACA2402 Endplate

(c) NACA2402 with cut on the pressure side.

Figure 4.13: Cp on wing.

ure 4.15). This means that we have effectively two wings working on different planes whose vortexes, due to their different core orientation, won't counteract each other in the same way that we saw with the single element wing. More study is required to understand this interaction and how to harness the effect of the curved endplate on the performance of a multi-element wing.

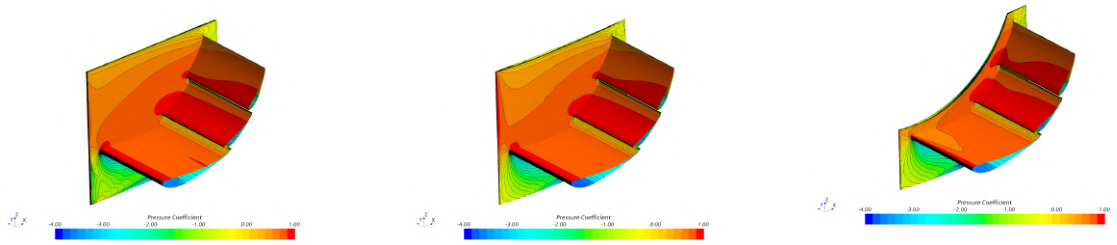

(a) Flat endplate.

(b) NACA2402 Endplate

(c) NACA2402 with cut on the pressure side.

Figure 4.14: Cp on wing.

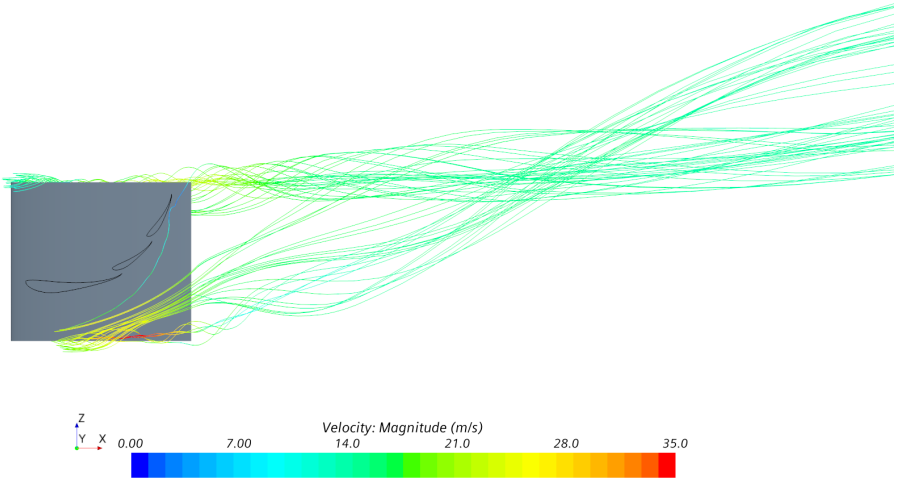

Figure 4.15: Due to the flaps, the airflow leaves the wing at an angle when compared with the top vortex of the endplate tip.

4.5 Yaw Simulations

Another set of simulations was done to understand how the change in endplate design affected the airflow over the wing in a cornering condition. A yaw angle was then introduced in the wing geometry, meaning that now the main wing has a side angle and that the endplates have an angle of attack (Figure 4.16), with each endplate having a high-pressure surface and a low-pressure surface.

The single plane wing model was used once again and since the symmetry of the wing is now lost a full domain had to be used. The mesh parameters however remained the same. The values of the tested angles were 4° and 8° (based on documentation from FST09e Lisboa), since they cover almost the entire range of cornering angles in a Formula Student event. The results are given in Table 4.9.

The endplate with the NACA2402 airfoil has higher C_L and lower C_D values for all the angles tested. The skin friction coefficient of the low-pressure endplate surfaces for the NACA2402 and flat endplates at 4° and 8° is shown in Figures 4.17 and 4.18. The difference in C_f is most noticeable in the low pressure endplate surface near the low-pressure surface of the main element for both $\beta = 4°$ and $\beta = 8°$, where a larger area of separated flow seems to appear near the leading edge of the flat endplate when compared with the leading edge of the NACA2402 endplate.

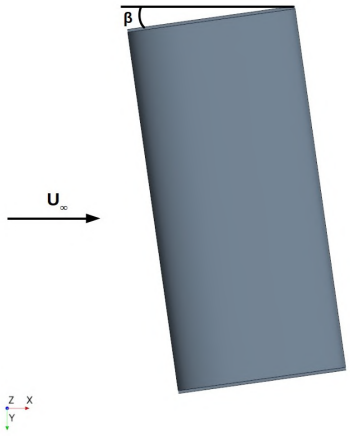

Figure 4.16: Rotation of the wing to introduce the yaw angle.

Endplate	Yaw [°]	L [N]	D [N]	C_L	C_D	C_L/C_D
Flat	0	27.826	3.548	1.174	0.150	7.842
	4	54.896	7.335	1.158	0.155	7.484
	8	54.080	8.012	1.141	0.169	6.750
2402	0	28.981	3.348	1.223	0.141	8.657
	4	57.455	6.888	1.212	0.145	8.342
	8	56.987	7.718	1.202	0.163	7.384

Table 4.9: Values from the yaw angle simulations. The values of the 0° simulations are from the previous section with the half model.

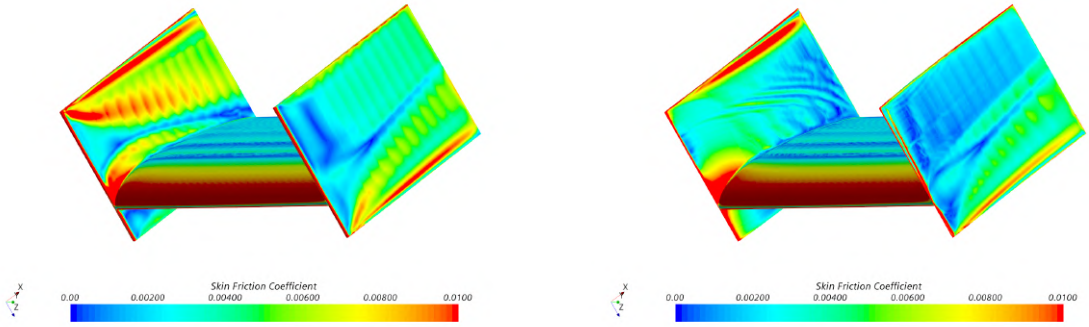

(a) Flat endplate.

(b) NACA2402 endplate.

Figure 4.17: Skin friction coefficient for $\beta = 4°$.

An isosurface of the vorticity magnitude function was created at $\Omega = 1000\ 1/s$ for the entire fluid region. It can be used to see where the vortices are, as well as separation affected zones of the wing. The isosurfaces of the low-pressure side of the endplates facing the wing main plane for $\beta = 4°$ and $\beta = 8°$ are displayed in Figures 4.19 and 4.20. It can be seen that the separation on the flat endplate is indeed bigger than that of the NACA2402 endplate. This can be attributed to the curvature of the airfoil that delays the separation, which does not happen with the flat plate. Furthermore the air of the separated region flows into the tip vortex in the flat endplate case. The separation zone increases with the yaw angle, as a result of the pressure gradient increase.

The different separation patterns observed justify the values in Table 4.9 and the fact that the curved

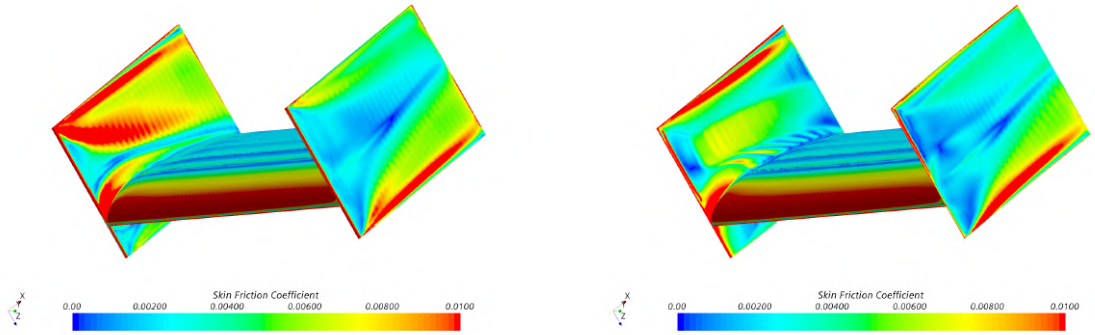

(a) Flat endplate. (b) NACA2402 endplate.

Figure 4.18: Skin friction coefficient for $\beta = 8°$.

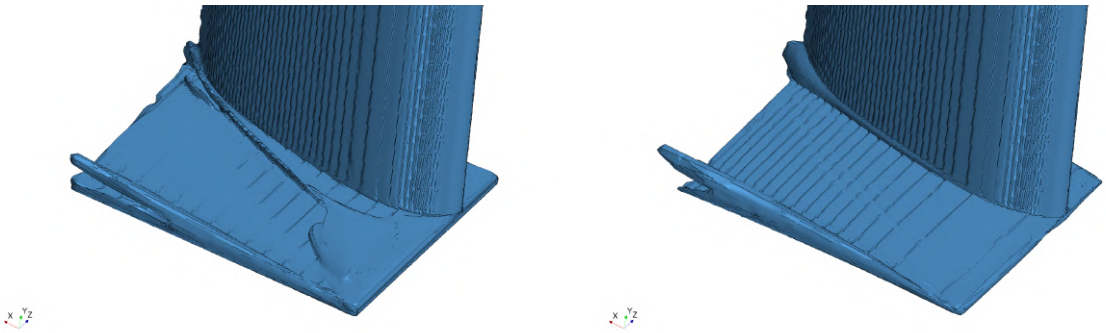

(a) Flat endplate. (b) NACA2402 endplate.

Figure 4.19: Isosurface of $\Omega = 1000\ 1/s$ with $\beta = 4°$.

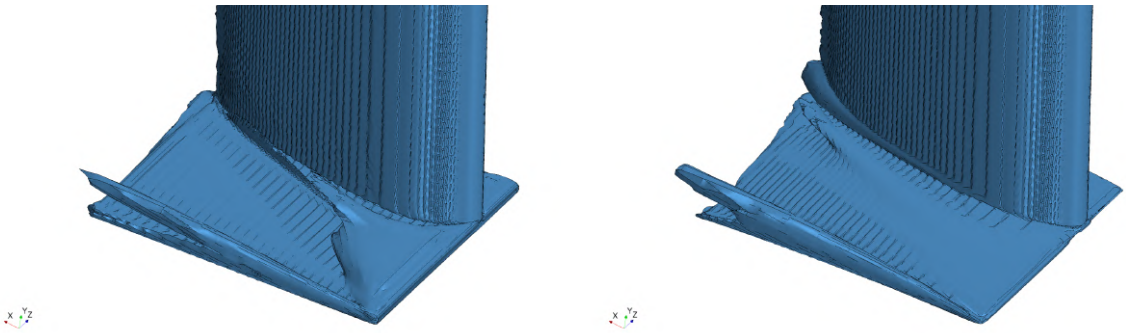

(a) Flat endplate. (b) NACA2402 endplate.

Figure 4.20: Isosurface of $\Omega = 1000\ 1/s$ with $\beta = 8°$.

endplate maintains a superiority in terms of lift and drag coefficient for the two angles simulated.

Chapter 5

Experimental Tests

After the simulation phase, a scale model was constructed so that wind tunnel tests could be carried out to confirm the trends observed in the simulations. At IST there are three wind tunnels available for testing: The Low-Speed Wind Tunnel (LSWT) (described in [37]); the wind tunnel at the Fluids Laboratory, also a low speed wind tunnel; and the wind tunnel of the Aerospace Laboratory. The experimental tests were conducted at the latter two for different Reynolds numbers.

5.1 Wind Tunnel Testing Considerations

For two flows to be dynamically similar, they have to possess the same Mach and Reynolds numbers, which is generally hard to achieve. In the case of low-speed wind tunnels – $Ma < 0.3$ –, the Reynolds number is the primary similarity parameter of interest, since the compressibility effects can be neglected. In such low speed flows, since their characterisation is only a function of L and V, the forces on a body will be the same for any combination of L and V that yields that particular Reynolds number [38].

Due to the difficulty in achieving Reynolds number similarity, namely lower Reynolds numbers than those of actual operations $Re_{model} < Re_{full-scale}$, discrepancies arise in the data gathered in wind tunnel testing: the scale effects. Usually there are also geometric differences in the testing model when compared with the full-scale objects. When the full-scale objects have small items, they are mostly discarded in the scale models even if they could be accurately replicated, because the Reynolds effects would be too great. This inevitably leads to a distortion of the estimation of the variables of interest [38].

The tests were first ran at the FLuids Laboratory, which is a low-Reynolds number tunnel of the open type, with a test section measuring circa $600 \times 400mm$ (height and width, respectively) and a maximum achievable speed of $20m/s$. The tunnel is equipped with a 6DOF balance (specifications in section B.1).

5.2 Wing Model

The tunnel specifications present the problems described above, making it impossible to establish Reynolds similarity in these experiments. To reduce the scale effects, the model has to be as big as

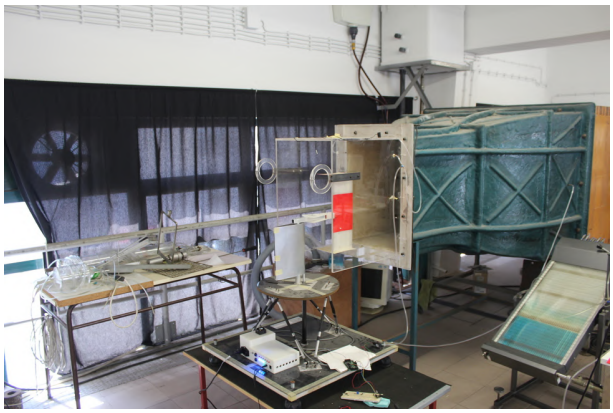

Figure 5.1: Low Reynolds Wind Tunnel at the Fluids Laboratory.

possible. Given that the working section is a rectangle whose height is larger than its width, the wing had to be mounted in a rotated position of 90 degrees over its x-axis. This gives a maximum scale of 40%. At that scale the wing model has a span of $400mm$ and a chord of $160mm$, for a planform area of $A = 0.064m^2$. The maximum possible Reynolds number is then $Re = 2.17 \times 10^5 < Re_{CFD}$.

The construction of the model had to take several factors into account. The wing itself made use of 3D printing. Since the printing base measured $200 \times 200mm$, the wing had to be printed in several parts (Figure 5.2). On top of that, testing the wing with a yaw angle required that an additional part was printed that allowed the wing to be rotated along its z-axis. Therefore, the wing model assembly has the following characteristics:

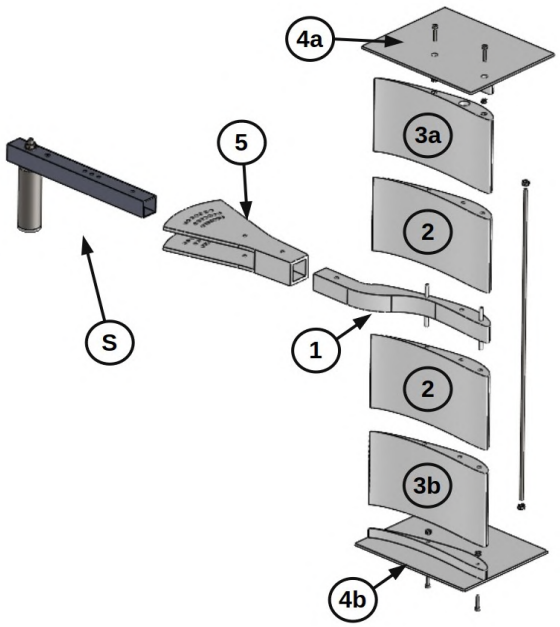

Figure 5.2: Wing model assembly, exploded view.

- Part **1** is in the symmetry plane of the wing model. It has an extension that connects it to **Part 5**;
- Part **2** was printed twice; they constitute the root half-span of the wing;

- Parts **3a** and **3b** are symmetrical. Two M3 nuts were glued to each of parts **3a** and **3b** so that the endplates could be fastened to them;
- Parts **1**, **2**, **3a** and **3b** are all connected together with a M4 threaded steel rod. Pins were added in each part's interface to stop the parts from rotating about the steel rod;
- Parts **4a** and **4b** are the endplates. They are connected to parts **3a** and **3b** with two M3 bolts. Each one has the final tip of the wing's main plane for three reasons:
  - First, to hide the bolts needed to connect each of the endplates to the parts **3a** and **3b**, reducing their drag penalty;
  - Second, to guarantee that the span of the wing would be the same regardless of the endplate, which would have been more difficult to do especially in the case of the endplate with curvature;
  - Third, the endplates with curvature would require a different ending to parts **3a** and **3b** in comparison to the flat ones (see Figure 5.3). The tip integrated in the endplate solves that problem and reduces the overall time and material needed for printing.
- Part **5** is the yaw angle adapter. It is fastened to part **1** with a M4 bolt. It has three "rows" of concentric roles which allow the testing of angles in a range of 0 to 20° in increments of 1° ;
- The sub-assembly **S** forms the structure that is fastened to the threaded rod of the balance. It consists of a $20 \times 20mm$ aluminum tube and a $25 \times 2mm$ cylindrical steel tube[1] that acts as extension of the balance's fixation point.

(a) Flat endplate.

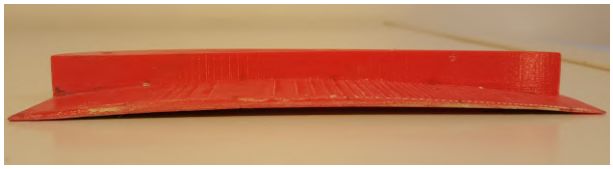

(b) Endplate with the 2402 airfoil.

Figure 5.3: The two endplate designs selected for testing. The extremity of the wing saved time and material during the printing phase.

The printing quality was good overall except for the endplates with curvature. The pressure side on those had extreme roughness because of the support material added during the printing process. To address it, the surfaces of the endplates with curvature were sanded and putty was added, a process repeated until the surface had a proper finish (Figure 5.4).

[1] This extension was added only after the first test runs when it was noticed that the lower endplate was too close to the tunnel's lower wall, causing larger vibrations than on the other endplate

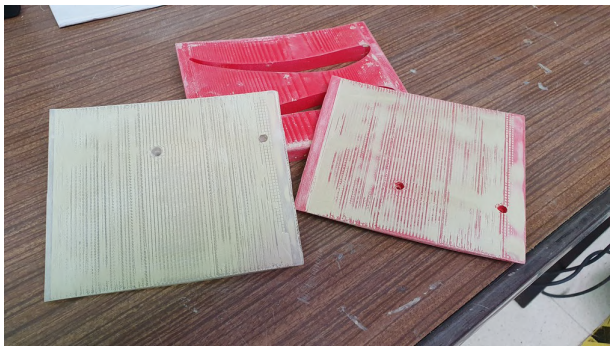

Figure 5.4: The endplates with curvature required sanding and putty before testing.

After this process the wing model was assembled on the tunnel to assess if it was ready for testing (Figure 5.5).

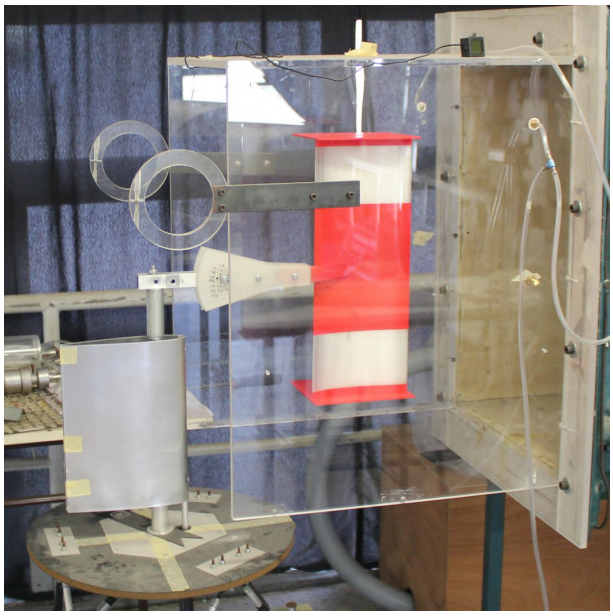

Figure 5.5: Wing model mounted on the balance at the Fluids Laboratory.

5.3 Experimental Procedure

The purpose of the tests was to confirm the trends observed in the CFD simulations. In order to accomplish that, it was decided that three different configurations would be tested:

- A reference setup without any endplates;
- The flat endplates;
- The endplates with curvature.

For each setup, twenty data acquisitions were performed, each during 20s at the DAQ 150Hz acquisition frequency.

Initially, data was collected for two different airflow velocities: 7.5 and 10 m/s. It was noted that the lower extremity of the wing was too close to the flow adjacent to the lower wall of the tunnel, having a clear effect on the stability of the wing. Therefore, an extension was added to the support so that the wing would be in a more centered position relative to the working section. The fastener was also changed, as well as the position of the wing. The moment generated by the downforce was then in the fastening direction, stopping the wing from rotating from the initial position for higher velocities/loads. This way, the maximum velocity measured increased from the 10m/s to 15m/s. The maximum velocity of the tunnel still could not be reached because from that velocity the vibrations of the wing model were strong enough to threaten its structural integrity, as well as that of the balance.

Woolen threads were added to the surfaces of the wing so that the airflow behaviour over the wing could be visualized and compared with the CFD simulations. For the latter experiments sand-paper strips were glued to the model's surfaces. These act as a trip strip, fixing the location of transition from laminar to turbulent flow [38]. This is done in an attempt to emulate the working condition Reynolds flow and minimize the scale effects. A consequence of their use will be the elimination of any separation bubbles [39]. Nonetheless, despite the possible differences in the airflow with the sand-paper, the objective of its addition was to confirm the trend observed in the numerical simulations. The woolen threads and sand paper strips are shown in Figure 5.6.

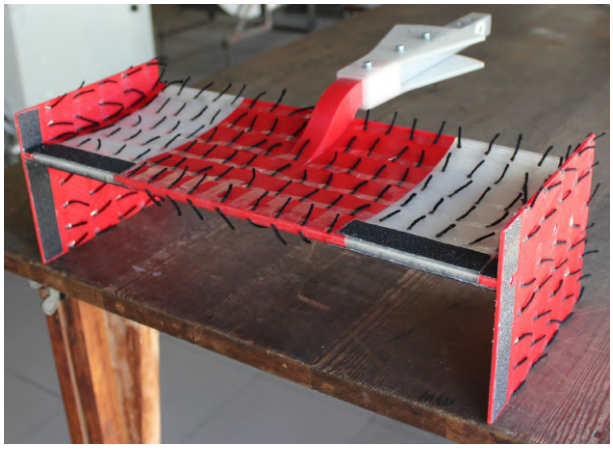

Figure 5.6: Wing model with woolen threads and sand paper as used in the last test run for the yaw angles.

5.4 Test Results

5.4.1 Clean Wing

The first run was performed for the three configurations described above at two airflow velocities, $\approx 7.5m/s$ and $\approx 15m/s$. The wing was clean, in that there were no woolen threads or sand paper strips. The results are presented in Table 5.1.

For the lower Re, the differences are significant. The 2402 endplate has less lift (11.1%), more drag (35.2%) for a smaller efficiency C_L/C_D (34.3%). When the Re was increased, the C_L increased for the

Endplate	Velocity [m/s]	Re	Lift [N]	Drag [N]	C_L	C_D	C_L/C_D
No-Endplates	7.823	8.50×10^4	0.44521	0.04215	0.186	0.018	10.563
	14.781	1.61×10^5	1.64069	0.11867	0.192	0.014	13.825
Flat	7.851	8.53×10^4	0.58894	0.04049	0.244	0.017	14.545
	14.800	1.61×10^5	2.22239	0.12462	0.259	0.015	17.833
2402	7.872	8.56×10^4	0.52618	0.05504	0.217	0.023	9.559
	14.833	1.61×10^5	2.13202	0.13637	0.247	0.016	15.635

Table 5.1: Data for the first experiment.

Re	Endplate	C_L	$\Delta[\%]$	C_D	$\Delta[\%]$	C_L/C_D	$\Delta[\%]$
8.53×10^4	Flat	0.244	—	0.017	—	14.545	—
	2402	0.217	-11.1	0.023	+35.2	9.559	-34.3
1.61×10^5	Flat	0.259	—	0.015	—	17.833	—
	2402	0.247	-4.5	0.016	+8.9	15.635	-12.3

Table 5.2: Clean wing results' comparison.

two endplates and the C_D decreased, resulting in higher C_L/C_D ratios. The differences between the two endplates at the higher Re were much smaller for each of the three coefficients. In this case, the 2402 endplate had a 4.5% smaller C_L , a 8.9% increase in C_D and an efficiency 12.3% below the flat endplate. This second set of values points to a significant influence of small Reynolds numbers effects at the lowest flow speed tested.

Indeed, the latter addition of the woolen threads showed the existence of significant separation on the low-pressure surfaces of the 2402 endplate and main wing (Figure 5.7), something which was not present on the flat endplate. The separation could not be as easily observed at the lower Re, but looking at the forces' values one can assume that not only is it there, but it also spans a larger region. The separation justifies the values obtained for the 2402 endplate, contrary to what was expected based on the CFD results.

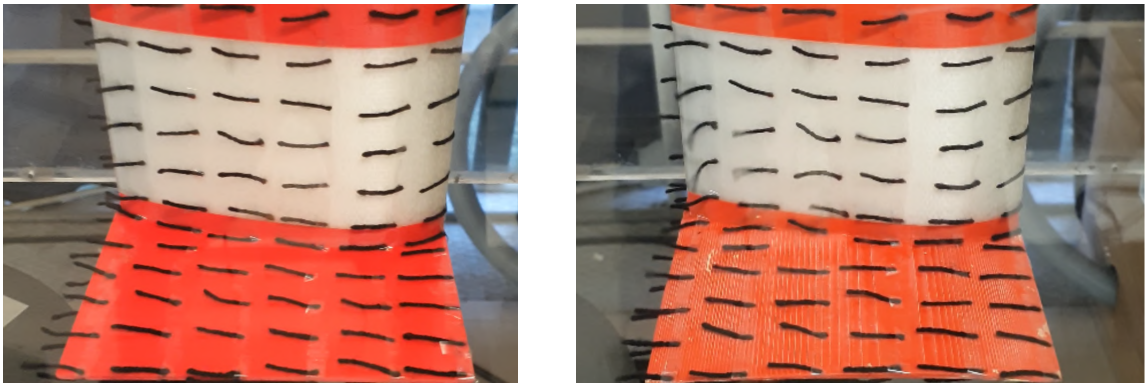

(a) Flat endplate.

(b) 2402 endplate.

Figure 5.7: Woolen threads on the underside of the wing showing separation on the 2402 configuration at $Re = 1.61 \times 10^5$.

5.4.2 Sand Paper

The results of the clean wing suggested that the different trend of the experimental results was a consequence of the scale effects. As such, sand paper strips were added to the main wing. These were placed on the leading edge of the wing (both pressure and suction sides) near the wing tip and on all the endplates' surfaces. the. In this test the reference configuration without endplates was not tested for time-saving reasons. The data is shown in Table 5.3. In Table 5.4 a comparison between the values of the two configurations is given.

Endplate	Velocity [m/s]	Re	Lift [N]	Drag [N]	C_L	C_D	C_L/C_D
Flat Plate	8.040	8.74×10^4	0.47473	0.05209	0.187	0.021	9.114
	14.948	1.63×10^5	1.85127	0.14411	0.211	0.016	12.846
NACA2402	8.001	8.70×10^4	0.45046	0.06109	0.180	0.024	7.374
	14.989	1.63×10^5	1.75520	0.14362	0.199	0.016	12.221

Table 5.3: Sand paper on all the models' surfaces.

Re	Endplate	C_L	$\Delta[\%]$	C_D	$\Delta[\%]$	C_L/C_D	$\Delta[\%]$
8.70×10^4	Flat	0.187	—	0.021	—	9.114	—
	2402	0.180	-4.2	0.024	+18.4	7.374	-19.1
1.63×10^5	Flat	0.211	—	0.016	—	12.846	—
	2402	0.199	-5.7	0.016	-0.9	12.221	-4.9

Table 5.4: Wind Tunnel results, sand paper and woolen threads on wing surfaces.

The sand paper has a considerable influence on the results. With it, for each of the Reynolds numbers tested, the difference between the two endplates is smaller, particularly for the lower Reynolds flow, where the differences regarding the three coefficients C_L , C_D and C_L/C_D are now, respectively -4.2% (>-11.1%), +18.4% (<+35.2%) and -19.1% (>-34.3%) At $Re = 1.63 \times 10^5$, the C_L is smaller by 5.7%, but the C_D of the 2402 endplate is atually 0.9% smaller than that of the flat endplate, the first occurrence of a value in agreement with the results of the CFD simulations. Combined, the 2402 endplate has an efficiency 4.9% below that of the flat endplate. This is further evidence that the low Reynolds number flows are not identical to the simulated conditions and that they have a significant influence on the obtained results.

With the sand strip, there did not seem to exist separation as before on the 2402 endplate, which would explain the close C_D values between the two geometries. There seemed to be more perturbations on the flow with the 2402 endplate, though (Figure 5.8), which may be related to the dimensions of the sand paper (width and height) that may cause small separation regions aft of it.

5.4.3 Yaw Angles

Two yaw-angles (β) were tested for the the two principal configurations – flat plates and 2402 endplates –, whose purpose is to simulate the wing behavior in a cornering condition. The angles chosen were 4 and 8 degrees, based on documentation from FST Lisboa. These two values cover the entire

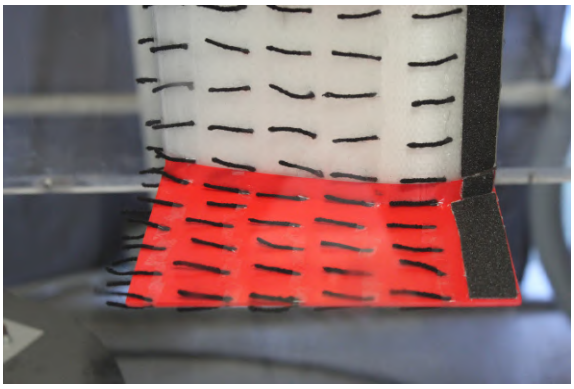

(a) Flat endplate.

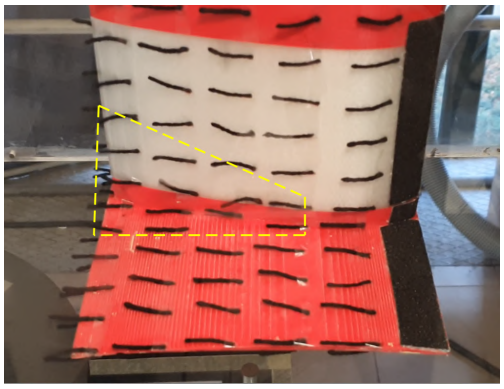

(b) 2402 endplate.

Figure 5.8: Woolen threads on the underside of the wing featuring the sand paper strip at $Re = 1.61 \times 10^5$. This time separation was not evident, but the flow with the 2402 configuration had more perturbations than with the flat endplate, highlighted by the yellow dashed line.

range of angles in a cornering situation at a Formula Student Event. The wing had the sand paper on it owing to the results obtained beforehand. The results are outlined in Table 5.5 and the differences between the two endplates is given in Table 5.6.

Endplate	$\beta[^\circ]$	Velocity [m/s]	Re	Lift [N]	Drag [N]	C_L	C_D	C_L/C_D
Flat	0	8.040	8.74×10^4	0.47473	0.05209	0.187	0.021	9.114
		14.948	1.63×10^5	1.85127	0.14411	0.211	0.016	12.846
	4	7.726	8.40×10^4	0.46504	0.05801	0.199	0.025	8.017
		15.127	1.64×10^5	1.83727	0.14996	0.205	0.017	12.252
	8	7.927	8.62×10^4	0.47483	0.05837	0.193	0.024	8.135
		14.765	1.61×10^5	1.69659	0.17045	0.199	0.020	9.953
2402	0	8.001	8.70×10^4	0.45046	0.06109	0.180	0.024	7.374
		14.989	1.63×10^5	1.75520	0.14362	0.199	0.016	12.221
	4	8.022	8.72×10^4	0.46632	0.06597	0.185	0.026	7.069
		14.987	1.63×10^5	1.69864	0.15906	0.193	0.018	10.679
	8	7.990	8.69×10^4	0.45311	0.07025	0.181	0.028	6.450
		14.985	1.63×10^5	1.64419	0.17754	0.187	0.020	9.261

Table 5.5: Values measured for the two yaw angles chosen.

Once again there is a significant difference between the two Reynolds numbers tested. The 2402 endplate again has generally smaller C_L and higher C_D values than the flat one. There are also noteworthy differences across the 3 angles tested. While the difference of the C_L values remain relatively constant for the three angles at each Reynolds number, that is not the case with the C_D values. For $Re = 8.70 \times 10^4$ and $\beta = 4^\circ$, the 2402 endplate only has 5.5% more drag than the flat endplate (the smallest difference of the three C_D coefficients), whereas for $Re = 1.63 \times 10^5$ and $\beta = 4^\circ$ the C_D of the 2402 exhibits the largest difference to the flat endplate at 8.1%. These differences in the C_D values reflect themselves on the efficiency of each of the combinations of endplate and angle, but all below those of the flat endplates. These varying differences hint at a larger importance of the lower Reynolds number at which these tests were conducted.

With the help of the woolen threads in the runs with the yaw angles, shown in Figures 5.9 and 5.10

Re	$\beta[^\circ]$	Difference to the flat plate Δ [%]		
		C_L	C_D	C_L/C_D
8.70×10^4	0	-4.2	18.4	-19.1
	4	-7.0	5.5	-11.8
	8	-6.1	18.4	-20.7
1.63×10^5	0	-5.7	-0.9	-4.9
	4	-5.8	8.1	-12.8
	8	-5.9	1.1	-7.0

Table 5.6: Differences of the 2402 endplate to the flat endplate for the three β angles tested.

for the highest Reynolds number tested $Re = 1.63 \times 10^5$, the differences in the airflow could be seen for the two yaw angles and the two endplates. For every angle and endplate there was separation on its outer and inner surfaces, differing in region size and intensity. For $\beta = 4^\circ$, the outer surface of both endplates had separation. The flat endplate's separation seemed to extend further aft of the leading edge, whereas that of the 2402 endplate seemed stronger but shorter in length. In the inner surface both endplates displayed separation but only at the intersection between the main plane and endplate near the trailing edge. For $\beta = 8^\circ$, the separation areas were larger in all the considered surfaces. Both the outer surfaces of the flat and 2402 endplates had massive separation, but this time not only was that of the 2402 stronger, it was also bigger in size than the one of the flat endplate. On the inner surface, on the one hand the flat endplate had separation near its leading edge, which seemingly reattached, not reaching the trailing edge of the wing; on the other hand, the separation of the 2402 endplate on its inner surface was large, extending inward into the main plane, and strong, probably as a consequence of a stronger pressure gradient imposed by the angle, which effectively put the endplate at an angle of attack $\alpha = 8^\circ$.

5.5 Discussion

The low Reynolds number flows that were used in the experimental tests almost surely had a strong influence in the trends obtained. To better understand how it could have played a role in the results, two approaches have been taken with the help of CFD simulations:

- Simulating the model at the Reynolds numbers seen in the wind tunnel;
- Recreating the wind tunnel conditions in CFD to see the influence of the tunnel's walls.

5.5.1 Low-Reynolds Simulations

These simulations used the exact same geometries of section 4.2. Using the Reynolds number equation, to achieve similar Re of the wind tunnel, the following velocities $V = 3.1m/s$ and $V = 6.2m/s$ were tested. The forces, coefficients and differences are in Table 5.7.

There are some takeaways from these simulations:

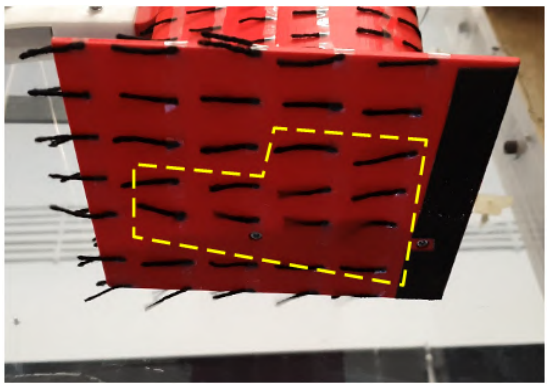

(a) Flat endplate, outer surface.

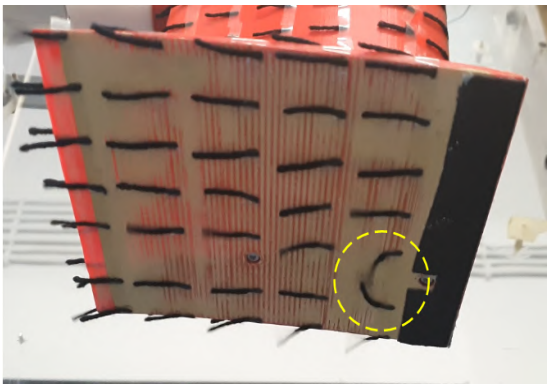

(b) 2402 endplate, outer surface.

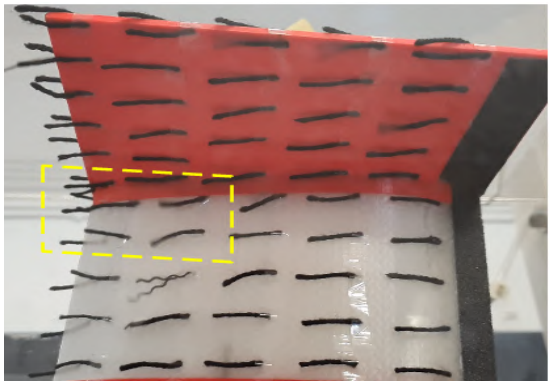

(c) Flat endplate.

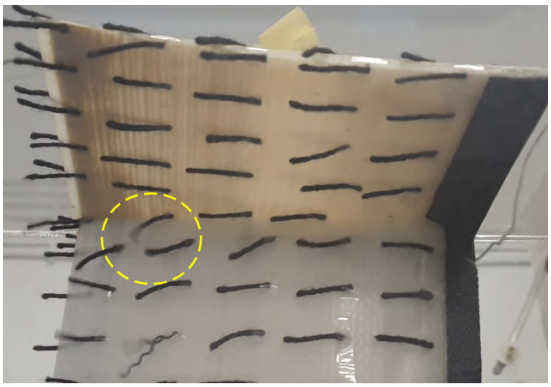

(d) 2402 endplate, inner surface.

Figure 5.9: Woolen threads on the underside of the wing for $\beta = 4°$ and $Re = 1.63 \times 10^5$.

Re	Endplate	Lift [N]	Drag [N]	C_L	Δ [%]	C_D	Δ [%]	C_L/C_D	Δ [%]
8.42×10^4	Flat	1.00294	0.13213	0.991	—	0.131	—	7.591	—
	2402	1.03150	0.12556	1.019	+2.8	0.124	-5.0	8.215	+8.2
1.68×10^5	Flat	4.46353	0.57458	1.102	—	0.142	—	7.768	—
	2402	4.61773	0.54178	1.140	+3.5	0.134	-5.7	8.523	+9.7

Table 5.7: Results of the simulations of the two experimental Reynolds numbers.

- As with the experimental results, the increase in Reynolds number results in an increase in C_L and a decrease in C_D , with an increase in C_L/C_D of both the configurations;
- The absolute values of the these simulations are much larger than those of the experiments, with $C_{L_{Low-RE-CFD}} \approx 5C_{L_{WT}}$, $C_{D_{Low-RE-CFD}} \approx 10C_{D_{WT}}$, similar to the ratios between the full-scale Reynolds simulations;
- The trend here is the same as the one in the first simulations, and not that of the wind tunnel, hinting at other cause for the difference in trend observed with the two methods;
- On the other hand, the increasing beneficial effect of the 2402 endplate effect on the C_L and C_D of the wing seems to agree with the data from the experimental tests.

The behaviour of the airflow at those Reynolds numbers in the simulations shared some similarities with those of the wind tunnel tests. These are shown in Figures 5.11 and 5.12. There is a larger separation area in the intersection between the main wing and the 2402 airfoil for both Reynolds numbers.

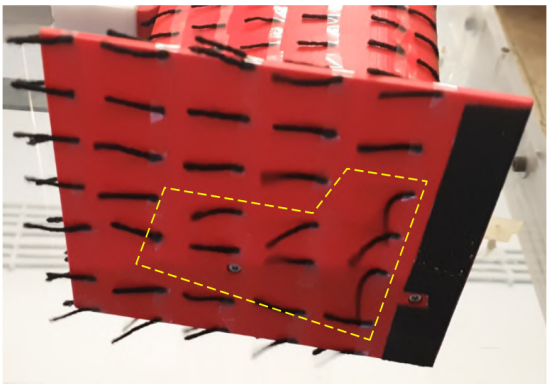

(a) Flat endplate, outer surface.

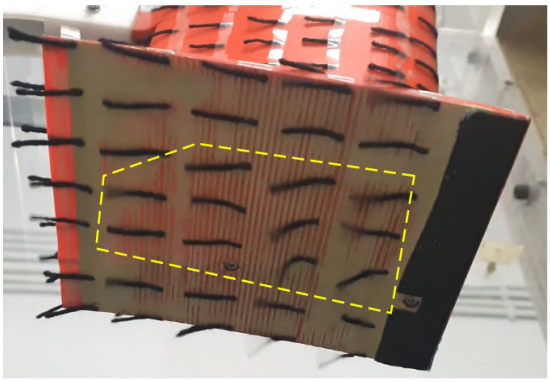

(b) 2402 endplate, outer surface.

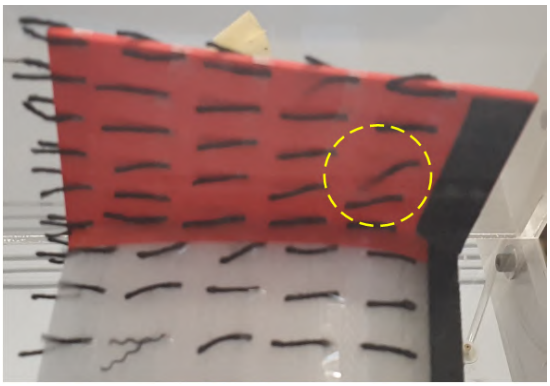

(c) Flat endplate.

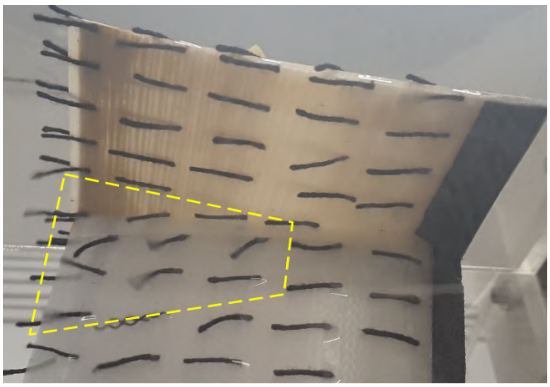

(d) 2402 endplate, inner surface.

Figure 5.10: Woolen threads on the underside of the wing for $\beta = 8°$ and $Re = 1.63 \times 10^5$.

In the case of the flat endplate, there is only a small separation zone in the intersection between the endplate and main wing near the wing's trailing edge. However, the blunt edges of the endplate's front face cause a separation region at the endplate's leading edge that does not exist with the 2402 airfoil and its round leading edge.

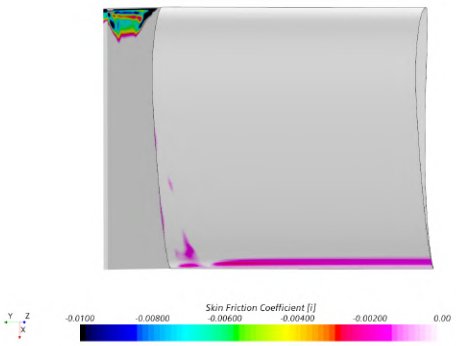

(a) Flat endplate.

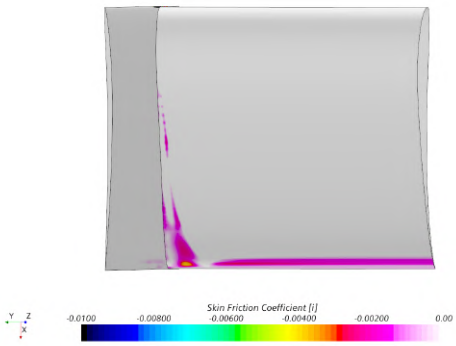

(b) 2402 endplate.

Figure 5.11: Skin friction coefficient on the underside of the wing at $Re = 8.42 \times 10^4$.

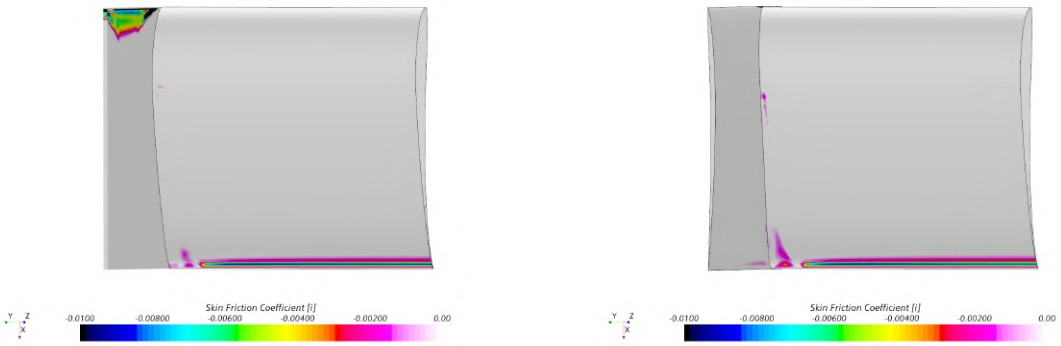

(a) Flat endplate.

(b) 2402 endplate.

Figure 5.12: Skin friction coefficient on the underside of the wing at $Re = 1.68 \times 10^5$.

5.5.2 Simulating the Wind Tunnel Conditions

Pre-processing – Geometry, Mesh and Numerical Setup

The tunnel geometry was recreated and then imported into Star-CCM+. The domain was made consisting of the contraction section of the tunnel, the acrylic walls that make up the working section, and then a rectangular prism aft of the wing constituting the rest of the space where the flow goes into (Figure 5.13). The geometry was made according to measurements taken from the laboratory itself. The contraction is a simple loft from the rectangle of the largest section of the ventilator ($\approx 1300 \times 1010mm$) up to its exit, which corresponds to the same dimensions of the working section ($600 \times 400mm$). Since the working section only has three acrylic walls (the top and side walls), so too does the model; the lower side was included in the rest of the domain.

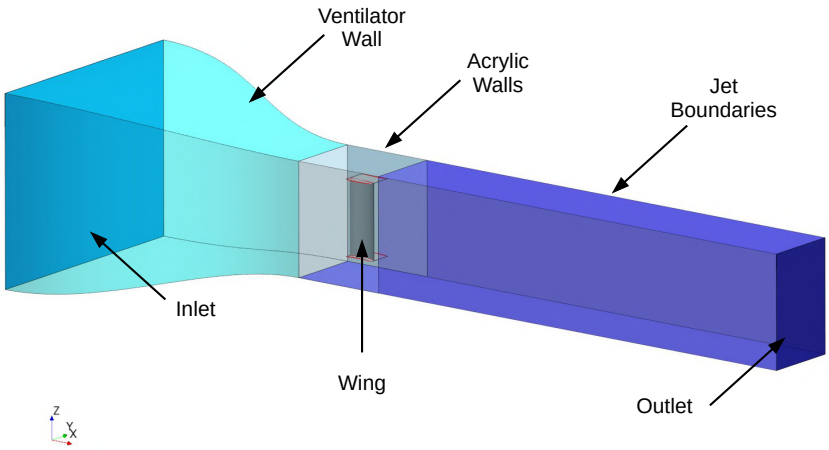

Figure 5.13: Geometry of the wind tunnel replicated in the simulation.

The mesh, that is shown in Figure 5.14, was generated having in mind what was described in Chapter 3. However, since the wing in these simulations is smaller due to the scale factor, the Target Surface Size was changed to $1mm$. To guarantee a y-plus value of $y^+ = 1$ on the wing's surfaces, the initial

prism layer height was set to $h_1 = 0.01mm$ This can be verified in Figure 5.15. Prism layers were also used in the ventilator and acrylic no-slip walls.

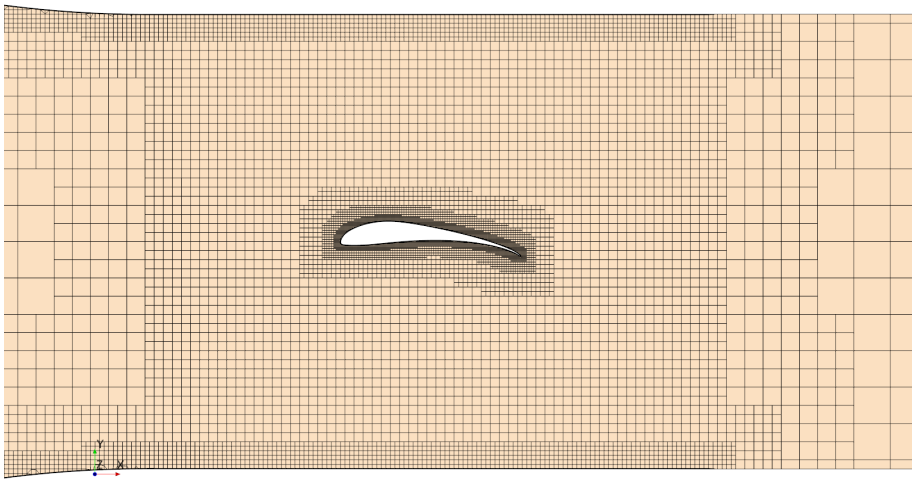

Figure 5.14: Mesh on $z = 0m$ plane.

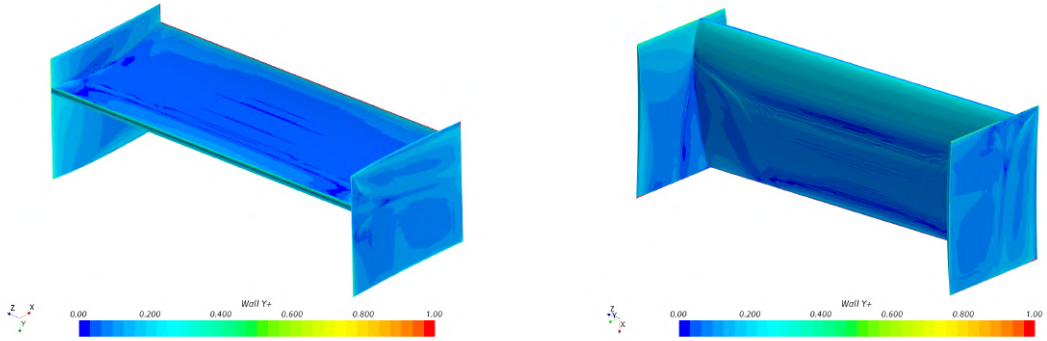

(a) Wing's top surface.

(b) Wing's underside.

Figure 5.15: Distribution of the y^+ values on the wing.

In terms of boundary conditions, the inlet is a velocity inlet; the velocity value was calculated using the velocity measured in the actual experiments as a starting point, which was then introduced in the continuity equation (Equation 5.1). The continuity equation is used just as an approximation, because the no-slip walls of the ventilator and the wing on the exit of the ventilator will impact the flow velocity there. To ascertain if the velocity before the wing was the same as the one in the experiments, the average velocity on the plane at the exit of the ventilator was calculated. This velocity was used in the calculation of the different coefficients. The ventilator walls are no-slip walls, as well as the acrylic walls. The jet walls have a no-slip condition. Due to the assymetry of the boundary conditions, no symmetry condition could be used in these simulations.

$$\dot{m} = \rho_{inlet} A_{inlet} V_{inlet} = \rho_{exit} A_{exit} V_{exit} \quad \Leftrightarrow \quad V_{inlet} = \frac{A_{exit}}{A_{inlet}} V_{exit} \tag{5.1}$$

In this case, $A_{exit}/A_{inlet} = \frac{600\times400}{1300\times1010} \approx 0.183$.

Regarding the physics models, the same ones were used as in the CFD simulations mentioned in Chapters 3 and 4, including the γ-Re_θ model. The simulations were done for the same two Reynolds numbers verified in the laboratory.

Results

Re	Endplate	C_L	$\Delta[\%]$	C_D	$\Delta[\%]$	C_L/C_D	$\Delta[\%]$
8.03×10^4	Flat	1.192	—	0.120	—	9.937	—
	2402	0.957	-19.8	0.124	3.3	7.721	-22.3
1.61×10^5	Flat	1.258	—	0.121	—	10.364	—
	2402	1.151	-8.5	0.117	-3.4	9.817	-5.3

Table 5.8: Results of the Wind-Tunnel simulation.

The results of the simulations are in Table 5.8. There are some things of notice:

1. Once again, the increase in C_L with the higher Reynolds number is consistent with the low Reynolds simulations as well as the data from the wind tunnel experiments. The C_D , however, increases in the flat plates but decreases in the 2402 endplates;

2. Trend-wise, the lift and drag coefficients are respectively lower and higher at the two Reynolds numbers for the 2402 endplates, just like the wind-tunnel tests showed, and unlike the low Reynolds simulations. Just as was seen with those two methods, the difference between the C_L , C_D and C_L/C_D decreases significantly when the Reynolds number was increased;

These two observations point towards the idea that the blockage effect contributes to the inverted tendency observed in the experimental tests, even if the exact geometry of the wind tunnel could not be replicated.

Besides the coefficients, the separation areas observed in the wind-tunnel testing can also be compared with the ones seen in the simulations. To that effect, the skin friction coefficient in the i direction is shown for the Reynolds numbers indicated in Table 5.8 in Figures 5.16 and 5.17. At the lower Reynolds number, there is a massive separation area on each wing-tip of the curved endplate (Figure 5.16b) which is not present in the case of the flat endplate (Figure 5.16a). The presence of the walls near the model influence how the airflow behaves around it, affecting the pressure gradients on the wing's surfaces, originating separation areas that otherwise would not exist on the wing. On the higher Reynolds number, whereas the flat endplate does not have noticeable separation besides the trailing edge area (Figure 5.17a), the curved endplate now just has a large separation zone on one of the wing-tips (Figure 5.17b), the one that is not surrounded by an acrylic wall ($\tau_w = 0Pa$).

The same sort of flow patterns were observed in the wind-tunnel, even if separation outright was hard to identify. These are laid out in Figures 5.18 and 5.19 for the two Reynolds numbers tested, highlighet by the yellow dashed lines. When the flat endplates were mounted on the wing, there was hardly ever any sort of disturbance on the wing's surfaces, either on top or the lower side, just like what

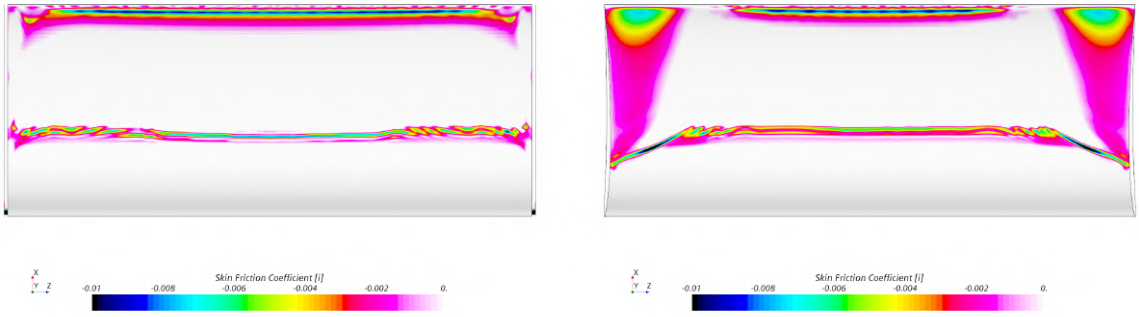

(a) Flat endplate.

(b) NACA2402 endplate.

Figure 5.16: Skin Friction Coefficient [i] for $Re = 8.03 \times 10^4$ on the wing underside.

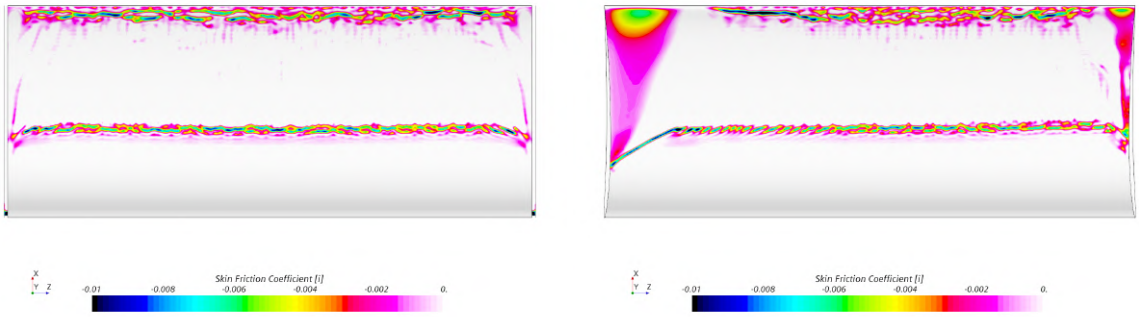

(a) Flat endplate.

(b) NACA2402 endplate.

Figure 5.17: Skin Friction Coefficient [i] for $Re = 1.61 \times 10^5$ on the wing underside.

was seen in the simulations. With the 2402 endplate the airflow seemed to be more chaotic, with the threads oscillating from side to side vigorously but not turning backwards. This happened on both the main plane and endplate's surfaces, on both wing tips and for both the Reynolds numbers tested. The higher Reynolds number tested seemed to have reduced this effect on the wing's surfaces, especially on the inside of the endplate on the bottom. On the top endplate there were still some perturbances, which is opposite to what the simulations showed.

These differences in the separation areas of the wing due to the different endplates demonstrate that the blockage effect of the tunnel in this experiment has a significant effect on the results obtained. Nevertheless, the diminishing area of the separation areas of the NACA2402 endplate with increasing Reynolds number once again indicates that the findings in the CFD simulations can be replicated in a FS car at the working Reynolds number.

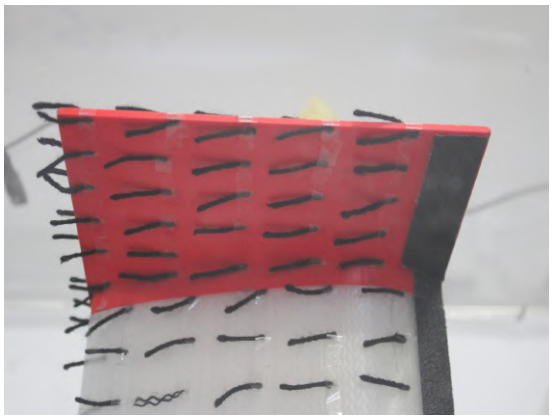

(a) Flat endplate.

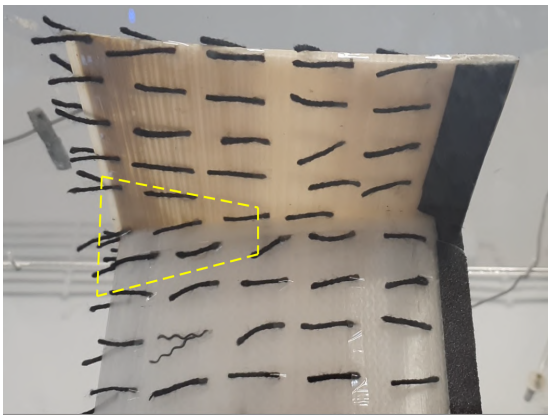

(b) NACA2402 endplate.

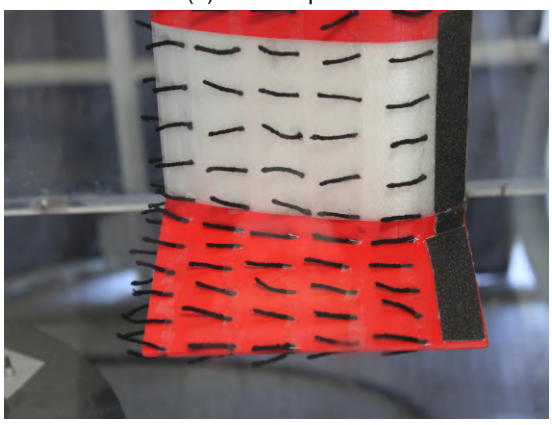

(c) Flat endplate.

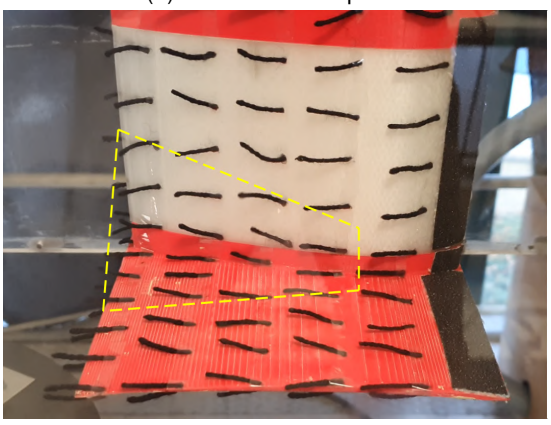

(d) NACA2402 endplate.

Figure 5.18: Woolen threads on the underside of the wing with the two different endplates at $Re = 8.70 \times 10^4$ on the wing underside.

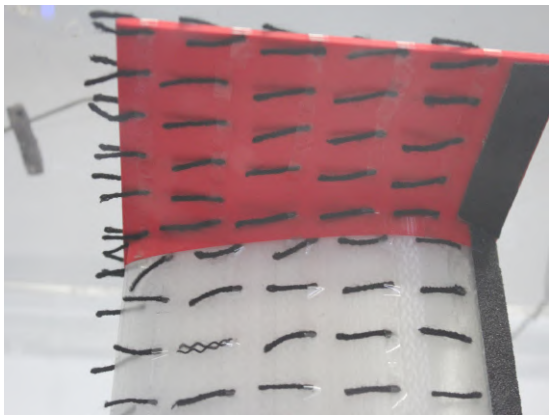

(a) Flat endplate.

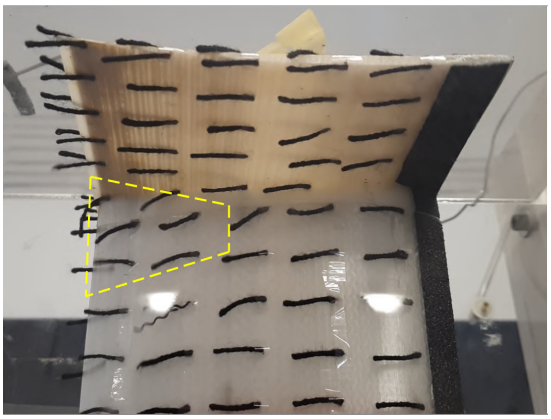

(b) NACA2402 endplate.

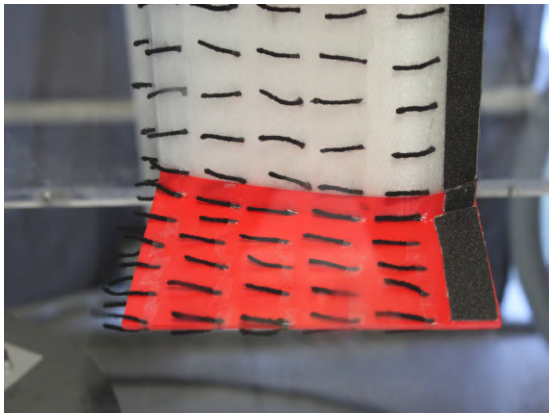

(c) Flat endplate.

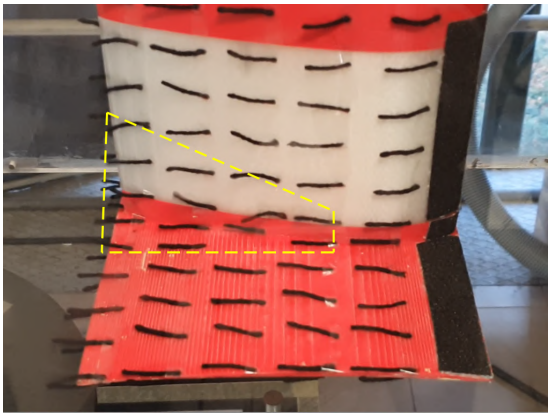

(d) NACA2402 endplate.

Figure 5.19: Woolen threads on the underside of the wing with the two different endplates at $Re = 1.63 \times 10^5$ on the wing underside.

Yaw simulations

Regarding the yaw experiments, these were also reproduced in Star-CCM+ with the same model. The results are in Table 5.9. These are compiled and compared with the results from the simulations of Chapter 4 and experiments in the plots of Figures 5.20 to 5.22.

Re	$\beta[^\circ]$	Endplate	C_L	$\Delta[\%]$	C_D	$\Delta[\%]$	C_L/C_D	$\Delta[\%]$
8.03×10^4	0	Flat	1.192	—	0.120	—	9.937	—
		2402	0.957	-19.8	0.124	3.3	7.721	-22.3
	4	Flat	1.176	—	0.126	—	9.308	—
		2402	1.036	-11.9	0.123	-2.7	8.431	-9.4
	8	Flat	1.152	—	0.143	—	8.063	—
		2402	0.999	-13.3	0.136	-4.5	7.323	-9.2
1.61×10^5	0	Flat	1.258	—	0.121	—	10.364	—
		2402	1.151	-8.5	0.117	-3.4	9.817	-5.3
	4	Flat	1.253	—	0.128	—	9.760	—
		2402	1.141	-8.9	0.121	-5.4	9.399	-3.7
	8	Flat	1.214	—	0.144	—	0.144	—
		2402	1.090	-10.2	0.134	-7.1	8.122	-3.4

Table 5.9: Results of the wind-tunnel simulations with a yaw angle.

First, the 2402 endplate has lower C_L across the different angles. However, the C_D is also lower than that of the Flat endplate. The net effect is larger C_L/C_D values for each of the yaw angles. The lift coefficient drops consistently with increasing β, whereas the drag coefficient rises sharply from $\beta = 4^\circ$ to $\beta = 8^\circ$. The result is a C_L/C_D that drops as well with increasing β.

In terms of lift coefficient (Figure 5.20), the wind tunnel experiment and simulation of the wind tunnel are in agreement in that the flat endplate has a higher C_L for each of the Reynolds numbers tested. This is against the results of the full model simulations.

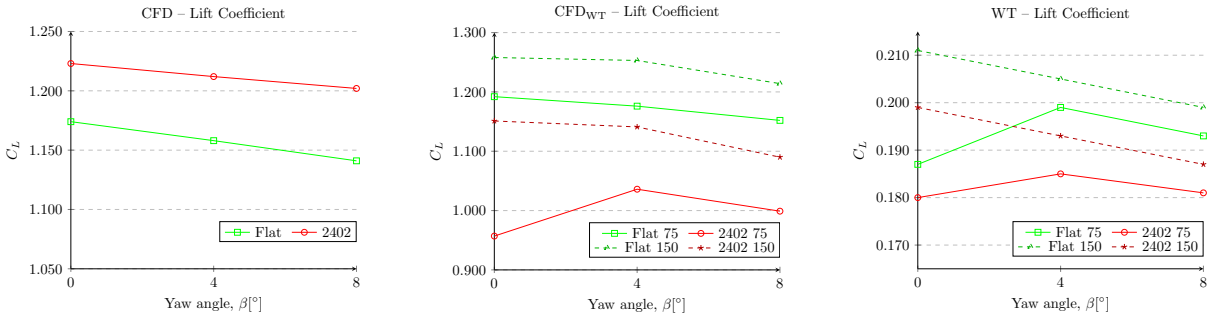

(a) CFD simulations. (b) Simulation of the WT. (c) Wind tunnel.

Figure 5.20: Lift coefficient values of the three data sets.

Regarding the drag coefficient (Figure 5.21) there are two different trends. The wind tunnel data indicates that the flat endplate has less drag then the NACA2402 one, even if at the higher Reynolds number the difference is small. The simulations of the wind tunnel show the opposite for $\beta = 4^\circ$ and $\beta = 8^\circ$: for those angles the NACA2402 endplate has a lower C_D than the flat endplate. In fact, for the highest Re the NACA2402 endplate has a smaller C_D , while the flat endplate has a higher C_D for the

highest Re.

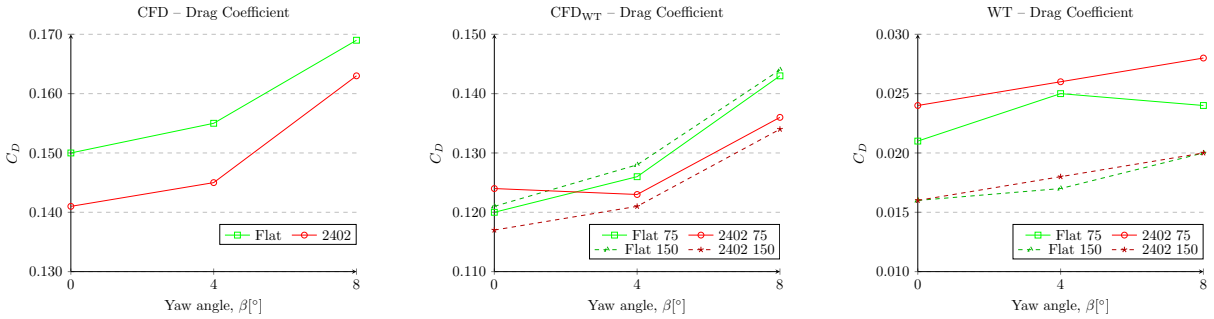

(a) CFD simulations. (b) Simulation of the WT. (c) Wind tunnel.

Figure 5.21: Drag coefficient values of the three data sets.

Concerning the C_L/C_D ratio, depicted in Figure 5.22, it comes as a consequence of the lift and drag coefficient trends mentioned above. The values from the wind tunnel testing have a wider range, with a higher increase in C_L/C_D compared to what was seen in the respective simulations of the experiment. On both the wind tunnel testing and the simulations of the tunnel, the overall efficiency was higher for the flat endplate, but the difference was smaller in the wind tunnel simulations, essentially due to the fact that in those the C_D was lower for the NACA2402 endplate.

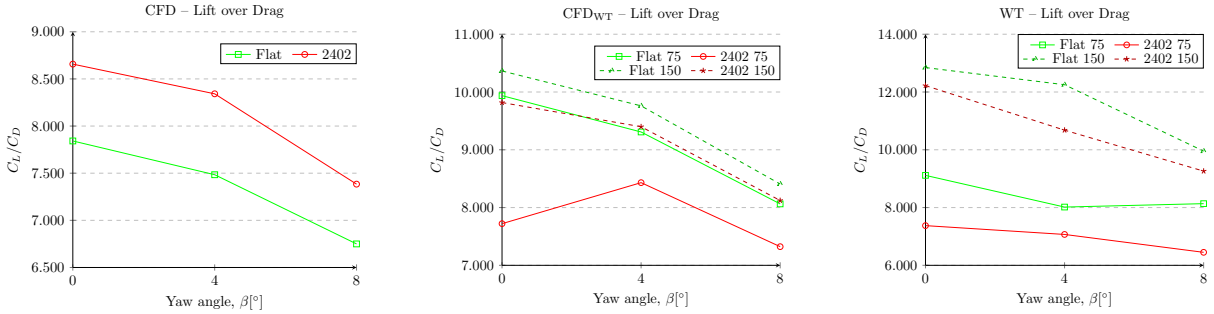

(a) CFD simulations. (b) Simulation of the WT. (c) Wind-tunnel.

Figure 5.22: Lift over drag values of the three data sets.

The fact that the simulations of the wind tunnel have given trends that are somewhat a middle-ground between the working Reynolds simulations and the wind tunnel once again points to the potential of this concept in a FS car, provided that more simulations and/or more experimental testes are conducted to prove its performance potential.

5.6 CAST Tunnel

At a later time the wing model was also tested at the Aeroacoustic Wind Tunnel of the CAST, whose outside view is shown in Figure 5.23, as a joint effort with another thesis project. It is a closed-circuit, U-shaped tunnel with an open circular working section whose diameter measures $1.6m$ that also features a 6DOF balance [40]. The tunnel has a maximum flow velocity of about $50m/s$ [41], which makes the flow similarity possible, as it is reached at $37.5m/s$.

Figure 5.23: Aeroacoustic Wind Tunnel of the CAST

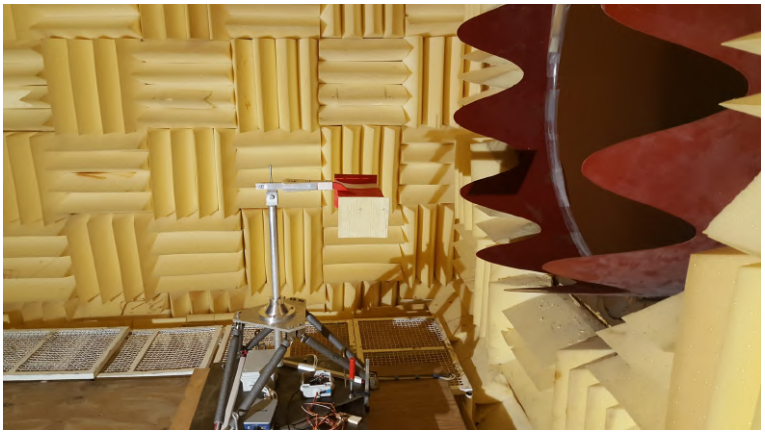

Figure 5.24: Wing model assembled in the Aeroacoustic Wind Tunnel.

The experimental procedure here was identical to the tests done in the other facility. Four different airflow velocities were tested for each of the three geometric configurations, from $15m/s$ up to $37.5m/s$. The wing model assembled on the balance at the CAST wind tunnel is shown in Figure 5.24.

In this case, since the maximum velocity to be tested allows for Reynolds similarity, and because the values are to be shared with the other thesis project, the sand paper strips were removed. So too were the woolen threads, since the working section is closed and opaque (for acoustic purposes), which does not permit the flow visualization like was done previously. The test results are presented in Table 5.10

and a comparison between the flat and 2402 endplate is provided in Table 5.11; the results are also plotted for the different Reynolds numbers in Figure 5.25.

Endplate	Velocity [m/s]	Re	Lift [N]	Drag [N]	C_L	C_D	C_L/C_D
No-Endplates	14.653	1.59×10^5	3.896	2.389	0.463	0.284	1.631
	22.072	2.40×10^5	9.368	4.710	0.491	0.247	1.989
	29.542	3.21×10^5	7.603	4.874	0.222	0.142	1.560
	37.011	4.02×10^5	12.848	6.105	0.239	0.114	2.105
Flat	14.653	1.59×10^5	3.571	2.935	0.424	0.349	1.217
	22.072	2.40×10^5	7.986	3.053	0.418	0.160	2.616
	29.542	3.21×10^5	12.068	5.022	0.353	0.147	2.403
	37.011	4.02×10^5	15.726	6.423	0.293	0.120	2.448
NACA2402	14.653	1.59×10^5	3.204	3.676	0.381	0.437	0.872
	22.072	2.40×10^5	7.282	2.590	0.381	0.136	2.811
	29.542	3.21×10^5	14.764	4.831	0.432	0.141	3.056
	37.011	4.02×10^5	17.126	6.217	0.319	0.116	2.755

Table 5.10: Values measured in the first run at the CAST tunnel.

Re	Difference to the flat plate Δ [%]		
	C_L	C_D	C_L/C_D
1.59×10^5	-10.3	+25.3	-28.4
2.40×10^5	-8.8	-15.1	+7.5
3.21×10^5	+22.3	-3.8	+27.2
4.02×10^5	+8.9	-3.2	+12.5

Table 5.11: Difference of the 2402 endplate's values to the flat endplate.

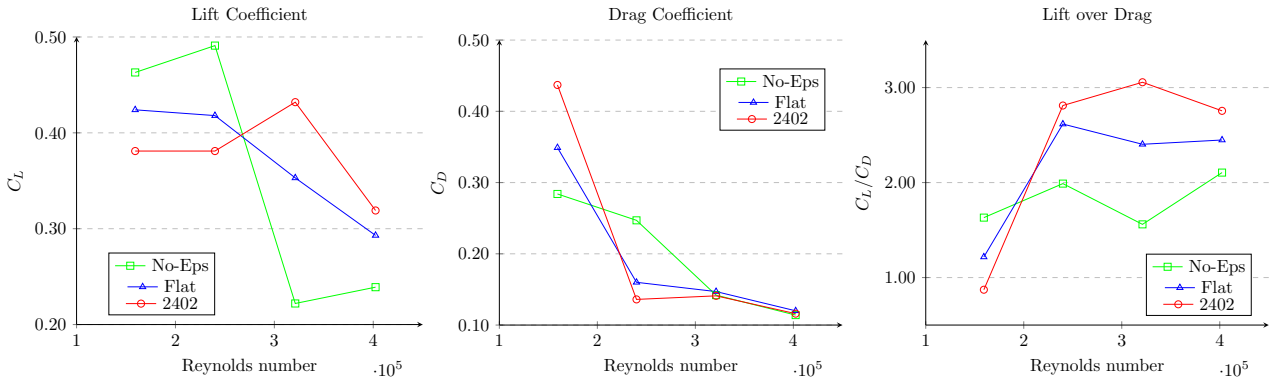

(a) Lift coefficient. (b) Drag coefficient. (c) Lift over Drag ratio.

Figure 5.25: Plots of the C_L , C_D and C_L/C_D coefficients for the 4 different Reynolds numbers tested at the CAST tunnel.

For the lowest Reynolds number, which coincides with the highest Reynolds number tested at the Fluids Laboratory, the trend is the same: the flat endplate has a larger C_L , smaller C_D and a higher C_L/C_D ratio. Regarding the C_L , at the second lowest Re the flat endplate still outperforms the 2402 endplate, but this trend is inverted for the two highest Reynolds numbers. Concerning the C_D this happens from the second lowest Re. This further emphasizes the influence that the low Reynolds

number has over the behaviour of the airflow. The efficiency values are a direct consequence of the evolution of the C_L and C_D coefficients, as such is smaller for the 2402 endplate than the flat endplate at the lowest Re, but for the three following Reynolds numbers is concurrent with the CFD simulations. At the highest Reynolds number, which enables the flow similarity, the trend is the same as the one observed with the simulations, indicating that the flow tested is in fact similar to the conditions simulated in CFD. This indicates that the proposed solution is valid for the Reynolds numbers that Formula Student experience.

Chapter 6

Conclusions

6.1 Conclusions

This project's aim was to improve the efficiency of the rear wing of a Formula Student car by changing its endplate geometry. More specifically, the addition of curvature to it by making use of a wing section meant to reduce the wing's induced angle of attack, simultaneously reducing its induced drag, increasing its lift and boosting its overall efficiency.

The use of the CFD simulations allowed this much, with a maximum increase of efficiency of the 2402 endplate of 10.4% when compared against a flat endplate with the same area. This increase was a result of the double effect of a larger lift coefficient and a smaller drag coefficient. The physical phenomenon responsible for this result was also illustrated with the results obtained. The use of the same concept on a wing with multiple flaps, however, did not yield the same results, which is something that should be further looked into.

The simulations with the yaw angles suggested that the proposed design can be an efficient alternative for Formula Student cars, when compared to the standard flat endplates. This is of significance in Formula Student events, where the most important ones – Autocross and Endurance – have tracks mostly composed of corners with different radii.

The wind tunnel testing provided two sets of data. The experiments in the fluids laboratory showed a significant effect of the Reynolds number on the force coefficients. It also showed that, even though it is a low Reynolds wind tunnel, where the Reynolds and scale effects are large, meaningful results and conclusions can be drawn from it. This is especially true when combined with the extra simulations mimicking the wind tunnel conditions since they exhibited similar trends. The tests done at the CAST wind tunnel were the final proof of validity of the concept that was developed in the simulations. It was possible to explore scale effects and confirm the trends obtained in the simulations and the strong effect of the Reynolds number. Unfortunately, it was not possible to perform the tests with a yaw angle in the CAST wind tunnel.

6.2 Future Work

To further understand and explore the possibility of using airfoils as section areas of endplates at the Reynolds numbers that the Formula Student cars experience, as well as their wings' dimensions (low aspect-ratio), there are a number of suggestions that could be followed to improve upon this work.

The intersection of the main plain with the endplate is a problematic area due to the developing boundary layers of each surface. Thickness and camber of the tip sections can be varied to improve the efficiency of the wing. However, preliminary tests showed that at the range of Reynolds numbers that the wing operates it is not easy to converge statistically steady simulations.

The fact that the effect of the single element wing element could not be replicated on the wing with the two flaps should also be looked into, since the difference in lift coefficient from the former to the latter was significant. This will have a significant impact on the overall performance of the Formula Student car, not only in terms of overall downforce, but also in terms of aerodynamic balance, which is important in Formula Student events due to the high number of corners in the Autocross and Endurance events. By further studying how to manipulate the interaction between the main wing's vortices and the vortices of the endplate, gains are to be had in terms of overall vehicle performance. There is potentially a good compromise to be reached, if for a lower downforce the decrease in drag is surpassed due to the new endplates, for instance with one less flap or with a higher main element angle of attack.

Further wind tunnel testing should be pursued, especially at the working Reynolds conditions. Given the new availability of the CAST tunnel for testing with its new balance, a full-scale model could be tested at even higher Reynolds numbers, providing the team with more data and information on how new performance can be extracted from this concept, without the difficulties of the Reynolds effects experienced during this project.

Finally, track testing with this concept on a car would provide invaluable insight into how the concept works in tandem with the entire aerodynamic package, as well as its influence on the global car performance. Given the reduced weight and improved efficiency of the proposed design, the driver's feedback would also be of importance.

Bibliography

[1] W. H. Hucho. *Hucho - Aerodynamik des Automobils: Strömungsmechanik, Wärmetechnik, Fahrdynamik, Komfort*, chapter Einführung, pages 1–67. Springer Fachmedien Wiesbaden, Wiesbaden, 2013. ISBN 978-3-8348-2316-8. doi: 10.1007/978-3-8348-2316-8_1. URL https://doi.org/10.1007/978-3-8348-2316-8_1.

[2] J. Katz. *Race Car Aerodynamics: Designing for Speed*. Bentley Publishers, 2003. ISBN 0 8376 0142 8.

[3] L. 95 Customs. The lotus 49 formula 1 car. URL http://www.95customs.com/interstate-1. Last accessed 10th April 2020.

[4] M. Pfadenhauer. *Hucho - Aerodynamik des Automobils: Strömungsmechanik, Wärmetechnik, Fahrdynamik, Komfort*, chapter Hochleistungsfahrzeuge, pages 551–650. Springer Fachmedien Wiesbaden, Wiesbaden, 2013. ISBN 978-3-8348-2316-8. doi: 10.1007/978-3-8348-2316-8_9. URL https://doi.org/10.1007/978-3-8348-2316-8_9.

[5] M. Trzesniowski. *Rennwagentechnik: Grundlagen, Konstruktion, Komponenten, Systeme*, chapter Aerodynamik Aerodynamics, pages 125–184. Springer Fachmedien Wiesbaden, Wiesbaden, 2014. ISBN 978-3-658-04919-5. doi: 10.1007/978-3-658-04919-5_5. URL https://doi.org/10.1007/978-3-658-04919-5_5.

[6] H. Dahlberg. Aerodynamic development of formula student race car. Bachelor's thesis, KTH, School of Engineering Sciences (SCI), Mechanics., 2014.

[7] S. Wordley and J. Saunders. Aerodynamics for formula sae: Initial design and performance prediction. *SAE International*, apr 2006. Paper 2006-01-0806, https://doi.org/10.4271/2006-01-0806.

[8] F. S. Germany. Formula student rules 2020, 2020. URL https://www.formulastudent.de/fsg/rules.

[9] V. de Brederode. *Aerodinâmica Incompressível: Fundamentos*. Colecção Ensino da Ciência e da Tecnologia. IST Press, Av. Rovisco Pais, 1049-001 Lisboa, Portugal, 1st edition, September 2014. ISBN 978-989-8481-32-0.

[10] J. John D. Anderson. *Fundamentals of Aerodynamics*. McGraw-Hill Series in Aeronautical and

Aerospace Engineering. McGraw-Hill, 1221 Avenue of the Americas, New York, NY, 10020, USA, 5th edition, 2011. ISBN 978-1-259-01028-6.

[11] D. Raymer. *Aircraft Design: A Conceptual Approach*. AIAA EDUCATION SERIES. American Institute of Aeronautics and Astronautics, Reston, VA, 6th edition, 2018. ISBN 978 1624104909. doi: https://doi.org/10.2514/4.104909.

[12] B. Mattos, A. Macedo, and D. S. Filho. *Considerations About Winglet Design*. doi: 10.2514/6.2003-3502. URL https://arc.aiaa.org/doi/abs/10.2514/6.2003-3502.

[13] R. T. Whitcomb. A design approach and selected wind tunnel results at high subsonic speeds for wing-tip mounted winglets. Technical report, NASA Langley Research Center, Hampton, VA, United States, July 1976.

[14] J. Guerrero, D. Maestro, and A. Bottaro. Biomimetic spiroid winglets for lift and drag control. *Comptes Rendus Mecanique*, 340:67–80, 02 2012. doi: 10.1016/j.crme.2011.11.007.

[15] G. S. J. Pacheco, M. Carreira. Aerodynamics DDJF, May 2020. FST Lisboa Design Document.

[16] R. Faria, P. Moura, J. Delgada, and A. Almeida. A sustainability assessment of electric vehicles as a personal mobility system. *Energy Conversion and Management*, 61:19–30, sep 2006. https://doi.org/10.1016/j.enconman.2012.02.023.

[17] M. Barham. Design and development of the electrical systems in an electric formula sae race car. Master's thesis, University of Canterbury, Christchurch, New Zealand, 2017. http://hdl.handle.net/10092/14397.

[18] J. P. Merkel. Development of multi-element active aerodynamics for the formula sae car. Master's thesis, University of Texas at Arlington, 2013.

[19] K. Yousefi and A. Razeghi. Determination of the critical reynolds number for flow over symmetric naca airfoils. In *AIAA Aerospace Sciences Meeting*, 2018. https://doi.org/10.2514/6.2018-0818.

[20] O. Reynolds. On the dynamical theory of incompressible viscous fluids and the determination of the criterion. *Proceedings of the Royal Society of London. Series A: Mathematical and Physical Sciences*, 451(1941), 1995. https://doi.org/10.1098/rspa.1995.0116.

[21] W. Jones and B. E. Launder. The prediction of laminarization with a two-equation model of turbulence. *International Journal of Heat and Mass Transfer*, 15(2):301–314, February 1972. https://doi.org/10.1016/0017-9310(72)90076-2.

[22] D. C. Wilcox. *Turbulence Modeling for CFD*. DCW Industries, DCW Industries, Inc. 5354 Palm Drive, La Cañada, California 91011, 3rd edition, November 2006. ISBN 978-1-928729-08-2.

[23] F. R. Menter. Two-equation eddy-viscosity turbulence models for engineering applications. *AIAA Journal*, 32(8):1598–1605, 1994. doi: 10.2514/3.12149. URL https://doi.org/10.2514/3.12149.

[24] H. Schlichting and K. Gersten. *Boundary-Layer Theory*. Springer-Verlag Berlin Heidelberg, 9th edition, 2017. ISBN 978-3-662-52917-1.

[25] H. K. Versteeg and W. Malalasekera. *An Introduction to Computational Fluid Dynamics*. Pearson Education Limited, Edinburgh Gate, Harlow, Essex CM20 2JE, England, 2nd edition, 2007. ISBN: 978-0-13-127498-3.

[26] *Simcenter STAR-CCM+® Documentation*. Siemens PLM Software, 2019. Version 2019.2.

[27] J. Bredberg. On the wall boundary condition for turbulence models. Internal Report 00/4, Department of Thermo and Fluid Dynamics, Chalmers University of Technology, Göteborg, Sweden, 2000.

[28] M. Selig. Low reynolds number airfoil design lecture notes. *VKI Lect. Ser.*, 01 2003.

[29] K. Hansenand, R. Kelso, A. Choudhry, and M. Arjomandi. Laminar separation bubble effect on the lift curve slope of an airfoil. 12 2014.

[30] M. H. L. Eça. The numerical friction line. *Journal of Marine Science and Technology*, 13:328–345, 2008. doi: https://doi.org/10.1007/s00773-008-0018-1.

[31] X. Zheng, C. Liu, F. Liu, and C.-I. Yang. Turbulent transition simulation using the k–ω model. *International Journal for Numerical Methods in Engineering*, 42(5):907–926, 1998. doi: 10.1002/(SICI)1097-0207(19980715)42:5<907::AID-NME393>3.0.CO;2-T.

[32] F. R. Menter, P. E. Smirnov, T. Liu, and R. Avancha. A one-equation local correlation-based transition model. *Flow, Turbulence and Combustion*, 95(4):583–619, December 2015. doi: 10.1007/s10494-015-9622-4.

[33] R. B. Langtry. *A Correlation-Based Transition Model using Local Variables for Unstructured Parallelized CFD codes*. Phd thesis, Universität Stuttgart, Fakultät Maschinenbau, May 2006.

[34] L. Eça. *Aerodinâmica Incompressível: Exercícios*. Apoio ao Ensino. IST Press, Av. Rovisco Pais, 1049-001 Lisboa, 1st edition, Dezember 2015. ISBN 978-989-8481-33-7.

[35] P. J. Roache. Quantification of uncertainty in computational fluid dynamics. *Annual Review of Fluid Mechanics*, 29(1):123–160, 1997. doi: 10.1146/annurev.fluid.29.1.123. URL `https://doi.org/10.1146/annurev.fluid.29.1.123`.

[36] C. J. R. W. L. Oberkampf. *Verification and Validation in Scientific Computing*. Cambridge University Press, 2010. doi: 10.1017/CBO9780511760396.

[37] J. L. E. Guerreiro and J. M. M. Sousa. Low-reynolds-number effects in passive stall control using sinusoidal leading edges. *AIAA Journal*, 50(2):461–469, 2012. doi: 10.2514/1.J051235.

[38] A. P. J. B. Barlow, W. H. Rae. *Low-Speed Wind Tunnel Testing, 3rd Edition*. John Wiley and Sons, INC., New York, 3rd edition, 1999. ISBN 978-0-471-55774-6.

[39] L. Traub. Experimental investigation of the effect of trip strips at low reynolds number. *Journal of Aircraft*, 48:1776–1784, 09 2011. doi: 10.2514/1.C031375.

[40] A. F. R. Oliveira. Design, construction, calibration and testing of a wind tunnel force balance. Master's thesis, Instituto Superior Técnico, October 2020.

[41] https://fenix.tecnico.ulisboa.pt/investigacao/cctae/tunel-aero-acustico. visited on 22/07/2020.

[42] M. Ferreira. Design of a six-component external wind tunnel balance. Master's thesis, Instituto Superior Técnico, July 2015.

Appendix A

Airfoil Nomenclature

An airfoil has several geometric definitions associated with it (Figure A.1).

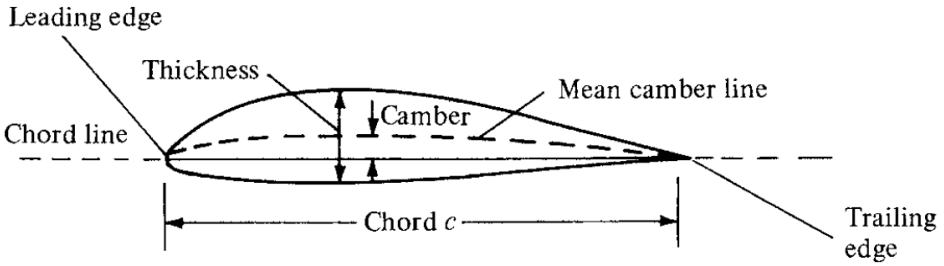

Figure A.1: Airfoil nomenclature.

These are[10]:

- *Leading edge*: the most forward point of the airfoil;
- *Trailing edge*: the most rearward point of the airfoil;
- *Chord line*: straight line that connects the leading and trailing edges of the airfoil;
- *Chord,* c: the length of the chord line;
- *Mean camber line*: the points equally distant to the upper and lower lines of the airfoil, measured perpendicular to the mean camber line itself;
- *Camber*: the maximum distance between the mean camber line and the camber line, orthogonal to the latter;
- *Thickness*: the distance between the upper and lower lines of the airfoil, perpendicular to the chord line.

Appendix B

Balance Specifications

B.1 Fluids Laboratory

The specifications of the balance at the Fluids Laboratory are as follows [42]:

- 6-6 in-parallel mechanism balance system:
  - 6-component measurement ability;
  - Single strut design, m6 20mm male thread at fixation point;
  - Equipped with Pitch, Yaw and Roll angle sensor, accurate to 0.1 ;
  - Overall dimensions: 700mm long, 700mm wide, 715mm high (the vertical strut is 300mm long and the device body is 415mm high).
  - Floor space required, 800 800mm;
  - Minimum required space below test section - 430mm;
  - 4 leveling feet with 120mm long thread;
- Load limits (maximum single loading, absolute values):
  - Normal force: 50N 0.4
  - Axial force: 30N 2.1
  - Side force: 30N 0.7
  - Roll moment: 2.5N.m 5.9
  - Yaw moment: 2.5N.m 2.0
  - Pitching moment: 2.5N.m 3.6
- Data acquisition
  - 6 force transducers;
  - 6 input channels, RJ-12 6P6C receptacles, with dedicated ultra-low noise 24-bit sigma-delta ADC;

  - Acquisition frequency: 150Hz;
  - Type of excitation: AC square wave, 150Hz
  - Amplification gain: 128;

B.2 Aerospace Laboratory

The balance of the Aerospace Laboratory has the following specifications [40]:

- Aerodynamic force balance:
  - Measurement of the 3 axial forces;
  - Measurement of the 3 axial moments;
  - Computation of air flow speed;
  - Computation of temperature and relative humidity;
  - Computation of model attitude.
- Aerodynamic force balance structure:
  - Based on 6-6 Stewart Platform;
  - Adjustable angle of attack and side-slip angle;
  - Adjustable top strut to use with a 1.42m wind tunnel circular nozzle.
- Instrumentation:
  - 6 Wheatstone strain-gauge half-bridges, each with a $1N$ sensitivity;
  - 2 NI 9237 boards by National Instruments TM;
  - 1 pressure sensor MPXV7002DP;.
  - 1 temperature sensor DHT11;
  - 1 attitude MPU-6050;